



Universiteit
Leiden



Eidgenössische Technische Hochschule Zürich
Swiss Federal Institute of Technology Zurich

Improving Direct Imaging of Exoplanets using Spectral Observations from SPHERE/IFS

Master Thesis

Sven Kiefer

November 9, 2020

Supervisor: Prof. Dr. Sascha Patrick Quanz IPA, ETH Zürich
Co-Supervisor: Alexander Julian Bohn Leiden Observatory

*The curious mind will find questions
where answers were expected*

Abstract

Detecting and characterising exoplanets with direct imaging is a challenging task which requires state-of-the-art instrumentation and advanced processing techniques. Spectral data can be used to improve the star-exoplanet contrast and to classify detected objects.

In this thesis, SPHERE/IFS support was added to the python package PynPoint. This includes basic data reduction, wavelength support to pre-existing modules and, most notably, spectral differential imaging (SDI). Combining SDI with the already implemented angular differential imaging (ADI) allowed to combine them to three different advanced differential imaging techniques. Furthermore, the model based rejection was developed to characterise detected companion candidates and classify them as bound to the observed star or as background contaminants. This method uses theoretical models to estimate a companion candidate's effective temperature, surface gravity, metallicity and distance. Using those estimations, the model based rejection can classify objects as bound or background.

The newly implemented functionalities were tested on Beta Pictoris, 51 Eridani and HR 8799. Using SDI and ADI together achieved clearer detections and more favourable contrast limits than when only using ADI. Moreover, an improvement of the technique's performance was observed with larger wavelength range $\Delta\lambda$, larger angular rotation $\Delta\alpha$ and longer integration times Δt . These parameters have an upper limit, after which increasing them no longer improves the detections. Additionally, the analysis of the technique's dependence on companion brightness revealed that differential imaging techniques are not suitable for bright companions as they reduce their signal. The model based rejection was tested on 51 Eridani b and correctly classified it as a companion.

Lastly, the advanced differential imaging techniques and the model based rejection were used to investigate five targets from the Sco-Cen association: 2MASS J 11555771-5254008 (Ob1), 2MASS J 13381128-5214251 (Ob2), 2MASS J 12123577-5520273 (Ob3), 2MASS J 13251211-6456207 (Ob4) and 2MASS J 13233587-4718467 (Ob5). In the dataset of Ob1, a companion candidate was found at $SEP = 0.371 \pm 0.003$ arcsec, $PA = 16.8 \pm 0.4^\circ$ and it was classified as a bound M-dwarf ($T_{\text{eff}} = 3000\text{K}$, $\log g = 4.5$, $\text{FeH} = -0.5$, distance = $60 \pm 25\text{pc}$). In the dataset of Ob2, a companion candidate was found at $SEP = 0.151 \pm 0.007$ arcsec, $PA = 166 \pm 3^\circ$ and it was classified as a background K-dwarf ($T_{\text{eff}} = 3600\text{K}$, $\log g = 5.0$, $\text{FeH} = -2.0$, distance = $360 \pm 90\text{pc}$). No companion candidates were found in Ob3, Ob4 or Ob5.

Overall, the newly implemented advanced differential imaging techniques and spectral characterisation tools allow for a more detailed analysis of direct imaging data than the current PynPoint version. By implementing these techniques into the framework of PynPoint, they become accessible for further studies and will hopefully help discover new exoplanets.

Contents

1	Introduction	1
2	Background on Exoplanet Research	3
2.1	Search for Exoplanets	3
2.2	SPHERE/IFS	5
2.3	PynPoint	7
2.4	Spectral Differential Imaging (SDI)	10
2.5	Background Contaminants	13
2.6	Spectral Characterisation of Exoplanets	14
3	PynPoint Modifications	16
3.1	Basic PynPoint Functionalities	16
3.2	New Adjusted Modules	18
3.3	IFS Support Function	21
3.4	PCA PSF Reduction	23
3.5	Companion Detection	26
3.6	Spectral Characterisation	27
3.7	The Pypelines	28
4	Testing Differential Imaging	32
4.1	Iterative PCA	33
4.2	Advanced Differential Imaging Techniques	36
4.3	Companion Brightness	40
4.4	Rotation and Wavelength Range	42
4.5	Integration Time	45
4.6	Further ADI/SDI Combinations	46
4.7	STIM Detection Map	49
5	Background Star Rejection	52
5.1	Model Based Rejection	52
5.2	Temperature-Radius Relation for Brown Dwarfs	54
5.3	Unsuitable Rejection Criteria	56
5.4	Testing	59

6	Search for Exoplanets	62
6.1	Object 1: 2MASS J 11555771-5254008	63
6.2	Object 2: 2MASS J 13381128-5214251	66
6.3	Object 3: 2MASS J 12123577-5520273	69
6.4	Object 4: 2MASS J 13251211-6456207	71
6.5	Object 5: 2MASS J 13233587-4718467	73
7	Conclusion	75
8	Outlook	78
8.1	Next Steps	78
8.2	The Future of Exoplanet Research	81
	Acknowledgement	82
	Index of Abbreviations	82
	References	83
A	Additional Graphs	89
B	Python Code	97
C	Declaration of Originality	110

Introduction

Are we alone in the universe? This is one of the most fundamental questions of mankind. Even the ancient Greek philosophers argued about life outside of Earth (Crowe [1997]). Unfortunately, they didn't have the means to actively search for signs of life and thus could only debate their ideas. Throughout the next centuries, the idea of extra-terrestrial life was discussed by many philosophers around the world (Schneider [2009]). But the tools to search for an answer were not yet available.

In the early 20th century, technology advanced rapidly and researchers finally had the means to search for the answers to centuries old questions. Huge telescopes and immense computational power allowed to search the universe and resulted in many ground-breaking insights. Among these was the discovery of the first exoplanets during the 1990s. Since then, thousands of exoplanets were found and, whenever possible, characterised.

This thesis focused around one of the exoplanet discovering techniques: direct imaging. More specifically, the advantages of spectral observations in addition to the usual broadband techniques were investigated. To observe planetary spectra, state-of-the-art instruments are needed. One example of such an instrument is SPHERE, which will be used throughout this thesis.

In direct imaging, observations alone are not good enough to detect faint exoplanets as their signal is buried underneath the residual star noise, background influences and instrumentation errors. To correct these and to increase the detection limits of exoplanets, highly advanced processing techniques have been developed. As many different techniques exist (e.g. bad pixel filters, angular differential imaging (ADI) and principal component analysis (PCA)), software packages containing the most important functionalities are useful tools to keep the overview and simplify using them. For this thesis, PynPoint (Amara and Quanz [2012], Stolker et al. [2019]) was used and expanded through the implementation of new techniques.

This thesis revolved around observations with SPHERE/IFS and the techniques used to improve exoplanet detections via direct imaging. The three main goals were:

- **Goal 1:** Implement and test the power of advanced differential imaging techniques (defined in chapter 2.4), based on the spectral and angular diversity in the data, and determine the detection limits of the corresponding reductions.
- **Goal 2:** Develop tools for characterisation of potential companions and rejection of background contaminants by spectral analysis.
- **Goal 3:** Use advanced differential imaging techniques to search for companion candidates in five unpublished datasets and, if successful, characterise the source as bound to the observed star or as background contaminant.

To achieve the first goal, the framework of PynPoint was used. As it already supports a large variety of processing techniques to evaluate broadband data, it was an ideal starting point to add advanced differential imaging techniques. Additionally, PynPoint was already successfully used and tested on several occasions (e.g. [Bohn et al. \[2019\]](#) and [Cugno et al. \[2019\]](#)). To compare the newly implemented functionalities and to find their advantages and disadvantages, numerous tests were conducted such as: single vs iterative PCA, companion brightness, rotation range, wavelength range and integration time. The implementation of the advanced differential imaging techniques is explained in chapter 3 and their testing is described in chapter 4.

The second goal was set to improve observations and to learn more about the characteristics of exoplanets. A rough characterisation is especially useful because a bright star far behind the observed target can mimic a bound but fainter companion. With a single broadband observation, the two cannot be distinguished and therefore a second observation is necessary to differentiate them. Using the additional spectral information, this can be done with a single observation as the spectrum of a star and a companion can differ substantially. For this thesis, a basic characterisation and distinguishing tool was developed and implemented into the framework of PynPoint. The characterisation tool for background rejection is explained in chapter 5.

Lastly, the implemented techniques were used to search for and characterise exoplanets around five observed targets from the Sco-Cen association. This is a young, star forming region and thus ideal for direct imaging as the additional formation heat of exoplanets helps to detect them. All targets were searched for exoplanets and the detection limits for the newly implemented processing techniques were determined. Two of the targets have a previously known object at small enough separations to be within the field of view (FOV) of SPHERE/IFS. The objects found in those sets were characterised using the developed tools and it was determined if they are bound or background. In chapter 6, the processing and results of the five datasets are described and discussed.

The final conclusion over all results is drawn in chapter 7. Lastly, in chapter 8 possible next steps building on the work of this thesis are given.

Background on Exoplanet Research

Exoplanet research is a young and rapidly growing field. Many thousand exoplanets have been found in the last 30 years using either the transit method, radial velocity measurements or direct imaging. This requires state-of-the-art instrumentation and advanced processing which is constantly improved. To learn more about the diversity and characteristics of exoplanets, those instruments were equipped with spectrographs to probe their atmosphere. Afterwards, the observations can be compared with theoretical models, which might lead to a more detailed characterisation of exoplanets. In this section, a short summary of the most important topics of exoplanet research regarding this thesis is given.

2.1 Search for Exoplanets

On the 6th of October 1995, the first exoplanet orbiting a main sequence star was discovered by [Mayor and Queloz \[1995\]](#). Since then, many exoplanets have been discovered using one of three main methods: radial velocity, transits or direct imaging. Especially the Kepler mission was hugely successful, detecting thousands of exoplanets using the transit method ([Borucki \[2016\]](#)). These observations revealed that exoplanets are not as rare as expected and that stars have on average more than one planet ([Cassan et al. \[2012\]](#)). Many of the discovered objects do not have a solar system equivalent, thus revealing the diversity of exoplanets. Since the three main detection methods use different properties of stars and exoplanets, they can be used to probe different characteristics. In this section, a short overview over these methods is given.

The radial velocity method uses small orbital motions of a star induced by lighter, orbiting objects. Large planets (e.g. Jupiter in the solar system) can offset the centre of mass enough to produce a detectable radial motion of a star ([Seager \[2010\]](#)). The heavier and the further away a planet is, the stronger the signal becomes,

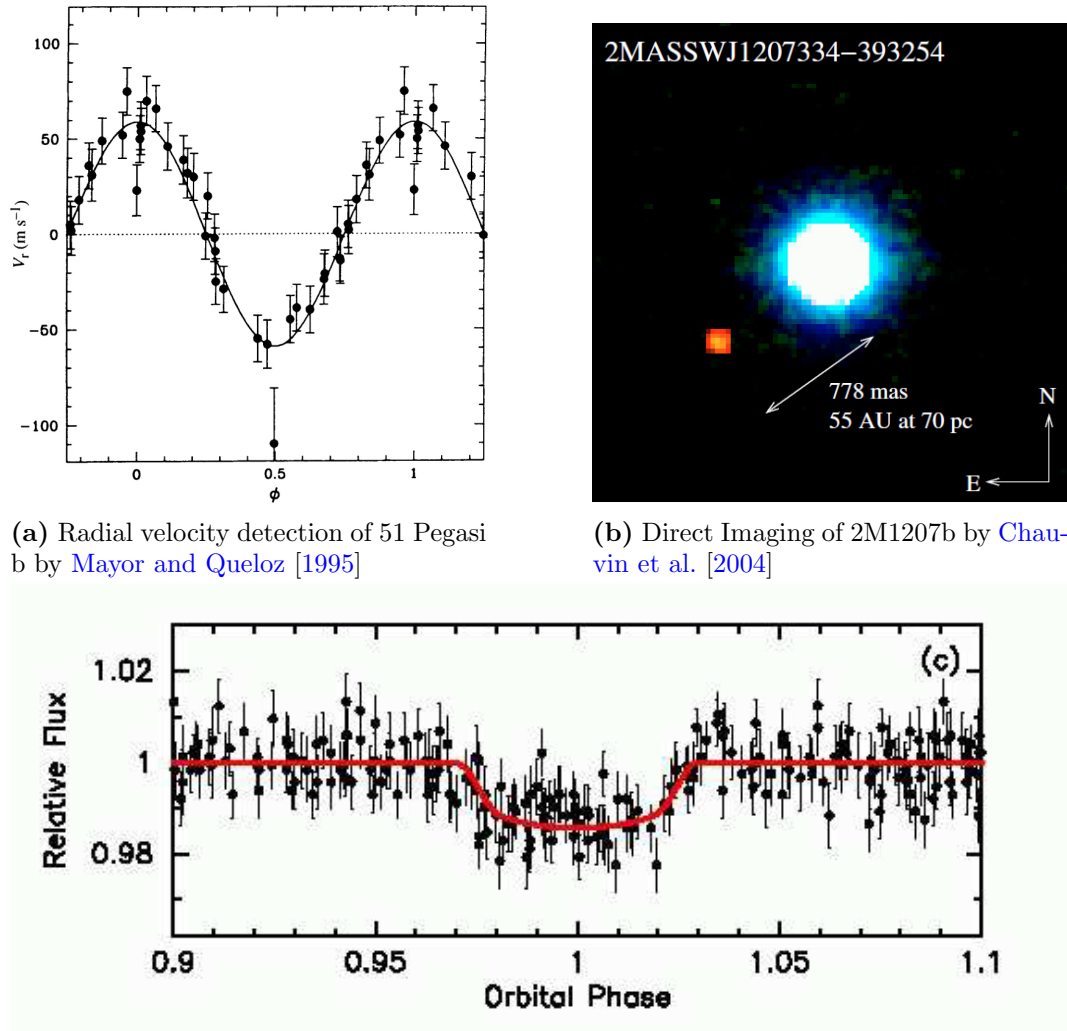


Figure 1: Detection of exoplanets using the three main methods. The objects displayed are some of the first discovered with their respective method. There is no clear consensus whether 2M1207b should be considered a planet or a brown dwarf. The detection of 51 Pegasi b by [Mayor and Queloz \[1995\]](#) was awarded the 2019 Noble prize.

therefore favouring massive exoplanets at large separations. On the other hand, a large separation means long orbital periods and therefore, longer observations are required to measure a full period of the object. Hot-Jupiters are objects with approximately the mass of Jupiter on orbits closer than mercury. Thus, they are good targets for the radial velocity method as they have a strong signal and short orbital periods.

The transit method uses the darkening of a star caused by an exoplanet if it crosses the line of sight between the star and an observer (like the moon covering the sun during a solar eclipse) (Seager [2010]). Large Planets (e.g. Jupiter sized) can cause the star's luminosity to drop by approximately 1%. The chance for an aligned orbit decreases with the distance between star and planet. Therefore, the transit method favours large exoplanets at small separations (e.g. Hot-Jupiters). The Kepler space mission searched for exoplanets using the transit method and found thousands of exoplanets by observing roughly 150'000 stars (Borucki [2016]). Additionally, the transit method can be used to measure the spectrum of exoplanets as the measured transit depth depends on the chemical composition of its atmosphere (Seager [2008]). Even though many observations are needed to achieve a reasonable accuracy, this technique allows to probe the chemical composition of transiting exoplanets

Direct imaging uses light emitted from an exoplanet to directly detect it. State-of-the-art technology is required to overcome the two main challenges: high angular resolution and high contrast (Seager [2010]). To achieve high angular resolution, large telescopes are required, as the mirror size can be a limiting factor (diffraction limit given by $\theta \propto \lambda/\mathcal{D}$, where λ is the observed wavelength and \mathcal{D} the diameter of the telescope). To achieve high contrast, the light of the star must be reduced as it is often more than 10^6 times brighter than a possible accompanying planet. To increase the contrast, coronagraphs are used to block the light from the star (Mennesson et al. [2016]). Young exoplanets are still hot from their formation and thus emit more light, especially at infrared wavelengths. The contrast is more favourable the further away the planet is from the star. Massive, young exoplanets at large separations are therefore the best targets for direct imaging. As this method separates star from planet flux, the spectrum can be obtained using high contrast spectrographs (e.g. SPHERE/IFS or SINFONI).

2.2 SPHERE/IFS

The very large telescope (VLT) is operated by the European Southern Observatory and located at Paranal Observatory in the Atacama Desert of Chile. It consists of four 8m class telescopes operating at visible and infrared wavelengths using many different instruments (e.g. SPHERE and the upcoming ERIS for exoplanet research). For this thesis, data from SPHERE (Spectro-Polarimetric High-contrast Exoplanet REsearch) was used, which has three science instruments: ZIMPOL, IRDIS and IFS. The instruments specifications are presented by Beuzit et al. [2019]. In this chapter, a short summary of the most important aspects of SPHERE/IFS is given

as most data used in this thesis was taken by this instrument.

One of the biggest limitations of ground based observations are perturbation effects caused by the turbulent motion of earth's atmosphere such as non-common path aberrations (NCPAs). To correct for those effects, adaptive optics (AO) systems have been developed and implemented into SPHERE/IFS (Fusco et al. [2006]). They first measure the distortion of the incoming light and then correct them by adjust a deformable mirror accordingly. Atmospheric distortions are only stable for several milliseconds (depending on the weather conditions). Therefore, the AO system work best, if they are able to measure, calculate and apply the corrections while the atmosphere remains stable. The influence caused by NCPAs is called atmospheric seeing and is expressed in arcsec. State-of-the-art telescopes with AO systems typically achieve a seeing of 0.5 to 1 arcsec (Petit et al. [2014]).

The goal of SPHERE is to search for giant exoplanets around nearby stars. Therefore, the biggest challenges are the large contrast between an exoplanet and its host star and their small angular separation. SPHERE's two big advantages for high contrast imaging are its advanced AO system and its high efficiency coronagraphs. This combination allows to observe companions with a typical contrast of $\Delta\text{mag} = 13.5$ at a separation of 0.5 arcsec under regular observing conditions Beuzit et al. [2019].

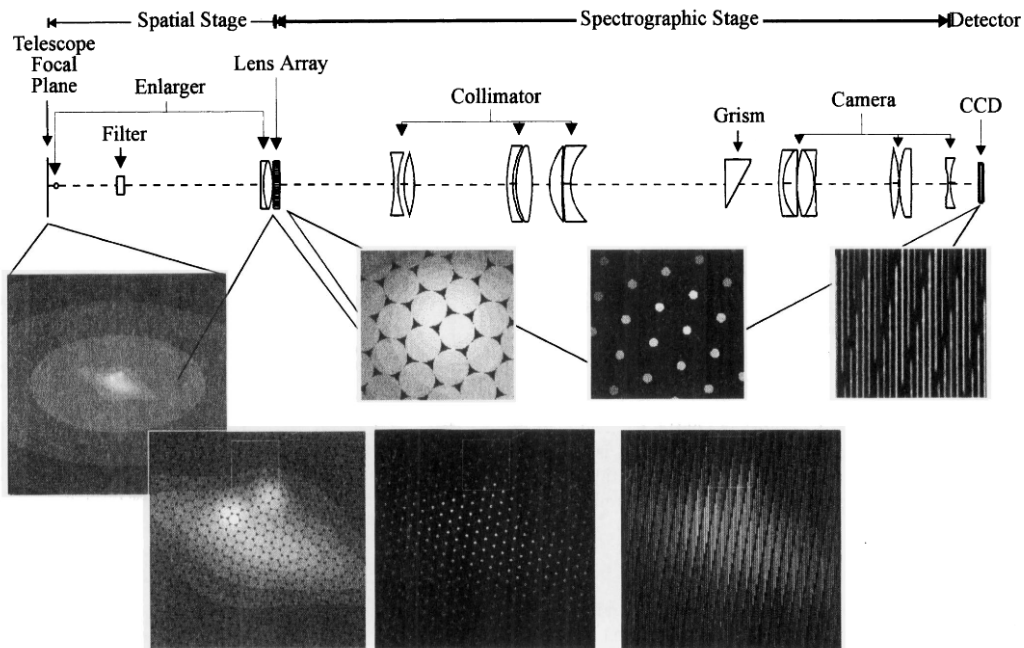


Figure 2: Optical set up of TIGER. Image taken from Bacon et al. [1995].

To image an exoplanet directly is challenging nevertheless and therefore choosing the right targets is crucial. SPHERE was built to focus on young stars with ages < 50 Myr and nearby young associations with ages 10 - 100 Myr at distances of 30 - 100 pc (Beuzit et al. [2008]). Those are ideal targets because of their formation heat especially at infrared wavelengths (Baraffe et al. [2003]).

The integral field spectrograph (IFS) of SPHERE measures low resolution spectra [Claudi et al. \[2008\]](#). This instrument uses an array of lenslets to bundle small areas of the observed sky. Afterwards, a grating prism is used to split the bundle into different wavelength components. As an example, the optical design of the TIGER IFS can be seen in figure 2. Based on this design, [Claudi et al. \[2006\]](#) developed their design for SPHERE/IFS. An example of a raw SPHERE/IFS image can be seen in figure 8a.

The wavelength range can be set to 0.95 - 1.35 μm with a resolution of $R \approx 50$, or it can be set to 0.95 - 1.68 μm with a spectral resolution of $R \approx 30$. In both cases, there are 39 channels evenly split over the wavelength range ([Wahhaj et al. \[2019\]](#)). The field of view (FOV) is approximately 1.73" x 1.73". This is a relatively small FOV compared to other instruments (e.g. IRDIS: 11" x 11"). Additionally, the smallest observable separation from the target star (inner working angle) is limited by the coronagraph at 0.1 arcsec ([Wilby \[2018\]](#)).

SPHERE/IRDIS was built for broadband and dual-band imaging ([Beuzit et al. \[2019\]](#)). Using the IRDIFS_EXT mode, both IRDIS and IFS can be used simultaneously. It covers a wavelength range of 0.95 - 2.32 μm using various filters. SPHERE/IRDIS has a FOV of approximately 11" x 11" which allows to search larger a larger FOV for exoplanets than SPHERE/IFS ([Wahhaj et al. \[2019\]](#)). Combining SPHERE/IFS with SPHERE/IRDIS allows to cover a wider wavelength range. The additional coverage, despite being broadband, can be very useful for atmospheric model fitting.

To observe the host star, SPHERE is equipped with neutral density filters to uniformly reduce the flux which can be used to prevent saturation of the detector. There are four filters ND_0, ND_1, ND_2 and ND_3.5 which have a transmission on average of 1, 10^{-1} , 10^{-2} and $10^{-3.5}$, respectively. The exact transmission curves can be found in [Wahhaj et al. \[2019\]](#) on page 103.

2.3 PynPoint

State-of-the-art instrumentation alone is not good enough to detect most exoplanets as the residual star noise influences measurements substantially. Therefore, highly advanced processing techniques have been developed to reduce the residual star noise and background noise. Many different image processing steps are involved to evaluate direct imaging data and the best processing steps vary for each observation. Therefore, software packages containing the different steps are crucial to efficiently evaluate exoplanet observations.

[Amara and Quanz \[2012\]](#) and [Stolker et al. \[2019\]](#) developed the python package PynPoint for processing direct imaging data taken by, for example, SPHERE or NACO. It contains all steps in order to process direct imaged data and allows setting up pipelines to produce final images starting from raw data. Additionally, it contains many functionalities to better explore, analyse and process data. A full list of functionalities can be found in the official documentation¹.

¹Available at <https://pynpoint.readthedocs.io/en/latest/>

Angular Differential Imaging (ADI)

One of the core functionalities implemented into PynPoint is angular differential imaging (ADI). To use this technique, raw images are taken with the instrument derotator turned off. This causes the field of view to rotate around its centre during observations. All instrumentation effects will be, to first order, static but a possible companion around a star will move during the observations. The residual star noise is assumed to be quasi-static and thus should be reduced to some degree as well. Therefore, those images can be used to create a reduction frame for example by taking the median of all images. As a possible companion moves, it will not (or only faintly) appear after median combining all images while the stellar PSF and instrumentation effects will be dominant. The reduction image can then be subtracted to reduce the static effects in the original images. Afterwards, all images can be derotated and stacked. A possible companion should remain while the stellar PSF and instrument effects are reduced. However, the assumption of a quasi static residual stellar noise only holds partially. Because not all residual star light will be completely reduced, SDI can help to clean the images further (see chapter 2.4). For more information on ADI refer to [Marois et al. \[2006\]](#).

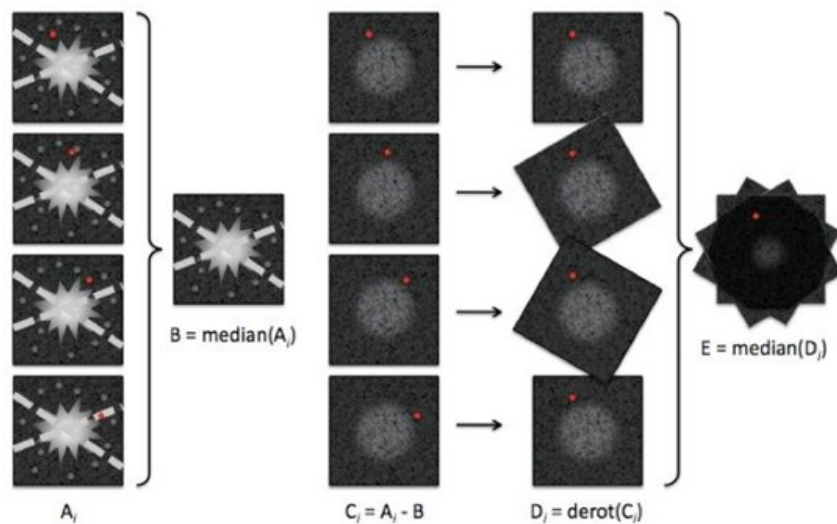


Figure 3: Schematics of ADI. The images (A_i) are taken with the instrument derotator turned off, causing all off-centre sources to rotate while instrument effects stay static. A subtraction image (B) can be created by averaging over all images. All rotating sources will not (or only faintly) appear in the reduction image. Afterwards, the images get subtracted by the reduction image leaving only moving sources behind (C_i). After derotating (D_j) and stacking all images a possible companion could be visible in the final image (E). (Image: Christian Thalmann)

Principal Component Analysis (PCA)

Instead of taking the median, principal component analysis (PCA) can be used to reduce all images Im_j from a dataset. The goal of PCA is to model the stellar PSF and subtract it from all science images. To achieve this, PCA generates an orthonormal basis $B = B_1, \dots, B_N$ called principal components where the first component describes the direction of maximum variance. The second component corresponds to the direction of maximum variance orthogonal to the first component. This is repeated until an orthonormal basis is established:

$$\text{Im}_j = \sum_{i=0}^N a_{ji} B_i \quad (1)$$

Because a companion moves between the images, it does not influence the variance significantly. Therefore, the first $D \ll N$ principal components should only reduce the stellar PSF. Therefore, fitting the components $\tilde{B} = B_1, \dots, B_D$ to the images Im_j creates a model $M_{PSF,j}$ of the PSF for each image without possible companions. This model can then be subtracted from the initial images Im_j :

$$M_{PSF,j} = \sum_{i=0}^D b_{ji} B_i \quad (2)$$

$$\text{Im}_{j, \text{reduced}} = \text{Im}_j - M_{PSF,j} \quad (3)$$

In PynPoint the calculation of the principal components is done with scikit-learn² (Pedregosa et al. [2011]). Afterwards, the images Im_j are processed as described above to produce $\text{Im}_{j, \text{reduced}}$. Those images can then be derotated and stacked to create the final image. A more detailed description of the implementation in PynPoint is given by Amara and Quanz [2012].

If more principal components are selected, the stellar PSF is removed more efficiently but it also increases the chance to inadvertently reduce a possible companion. On the other hand, the stellar PSF is not modelled precisely enough if too few components are selected and a possible companion would not be distinguishable from PSF speckles. Therefore, the ideal number of principal components depends on the target and must be found individually for each case. A further investigation into the ideal number of PCA components was done in chapter 4.2. In general, the fainter the target the more principal components are necessary. The influence of the companion's brightness on the PCA reduction was investigated in chapter 4.3.

²Available at <https://scikit-learn.org/stable/>

2.4 Spectral Differential Imaging (SDI)

Not only the time dependence of a companion's position but also the wavelength depended scaling of the residual stellar light can be used to achieve clearer exoplanet detections. Therefore, this thesis aims for adding SPHERE/IFS support to the current PynPoint package to enable SDI reductions. Especially the combination of SDI with ADI was analysed in section 4. In this chapter, the basic properties of SDI are described as well as its importance for processing direct imaging data.

The Basics of SDI

Like ADI, SDI uses displacements of a possible companion to create a reduction image with no companion signal. For ADI this would be image B in figure 3. Because of the diffraction caused by the telescope, a point source will be spread out. The distribution of the diffracted light is called point spread function (PSF). The shape of the PSF is approximately the same for all wavelengths, but the radial scaling differs ($\text{PSF}(r) \propto \lambda/\mathcal{D}$, where λ is the observed wavelength and \mathcal{D} the diameter of the telescope). If the images are rescaled using a factor $S \propto 1/\lambda$, then the speckles are aligned and the stellar PSF is at the same FWHM while at the same time causing a radial shift in position of a possible companion. The difference to ADI is that displacement of a possible companion is radial instead of azimuthal (see figure 4). Afterwards the reduction image is back-scaled proportional to their wavelength to have the same scaling as the original images. Lastly, the rescaled reduction frames are used to correct the initial images before stacking them to one final image.

A main problem in direct imaging with ground-based telescopes is the stellar PSF, which covers the planetary signal. Especially NCPAs (even if they are partially corrected through an AO system) and the finite telescope size cause a point source to split into a large PSF with many speckles. Because ADI averages over the time dimension, the time dependence of the NCPAs is not taken into account. SDI on the other hand uses only frames that were taken at the same time. Therefore, SDI is ideal to search for exoplanets close to the star where stellar speckles are the limiting factor. The performance of SDI depending on the separation has been investigated during this thesis and can be found in chapter 4.2.

The scaling of the images leads to a reduced FOV. For the SDI reduction, the smaller wavelength images are scaled up to create the reduction image. Thus, high separations are not covered by all wavelengths (see figure 4). The instrument SPHERE/IFS has a FOV of 1.73 arcsec and a spectral range of 0.95 - 1.35 μm (or 0.95 - 1.68 μm) (Wahhaj et al. [2019]). After rescaling the images with $S = \lambda/\lambda_{max}$, this leads to a FOV with complete coverage of 1.22 arcsec (or 1.00 arcsec). The remaining outer area is not covered by all wavelengths and therefore only partially reduced. Objects in this region are defined as partially within the FOV. If only ADI is applied, this FOV reduction does not occur.

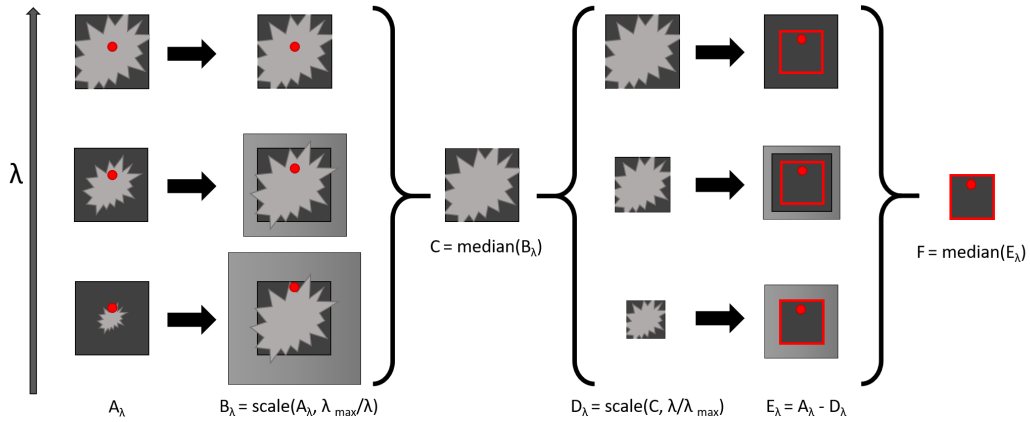


Figure 4: Schematic of SDI (including the FOV loss through scaling). First, the images (A_λ) need to be scaled inverse proportional to their wavelength (B_λ) and then averaged to create the reduction image (C). Afterwards the reduction image is back-scaled proportional to their wavelength (D_λ) to have the same scaling as the original images (A_λ). Therefore, the outer region of the small wavelength images is not covered by the SDI reduction. This reduces the completely covered FOV by a factor $S = \lambda_{\min}/\lambda_{\max}$. The completely covered FOV is marked by a red boarder, the companion is marked as a red dot.

Advanced Differential Imaging

As ADI uses the time dependence of the companion's position, it is specifically useful to reduce static noise sources. Time dependent objects changes their position and are therefore reduced less. In contrast, SDI uses the wavelength scaling of the stellar PSF at each time instance. Because SPHRER/IFS can observe 39 wavelengths at once, its observations can be used to perform SDI. To benefit from the advantages of both ADI and SDI, they can be combined. The six techniques used during this thesis including their abbreviation, are listed below. A priori it is not clear which combination achieves the clearest detections.

- **NAN:** This method is equivalent to classical ADI as described in chapter 2.3. The only difference, NAN uses the mean instead of the median to generate the reduction frame.
- **ADI:** This method splits the dataset into subsets with the same wavelength. Afterwards, the mean is subtracted before a PCA reduction is used on each subset with a given number N of principal components. The variable N is the same for all subsets. As a last step the images are derotated and stacked to create the final image³.

³To prevent ambiguous abbreviations, classical ADI will be referred to as NAN and ADI+PCA will be referred to as ADI for the rest of this thesis.

- **SDI:** This method splits the dataset into subsets of the same time instance. Afterwards, all images are scaled according to their wavelength with a scaling factor of $S(\lambda) = \lambda_{max}/\lambda$. Then, the mean is subtracted before a PCA reduction is used on each subset with a given number N of principal components. The variable N is the same for all subsets. As a last step the images are scaled back with $B_{im} = 1/S_{im}$, derotated and stacked to create the final image.
- **SAA:** This method first scales all images with $S(\lambda) = \lambda_{max}/\lambda$. Afterwards, the mean is subtracted before a PCA reduction is performed on the full dataset at once with N principal components. As a last step the images are scaled back with $B_{im} = 1/S_{im}$, derotated and stacked to create the final image.
- **SAP:** This method first performs SDI as described above without derotating and stacking. Afterwards it performs ADI as described above. Both reduction steps use $N/2$ principal components (where N is an even number) leading to N principal components used in SAP.
- **ASP:** This method first performs ADI as described above without derotating and stacking. Afterwards it performs SDI as described above. Both reduction steps use $N/2$ principal components (where N is an even number) leading to N principal components used in ASP.

During this thesis, the performance of these combinations will be investigated using various tests (see chapter 4). As every SDI step can be followed by an ADI step, or vice versa, there are many more combination possible. Some additional combinations were tested in chapter 4.6. For a clearer notation of those various combinations, the following shorthand is introduced: reducing a data set first with ADI (using N principal components) and afterwards with SDI (using M principal components) is written as $ADI(N) \rightarrow SDI(M)$. The special case of SAA using N principal components can be written as $(ADI\&SDI)(N)$. Examples of different ADI/SDI combinations would be: $SDI(3) \rightarrow ADI(3)$, $SDI(1) \rightarrow ADI(2) \rightarrow SDI(1)$ or $ADI(8) \rightarrow SDI(4) \rightarrow SDI(4)$.

As ADI splits the dataset into its wavelength channels, it will conduct a PCA reduction for each wavelength. For example, if $ADI(4)$ is used on SPHERE/IFS data a total of 39 PCA reductions with 4 principal components each will be used. As SDI splits the dataset into time component, it will conduct a PCA reduction for each time instance of the dataset. If the dataset has 100 images and is reduced with $SDI(4)$, this results in 100 PCA reductions with 4 principal components each. SAA does not split the dataset at all and therefore $(ADI\&SDI)(4)$ only uses 1 PCA reduction with 4 principal components. For comparison: using ASP with 4 principal components on a SPHERE/IFS observation with 100 images, uses 139 PCA reductions with 4 principal components each. This also means, that SDI is limited to 38 PCA components as every time instance taken with SPHERE/IFS has 39 frames. The consequences of this difference were analysed in chapter 4.2.

2.5 Background Contaminants

A problem in direct imaging are background sources within the FOV of the observation which resemble companions. SPHERE/IRDIS uses broadband filters and therefore the measured flux of background sources is indistinguishable from bound companions because of the temperature-distance degeneracy: an observed object has the same broadband-flux if it is hot and far away or colder and closer. To determine if the found object is a companion or a background source, its co-movement can be measured. A bound object stays approximately at the same position for several months (or even years) because the orbital period for objects with a distance of $>10\text{AU}$ to their host star are typically several decades. Background stars on the other hand have considerable relative velocities compared to the observed target and therefore their observed distance can change measurably. To measure the co-movement, a second observation is required typically several months later. An example of a co-movement analysis is taken from Bohn et al. [2020] and can be seen in figure 5.

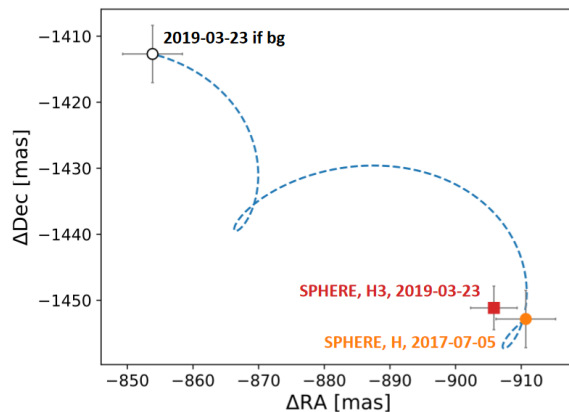


Figure 5: Co-movement analysis of the companion found around TYC 8998-760-1. The orange and red data points represent the measured relative position from two observations which were conducted 1.5 years apart. The black point represents the predicted position of the companion if it was a background source. Image taken from Bohn et al. [2020].

Another way to classify an object is via its absorption lines. Instruments like SINFONI⁴ or the upcoming ERIS⁵ can observe high resolution spectra of exoplanets which allow to analyse its absorption lines. The lines of astrophysical objects have very specific widths and depths and therefore can be used to classify them. Unfortunately, the low resolution of 39 wavelength channels over a maximum range of $0.95 - 1.68\mu\text{m}$ does not allow a detailed absorption line study.

⁴An overview of the instrument SINFONI is available at <https://www.eso.org/public/teles-instr/paranal-observatory/vlt/vlt-instr/sinfoni/>

⁵An overview of the instrument ERIS is available at <https://www.eso.org/public/teles-instr/paranal-observatory/vlt/vlt-instr/eris/>

2.6 Spectral Characterisation of Exoplanets

To investigate the formation, evolution and composition of exoplanets, it is important to characterise companions using spectral information. In this chapter a short summary on how to obtain exoplanetary spectra is given. Additionally, the importance of atmospheric models is explained.

Obtaining a Spectrum

The biggest advantage of SPHERE/IFS data compared to SPHERE/IRDIS is its capability to observe exoplanet spectra. In contrast to the advanced differential imaging techniques, all wavelength channels are treated as independent observations. Each channel can then be reduced individually using PynPoint to produce one final image per wavelength. If the companion is bright enough (see chapter 4.3), the flux for each wavelength can be directly determined using aperture photometry. This only works if the companions signal does not suffer from self-subtraction. The influence of self-subtraction was analysed in chapter 4.3.

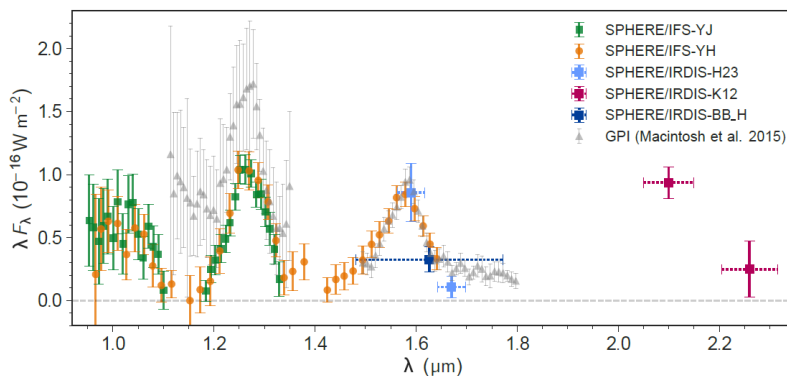


Figure 6: Spectrum of 51 Eridani b obtained by [Samland et al. \[2017\]](#) using SPHERE. Additionally, they compared their spectrum to the one obtained by [Macintosh et al. \[2015\]](#) who discovered 51 Eridani b with the Gemini Planet Imager (GPI).

Fainter targets require PCA to be detectable. Because the exoplanets signal can be reduced by the PCA reduction, simple aperture photometry would not result in an accurate measurement. To resolve this problem, the exoplanets intensity can be measured by injecting a negative companion into the data set and tuning its parameters until it exactly mirrors the real companion. If the negative companion is at the same position as the real exoplanet and has exactly the opposite brightness, they will cancel each other out and will no longer be visible in the final image. In PynPoint this is implemented using a simplex minimization algorithm which stepwise injects planets until, for example, the residual flux is close to zero. With this tools, it is possible to find and characterise even faint companions.

An example of the spectrum of 51 Eridani b obtained by [Samland et al. \[2017\]](#) using SPHERE/IFS in combination with SPHERE/IRDIS can be seen in figure 6.

Exoplanet Atmosphere Models

Exoplanet atmospheres are immensely complex systems. Their exact behaviour depends on macroscopic processes as well as microscopic processes, which makes them incredibly hard to predict and model. On earth itself, where we have the best possible observation conditions, the predictability of the weather does not range further than several days.

To tackle exoplanet characterisation, atmospheric models are developed and constantly improved. Their complexity ranges from simple black-bodies to highly advanced dynamic models considering hundreds of chemical actors. A detailed way to study atmosphere is by measuring their absorption lines and a typical spectrum has lines of various size. The limiting factor regarding which lines can be measured is the resolution of the spectrograph. For SPHERE/IFS the resolution is maximum $R \approx 50$. Therefore, all features with a FWHM less than $0.01\mu\text{m}$ are not reliably measurable with SPHERE/IFS. On the other hand, large absorption features (FWHM $> 0.02\mu\text{m}$) can be detected and are very useful to characterise the found object. Unfortunately, if those features are strong (opacity ≈ 1) and have a FWHM of more than $0.1\mu\text{m}$, the planetary signal can be too faint to be detected. In such cases only an upper limit can be determined which depends on the noise level of the image. To characterise exoplanets, it is important to know the limitations of the observations and choose models accordingly.

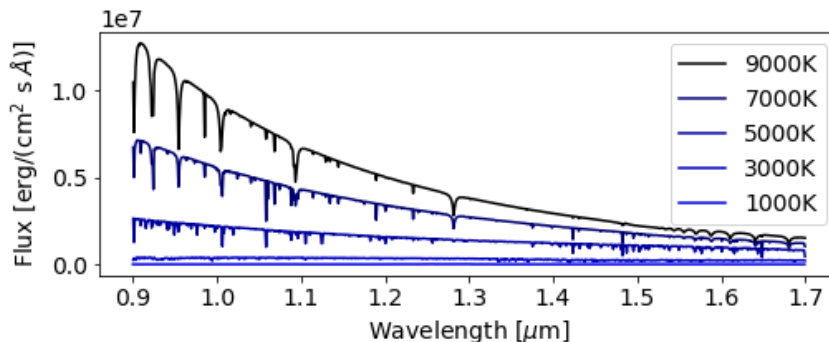


Figure 7: Examples of Bt-Settl models (Allard [2013]) with parameters $\log g = 4.0$, $\text{FeH} = 0.0$ and the displayed temperatures.

As one of the main goals of the thesis is to reject background stars, the type of object to be analysed is not a priori known. It could be a star with a bound planet, a double star system or a background source which just happens to be within the FOV. Therefore, models are required which span the range from planetary to stellar spectra. An example of such a model would be the Bt-Settl (Allard [2013]). It contains synthetic spectra for objects in a temperature range of 400 K to 70'000 K. Some example spectra can be seen in figure 7. Such models were used in chapter 5 to reject background contaminants.

PynPoint Modifications

PynPoint is a powerful python software package to evaluate SPHERE/IRDIS data (Amara et al. [2015], Stolker et al. [2019]). During this thesis, the advanced differential imaging techniques were implemented into its framework. PynPoint contains basic reduction steps (e.g. dark correction, flat calibration and image cropping) and many different processing methods. Most notably, it supports ADI and PCA for a sophisticated PSF reduction (see chapter 2.3). IFS data was not yet supported and thus the library was expended over the course of this thesis. This chapter lists the changes made to pre-existing PynPoint modules and the newly added functionalities which allow to evaluate SPHERE/IFS data similar to SPHERE/IRDIS data.

The here developed PynPoint version is available on GitHub⁶. Additionally, some of the here mentioned functionalities are currently being added to the official version of PynPoint. During this process they get further optimised and adjusted. Therefore, the modules mentioned in this chapter might differ slightly from the ones available in the official PynPoint version. Please refer to the official web page for the newest version⁷.

3.1 Basic PynPoint Functionalities

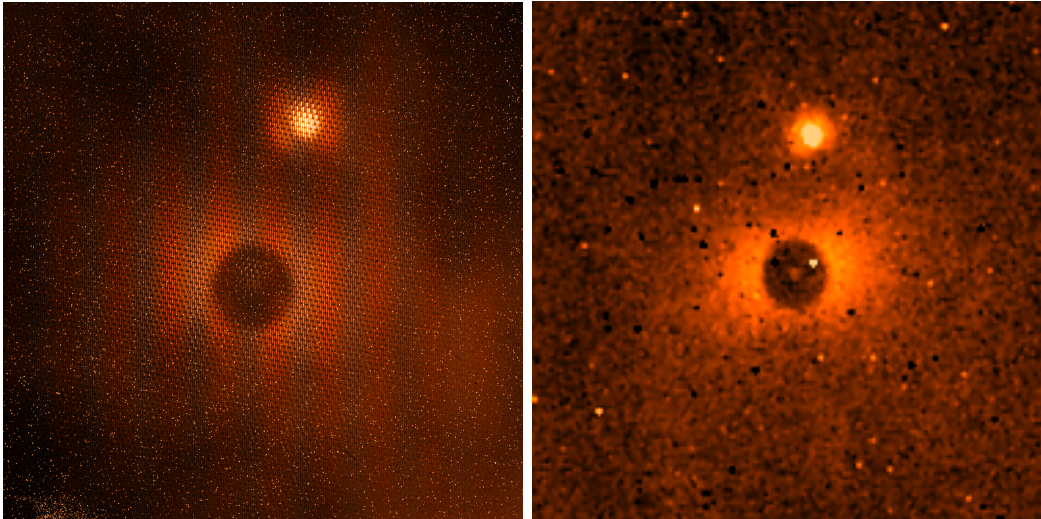
The basic input shape of raw SPHERE/IFS data is similar to SPHERE/IRDIS. The difference is that the SPHERE/IFS splits the incoming light into 39 wavelength channels and spreads them over the detector. A raw SPHERE/IFS image can be seen in figure 8a. The first step to evaluate the images is to flat and dark correct them as well as separate the individual wavelengths. EsoReflex provides these steps embedded into a graphical interface (Freudling et al. [2013]). All images used during this thesis were reduced using the 'SPHERE/IFS' pipeline of EsoReflex⁸. A single wavelength image after reduction with EsoReflex can be seen in figure 8b. There

⁶ Available at https://github.com/Kiefersv/PynPoint/tree/MasterThesis_Sven_Kiefer

⁷ Available at <https://pynpoint.readthedocs.io/en/latest/>

⁸ Available at <https://www.eso.org/sci/software/esoreflex/>

exist other reduction pipelines similar to EsoReflex but they were not added to PynPoint yet⁹.



(a) Raw SPHERE/IFS image containing all wavelength information (b) EsoReflex reduced image at wavelength $\lambda = 0.953 \mu m$

Figure 8: Comparison of SPHERE/IFS images before and after reduction using EsoReflex (Freudling et al. [2013]). The reduction creates one image per wavelength channel. The displayed star is 2MASS J 11555771-5254008 with a stellar type companion in the upper part of the image. (PI: A.J. Bohn)

Data Read In

SPHERE/IFS images shares most of their input parameters with SPHERE/IRDIS images. Therefore, only a few new parameters had to be added. The following additional information is needed to support wavelength specific evaluation:

- **LAMBDA0:** The wavelength in microns of the first image of a IFS data stack. Read in from FITS header; non-static float attribute.
- **LAMBDA0:** The wavelength difference between subsequent images in the IFS data stack. Read in from FITS header; non-static float attribute.
- **LAMBDA:** The wavelength of each frame from the IFS data stack. Calculated from LAMBDA0 and LAMBDA0 after read in; non-static float attribute.
- **DATCOR:** Contains the frame index number of the original images. Used to correct the assigned DATE from the EsoReflex pipeline. Read in from FITS header; non-static string attribute.

⁹The reduction pipeline VLTPF developed by A. Vigan (<https://github.com/avigan/VLTPF>) can also perform the basic reduction steps for SPHERE/IFS data but has not been implemented into PynPoint yet.

Slightly Adjusted PynPoint Modules

Many Pipeline modules do not depend on wavelength and thus can be used for SPHERE/IFS images with little or no adjustments. The following modules were tested and can be used for SPHERE/IFS images without further changes:

BadPixelMapModule	BadPixelSigmaFilterModule
ClassicalADIModule	CropImagesModule
FakePlanetModule	FitCenterModule
FitsWritingModule	PSFpreparationModule
ReplaceBadPixelsModule	ShifImagesModule
SimplexMinimizationModule	SortParangModule
StarAlignmentModule	StarExtractionModule
WaffleCenteringModule	

Some modules were slightly adjusted as they did not handle SPHERE/IFS information correctly. The following modules were slightly changed:

- **AngleCalculationModule:** Correction of the SPHERE/IFS angle calculation. The angles are now calculated according to the SPHERE manual page 96 of [Wahhaj et al. \[2019\]](#) including the necessary corrections for the EsoReflex pipeline.
- **DerotateAndStackModule** Attribute assignment changed to correctly handle wavelength information.
- **SortParangModule** Attribute assignment changed to support the LAMBDA attribute.

All modules can either be used on all wavelength simultaneously using the `Pypeline.add_module()` function or used on each wavelength individual using the `IfsSupportFunction` (see chapter 3.3). All modules which do not depend on the wavelength produce exactly the same output in both cases.

3.2 New Adjusted Modules

Not all PynPoint modules were suitable for IFS data and some functionalities were missing. Therefore, new modules were added during this thesis to allow SPHERE/IFS data handling. This chapter lists all modules which add basic functionalities. Some are similar to existing PynPoint modules and, for an official PynPoint release, might be merged together. All modules are listed with their dependencies and a short description. Modules which contain functionalities developed during this thesis are listed in chapters 3.3, 3.4, 3.5 and 3.6.

- **ClassicalSdiModule** (*name_in: str, image_in_tag: str, res_median_tag: str = None, res_mean_tag: str = None, median_back_tag: str = None, mean_back_tag: str = None*)

This module was newly added¹⁰. It scales the input images according to their wavelength and averages them to produce a reduction frame. Afterwards the reduction frame gets scaled back and subtracted from the input images. As a last step the images are scaled back, derotated and stacked to create the final image.

- **ContrastCurveModule** (*name_in: str, image_in_tag: str, psf_in_tag: str, contrast_out_tag: str, separation: Tuple[float, float, float] = (0.1, 1., 0.01), angle: Tuple[float, float, float] = (0., 360., 60.), threshold: Tuple[str, float] = ('sigma', 5.), psf_scaling: float = None, flux_filter: str = 'ND_0.0', aperture: float = 0.05, pca_number: int = 20, cent_size: float = None, edge_size: float = None, extra_rot: float = 0., residuals: str = 'median', snr_inject: float = 100., processing_type: str = 'adi', **kwargs: float*)

This module was adjusted to include the advanced differential imaging techniques (see chapter 4.2). Similar to the PCA PSF Reduction (see chapter 3.4), the differential imaging techniques can be selected with the `'processing_type'` parameter. Depending on the selected `'processing_type'`, it either calculates one final contrast curve using all wavelengths or it calculates a contrast curve for each wavelength. Multiprocessing over all wavelengths was added to reduce computational time if run on a cluster.

- **IfsScalingModule** (*name_in: str, image_in_tag: str, image_out_tag: str, scaling = Union[Tuple[float, float, float], Tuple[None, None, float], Tuple[float, float, None]] = (1.0,1.0,1.0), angle = 0, pixscale = False*)

This module is similar to the ScaleImagesModule. Additionally, it can scale images along all directions. The scaling direction can be set with `'angle'` and therefore allows to correct for distortion effects not aligned with the axis of the images. This module allows to apply the necessary corrections for SPHERE/IFS data according to Wahhaj et al. [2019] page 69.

- **PlotContrastCurve** (*name_in: str, image_in_tag: str, data_index: int, error_index: int = None, file_name: str = None, plot_title: str = None, output_dir: str = None*)

This module was newly added to simplify handling the output from the SelectiveContrastCurveModule or the SdiAperturePhotometryModule. It creates a simple plot with the given parameters. Its main use is to quickly plot contrast curves for setting up a Pipeline.

- **SdiAperturePhotometryModule** (*name_in: str, image_in_tag: str, psf_in_tag: str, flux_position_tag: str, rough_position: List[int], flux_filter: str = 'ND_0.0', psf_scaling: float = None, pixscale_corr: ufloat = ufloat(0.01227, 0.00002), TN: ufloat = ufloat(-1.75,0.1), cutout_size: int = 21, fit_each_image: bool = False, aperture_size: str = "fwhm"*)

¹⁰The ClassicalSdiModule was implemented for completeness but was not further investigated. The SDI reduction in chapter 4 uses PCA analysis and was included in the PcaPsfSubtractionModule (see chapter 3.4).

This module is similar to the AperturePhotometryModule and calculates the contrast between a companion candidate and its host star. Several functionalities were added to simplify SPHERE/IFS data handling. If the flux filter is specified and the PSF images are given, the calculation of the PSF scaling factor can be done internally. Similar to Samland et al. [2017], it uses a Gaussian approximation of the neutral density filters spectrum. Additionally, a true north correction and error calculation were added. The output is given as contrast to the host star. The differential imaging techniques can be selected with the `'processing_type'` parameter.

- **SdiSimplexMinimizationModule** (*name.in: str, image.in.tag: str, psf.in.tag: str, res.out.tag: str, flux.position.tag: str, position: Tuple[int, int], magnitude: float, psf.scaling: float = None, flux.filter: str = 'ND_0.0', merit: str = 'hessian', aperture: float = 0.1, sigma: float = 0.0, tolerance: float = 0.1, pca.number: Union[int, range, List[int]] = 10, cent.size: float = None, edge.size: float = None, extra.rot: float = 0., residuals: str = 'median', reference.in.tag: str = None, processing.type: str = 'Wadi'*)

This module is similar to the SimplexMinimizationModule and calculates the contrast between a companion candidate and its host star. It supports multi wavelength output and multiprocessing over all wavelengths to reduce the computational time. If the flux filter is specified and the PSF images are given, the calculation of the PSF scaling factor can be done internally. Similar to Samland et al. [2017], it uses a Gaussian approximation of the neutral density filters spectrum. The differential imaging techniques can be selected with the `'processing_type'` parameter.

- **SelectGivenAtributesModule** (*name.in: str, image.in.tag: str, selected.out.tag: str, attribute.tag: str, attribute.value: str*)

This module is similar to the SelectByAtributesModule. It selects all frames from `'image.in.tag'` with an `'attribute.tag'` value of `'attribute.value'`. The selected frames get saved under the `'selected.out.tag'`. This module is a core function of the IFSsupportFunction (see chapter 3.3) and is used to split datasets into wavelength channels.

- **WaffleCenteringModule** (*name.in: str, image.in.tag: str, center.in.tag: str, image.out.tag: str, radius: float = 45, l.min: float = 1, pattern: str = None, size: float = None, center: Tuple[float, float] = None, angle: float = 0, sigma: float = 0.06, dither: bool = False*)

This module was adjusted to support SPHERE/IFS data. The angle parameter (in degree) allows to use centring patterns other than `'x'` and `'+'`. To increase the centring accuracy over all wavelengths, this module automatically calculates the wavelength specific scaling of the centring pattern. For SPHERE/IFS data, the `'radius'` corresponds to the separation of the waffle spots for `'l.min'` (shortest observed wavelength).

All modules can either be used on all wavelength simultaneously using the `Pipeline.add_module()` function or used on each wavelength individual using the `IfsSupportFunction` (see chapter 3.3). All modules which do not depend on the wavelength produce exactly the same output in both cases.

3.3 IFS Support Function

The `IfsSupportFunction` is a helper for IFS data handling. It splits data sets according to a given attribute (typically the wavelength) before applying one or more PynPoint modules to each subset and afterwards recombines them. This allows to process SPHERE/IFS data similar to SPHERE/IRDIS. An example on how to use the `IfsSupportFunction` to clean bad pixels and sort and derotated IFS data with PynPoint can be seen in figure 9.

IfsSupportFunction (*image_in_tag*: List[str], *image_out_tag*: List[str], *pipeline*: Pipeline, *mod_args*: List[Dict[*args]], *path_lam*: str = None, *skip_split* = False, *print_out*: bool = True, *split_argument*: str = 'LAMBDA')

- *image_in_tag*: A list of tags which are given to the function and split according to *split_argument*. All tags used by modules inside the `IfsSupportFunction` but defined outside of it must be given here. If not, PynPoint will raise an error during the validation step.
- *image_out_tag*: A list of tags which will be written as output. Any tag used in the `IfsSupportFunction` can be written as output. The output tags are created by recombining the split datasets and saved in the database with the prefix 'WEOUT_' to prevent tag reuse. For example, if *image_out_tag* = ['test'], a database entry with the tag 'WEOUT_test' is created.
- *pipeline*: The Pipeline to which the modules listed in *mod_args* are added. This Pipeline will not be executed within the `IfsSupportFunction`.
- *mod_args*: A list of dictionaries with the arguments of the modules which are to be added to '*pipeline*'. The modules will be added in the same order as they are in the dictionary. The `IfsSupportFunction` supports default arguments and the optional parameters can be missing in the dictionary.
- *path_lam*: The `IfsSupportFunction` needs to run a preliminary Pipeline to determine the list of splitting parameters. If the *path_lam* is set to None, the input directory of '*pipeline*' is used. To reduce computational intensity, one can set '*path_lam*' to a folder with a representative subset of the images. The `IfsSupportFunction` cannot be executed if the subset does not contain all possible parameters of the chosen splitting argument.
- *skip_split*: A boolean to set whether the read in of the '*image_in_tag*' should be skipped. Can only be set to True if the `IfsSupportFunction` was executed before and the split datasets are currently stored in the database of the '*pipeline*'.

```

1 import pynpoint as pp
2
3 pype = pp.Pypeline()
4 mods = []
5
6 # --- Data read in
7 im_reading_mod = pp.FitsReadingModule(name_in="im_reading_mod",
8                                     input_dir = '\science',
9                                     image_tag = "im")
10
11 # --- bad pixel cleaning
12 im_badpixel_dict = {'module': 'BadPixelSigmaFilterModule',
13                   'name_in': "im_bp_dict",
14                   'image_in_tag': 'im',
15                   'image_out_tag': 'im_bp'}
16
17 # --- Angular calculation
18 im_anglecalc_dict = {'module': 'AngleCalculationModule',
19                    'name_in': 'im_ac_dict',
20                    'data_tag': 'im_bp',
21                    'instrument': 'SPHERE/IFS'}
22
23 # --- Derotate and Stack each wavelength
24 im_derotstack_dict = {'module': 'DerotateAndStackModule',
25                      'name_in': 'im_der_dict',
26                      'image_in_tag': 'im_sc',
27                      'image_out_tag': 'im_fc',
28                      'stack': 'median'}
29
30 # Add pypline modules
31 pype.add_module(im_reading_mod)
32
33 mods.append(im_badpixel_dict)
34 mods.append(im_anglecalc_dict)
35 mods.append(im_derotstack_dict)
36
37 # Run IFS Support Module
38 pp.IFSsupportModule(image_in_tag=['im'],
39                   image_out_tag=['im_sc'],
40                   pipe=pype,
41                   mod_args=mods,
42                   path_lam='\lam',
43                   skip_split = False,
44                   print_out = True,
45                   split_argument = 'LAMBDA')
46
47 # Run Pypeline
48 pype.run()

```

Figure 9: Example on how to use the IFSsupportFunction. Used to clean bad pixels and sort and derotate the data for each wavelength channel.

- *print_out*: A boolean to set whether all '*image_out_tag*' should be written as FITS file. In any case, the tags listed in '*image_out_tag*' will be combined and written into the database of the '*pypeline*'.
- *split_argument*: The argument which is used to split the input datasets. If *split_argument* = '*LAMBDA*', the input data is split into wavelength channels.

The `IfsSupportFunction` is not a PynPoint module. It is a function used to set up other modules and thus must be executed before the main run of the Pypeline. During the `IfsSupportFunction`, an independent Pypeline is run to collect all splitting parameters. This independent Pypeline does not interfere with other Pypelines.

Because loading data in and out of the `IfsSupportFunction` can be computationally intensive for large datasets, it is advised to use only one `IfsSupportFunction` if possible.

3.4 PCA PSF Reduction

The observed position of a physical object (e.g. stars and exoplanets) does not depend on wavelength whereas the stellar PSF is wavelength depended. In SDI this difference is used to align the stellar PSF and radially misalign possible companions by rescaling the images with a factor $S(\lambda)$. For a detailed description of SDI see chapter 2.4. In this section, the scaling factor $S(\lambda)$ is derived and used to derive the radial displacement caused by the scaling. Additionally, the azimuthal displacement caused by the rotating FOV is derived as well. Lastly, the implementation of SDI into PynPoint is described.

Scaling Factor

The scaling factor $S(\lambda)$ needs to be derived before using it to scale the images to align the stellar PSF. The scaling of the PSF is derived from the Rayleigh criterion (Smith [2013]) and can be written as:

$$\beta(\lambda) = 1.22 \frac{\lambda}{\mathcal{D}} \quad (4)$$

Where \mathcal{D} is the telescopes diameter and λ the wavelength of a given image from the dataset. Using the inverse of $\beta(\lambda)$ to scale the images therefore aligns the residual star light from the stellar PSF. Because only relative scaling between the images is needed to align them, the scaling factor can be defined as:

$$S(\lambda) = \frac{\beta(\lambda_{ref})}{\beta(\lambda)} = \frac{1.22\lambda_{ref}/\mathcal{D}}{1.22\lambda/\mathcal{D}} = \frac{\lambda_{ref}}{\lambda} \quad (5)$$

$$\lambda_{ref} := \max\{\lambda\} \quad (6)$$

For this thesis the reference wavelength λ_{ref} was chosen as the largest wavelength in the dataset, thus resulting in an up-scaling of all images with a shorter wavelength ($S(\lambda) \geq 1, \forall \lambda$). Theoretically any wavelength can be chosen as reference. For

example, choosing $\lambda_{ref} = \min\{\lambda\}$ would result in a down-scaling of images ($S(\lambda) \leq 1, \forall \lambda$). This would result in smaller images and therefore shorten the computation time but would also lead to an under-sampling of the residual star light.

Radial and Azimuthal Displacements

The radial displacements Δr of a companion are due to the rescaling of the images according to equation 5. Therefore, the total radial displacements Δr can be calculated with the following equation:

$$\Delta r = S(\lambda)r - r = r \frac{\lambda_{max}}{\lambda_{min}} - r = r \left(\frac{\lambda_{min} + \Delta\lambda}{\lambda_{min}} - 1 \right) \quad (7)$$

$$\Delta r = r \frac{\Delta\lambda}{\lambda_{min}} \quad (8)$$

On the other hand, the azimuthal displacements Δrot of a companion are due to the field rotation during the observation. Because the companion shifts its position over the circular segment with an angle of $\Delta\alpha$ and radius r , Δrot can be calculated with the following equation:

$$\Delta rot = 2\pi r \frac{\Delta\alpha}{360^\circ} \quad (9)$$

To be able to compare results between datasets, all displacements can also be given in FWHM of the PSF. The FWHM can be calculated using the flux images of the observed object. Using equations 8 and 9 and setting $\Delta r = \Delta rot = \text{FWHM}$, the rotation and wavelength ranges equivalent to a displacement of 1 FWHM are:

$$\Delta\alpha_{FWHM} = (\text{FWHM}) \frac{360^\circ}{2\pi r} \quad (10)$$

$$\Delta\lambda_{FWHM} = (\text{FWHM}) \frac{\lambda_{min}}{r} \quad (11)$$

PynPoint Implementation

The scaling factor derived in this chapter is used to implement SDI into the PcaPsf-SubtractionModule of PynPoint. To perform SDI on a dataset, all images are first scaled according to the scaling factor $S(\lambda)$. Afterwards, the scaled images are divided into their time channels which are then each processed using a PCA reduction with a given number of principal components. This process is comparable to the already implemented ADI but instead of applying PCA on each wavelength channel, it is applied on each time channel. This is possible because both techniques use small displacements (SDI radially; ADI azimuthally) of a possible companion to model and subtract residual star light. After the PCA reduction, the images are scaled back using the inverse of the scaling factor $S(\lambda)$ therefore realigning a possible companion. To create the final image, all processed images are derotated and stacked.

To execute the advanced differential imaging techniques, ADI and SDI can be combined. SAP (or ASP) are executed by first performing SDI (or ADI) before applying ADI (or SDI). To execute SAA, the same steps are applied as for SDI but

instead of splitting the dataset into time channels, SAA uses one PCA analysis on the whole, scaled dataset.

To select the advanced differential imaging technique within the `PcaPsfSubtractionModule`, the following keywords can be used:

- `"Tnan"` equivalent to classical ADI, no PCA is used for this method
- `"Oadi"`: performing `ADI(pca_number)` ignoring the wavelength information
- `"Tadi"` or `"Wadi"`: performing `ADI(pca_number)` on each wavelength channel
- `"Tsdi"` or `"Wsdi"`: performing `SDI(pca_number)`
- `"Tsaa"` or `"Wsaa"`: performing `(ADI&SDI)(pca_number)`
- `"Tsap"` or `"Wsap"`: performing `ADI(pca_number) → SDI(pca_number)`
- `"Tasp"` or `"Wasp"`: performing `SDI(pca_number) → ADI(pca_number)`

The reductions techniques to the corresponding keywords are described in chapter 2.4. The prefix of the keywords defines the output form. If set to 'W', a final image for each wavelength is produced. If set to 'T', one final image averaged over all wavelengths is produced. The other input parameters of the module are unchanged and are described in the official PynPoint documentation¹¹. The `PcaPsfSubtractionModule` parameters can be seen below including an explanation of the newly added ones.

PcaPsfSubtractionModule (*name_in: str, images_in_tag: str, reference_in_tag: str, res_mean_tag: str = None, res_median_tag: str = None, res_weighted_tag: str = None, dmp_stim_tag: str = None, res_rot_mean_clip_tag: str = None, res_arr_out_tag: str = None, basis_out_tag: str = None, pca_numbers: Union[range, List[int], np.ndarray] = range(1, 21), extra_rot: float = 0., subtractmean: bool = True, processing_type: str = 'Oadi'*)

- `dmp_stim_tag`: Tag of the database entry with the STIM map as proposed by [Pairet et al. \[2019\]](#). Not calculated if set to none. More details can be found in chapter 3.5.
- `processing_type`: Keyword of the processing type. The supported keywords are listed in this chapter.

¹¹Available at <https://pynpoint.readthedocs.io/en/latest/>

3.5 Companion Detection

To calculate the SNR of an exoplanet, a detection map is needed. In PynPoint the final images are created by taking the median of the derotated images. The disadvantage of this method is that it only considers the brightness of a companion and assumes the noise to be a Gaussian random field. In this chapter two other methods to determine a detection are described.

STIM Detection Map

The STIM detection map is based on the work of [Pairet et al. \[2019\]](#). They investigated the noise of direct imaging data to find a better estimation than a simple Gaussian random field. They claim their detection map leads to a lower false positive rate and that it is especially useful to detect companions at small separations.

The STIM detection map was implemented into the `PcaPsfSubtractionModule` of PynPoint. If selected, the module first applies a PCA reduction as described in chapter 3.4 but does not stack the processed images into a final image. Instead, the images are only derotated and afterwards the mean and standard deviation of each pixel value along the time dimension is calculated. Afterwards, the final detection map is produced by dividing the mean through the standard deviation for each pixel. The result is saved under the `dmp_stim_tag`. This detection map does not depend on wavelength and therefore works for both SPHERE/IFS and SPHERE/IRDIS.

The STIM module was tested during this thesis and the results can be found in chapter 4.7.

CompanionFinderModule (*name_in: str, image_in_tag: str, psf_tag: str, correlation_out_tag: str = None, sigma_out_tag: str = None, detection_lim: float = None, average_psf: str = None*)

This module assumes that the host star and the companion have identical PSF's. Thus, to find a companion in a noisy image, the images are cross correlated with the stellar PSF. Assuming the noise is similar to a Gaussian random field, the companions cross correlation value can be significantly higher.

As this method searches the final image for a PSF pattern, it achieves the clearest detection if the PSF is complex. Many coronagraphs which are currently researched use very specific patterns to filter the host stars light and thus produce very complex PSF patterns which are easier to distinguish from background noise. The main disadvantage of this method is that speckles can have a similar shape to the PSF. This leads to a higher false detection rate near the host star. A more advanced way to search for companions via pattern search would be forward modelled matched filters as presented by [Ruffio et al. \[2017\]](#). They calculate a forward model of the PSF at every position to include the effects of processing on the PSF shape. This method is not included in the `CompanionFinderModule`.

This module was tested on Beta Pictoris b and 51 Eridani b (see chapter 4) and Ob1 (see chapter 6). Because it did not result in higher SNRs than already present in the final images, this module was not further investigated.

3.6 Spectral Characterisation

An important addition from IFS data is spectral analysis and background star rejection (see chapter 2.5). Therefore, the model based rejection was developed over the course of this thesis (see chapter 5). The implementation of this method into PynPoint was done by implementing a new module: SpectralCharModule.

Before the SpectralCharModule can be used, the contrast of a companion candidate and its host star needs to be calculate using either the AperturePhotometryModule or the SdiSimplexMinimizationModule. To convert this relative measurements into the companion candidate's spectrum, a stellar spectrum of the host star is required which can be obtained, for example, from the VOSA web page¹² (Bayo et al. [2008]). Using the contrast measurements and the host star's spectrum, the module can calculate the companion candidate's spectrum.

To classify companion candidates as bound or background and to determine its rough characteristics, the model based rejection is used which was developed during this thesis (see chapter 5). To perform the model based rejection, this module fits the observed spectrum to a low resolution model grid ($\Delta T = 200\text{K}$, $\Delta \log g = 0.5$, $\Delta \text{FeH} \approx 0.5$) of the Bt-Settl model¹³ (Allard et al. [2012]) over the range of $T_{\text{eff}} = [2000\text{K}, 9800\text{K}]$, $\log g = [2.0, 5.0]$ and $\text{FeH} = [-2.0, 0.0]$. Afterwards the correlation between model and observation is calculated to find the best fit and thus a rough estimation of the objects parameters (temperature, Metallicity and $\log g$). The distance to the candidate is determined via the fitting parameter of the best fit model according to the calculations in chapter 5.

SpectralCharModule (*name_in*: str, *image_in_tag*: str, *method*: str, *stellar_model*: str, *prop_factor*: float = None, *error_simplex*: float = None, *error_cutting*: float = None, *mol_fit*: str = full, *manual_data_points_mag*: List[List[float]] = None, *output_dir*: str = None)

- *name_in*, *image_in_tag*: Parameters used for database handling.
- *method*: Define the format of the data in *image_in_tag*. Currently supports input from SdiAperturePhotometryModule ('aperture') and SdiSimplexMinimizationModule ('simplex').
- *stellar_model*: Path to the text file containing the spectrum of the host star. The Flux must be given in [ergs/(s cm² Å)] and the wavelength in [Å].
- *prop_factor*: Stellar correction factor. Used to correct the *stellar_model* for the stars distance and radius. Not used if set to None.
- *error_simplex*: Used to set the error on the contrast calculations of the *image_in_tag* data. Not needed if *method* = 'aperture' because the SdiAperturePhotometryModule calculates the error internally.

¹²Available at <http://svo2.cab.inta-csic.es/theory/vosa/>

¹³The Bt-Settl model was selected because of its parameter range. Theoretically, this module would work with any model grid. Furthermore, different models could be combined to one model grid.

- *error_cutting*: Value used to increase small errors to prevent over fitting. The *error_cutting* value describes how many standard deviations below the mean of the error the threshold should be set. Afterwards, all errors smaller than the threshold are set to the threshold value. Not used if set to None.
- *mol_fit*: Type of fitting used for the model based rejection¹⁴. The keyword is used to define two wavelength ranges: one to fit the model grid to the observation and the second one to calculate the correlation. Currently two types are supported:
 - 'full': Uses the whole spectral range to fit the model and calculate the correlation.
 - 'H2O': Uses the range 1.1 μm - 1.25 μm to fit the model grid to the observation and the range 1.3 μm - 1.6 μm to calculate the correlation.
- *manual_data_points_mag*: List with additional data points to be added to the spectrum (e.g. from SPHERE/IRDIS). The list should be of the following form for data points 1 to N: $[[\lambda_1, \dots, \lambda_N], [mag_1, \dots, mag_N], [\Delta\lambda_1, \dots, \Delta\lambda_N]]$
- *output_dir*: Path to the directory where the output should be stored.

3.7 The Pipelines

To find and characterise exoplanets in SPHERE/IFS data, different PynPoint Pipelines were set up. Because SPHERE/IFS data is already partly reduced by EsoReflex, less PynPoint modules are necessary to perform the basic reduction steps as for SPHERE/IRDIS data. An example including all Pipelines described in this chapter can be found in appendix B, listing 1.

Pipeline 1:

The following Pipeline is used to read in and prepare the science and flux images of SPHERE/IFS data including all necessary instrumentation correction. Additionally, it cleans the images of bad pixels using sigma clipping and centres the science images using the centring frames. In the end, the science images are cropped.

- 1) *FitsReadingModule*: Read in science, flux and centring frames separately.
- 2) *BadPixelSigmaFilterModule*: Remove bad pixels from all images using sigma clipping.
- 3) *IfsScalingModule*: Correct all images for distortion caused by the instrument according to the SPHERE manual page 69 of [Wahhaj et al. \[2019\]](#).
- 4) *AngleCalculationModule*: Calculate the paralytic angle of all images according to the SPHERE manual page 69 of [Wahhaj et al. \[2019\]](#).

¹⁴For further explanation on how to use this parameter see chapter 5.3: Molecular Band Fitting

- 5) *WaffleCentringModule*: Centre science images using one centring frame per wavelength. The 'radius' and 'L_min' parameter are given by the instrument and are the same for all observations with SPHERE/IFS. This module must be executed within the `IfsSupportFunction` because the centring frames are wavelength specific.
- 6) *SortParangModule*: Sort science images using the PARANG attribute.
- 7) *DerotateAndStackModule*: Derotates science images using the PARANG attribute. The resulting output is used to check the quality of the reduction.
- 8) *CropImagesModule*: Resizes science images to reduce the computational intensity by later modules. The final images should have an image size of at least 5 times the predicted separation of the companion because of the FOV loss caused by SDI (see chapter 2.4).

Except for the bad pixel cleaning parameters and the crop size of the images, all input parameters are SPHERE/IFS specific. Therefore, this Pipeline can be used for all SPHERE/IFS datasets with minimal tuning.

Pypeline 2:

To measure the flux of the host star, flux images are taken. To avoid covering the star with the coronagraph, the star is offset from the centre. The following Pipeline is used to centre the flux images around the star, average them to one image per wavelength and crop them to a reasonable size.

- 1) *StarExtractionModule*: Locate the host star's position in all flux images and crop the images. This module requires the manual input of the approximate position of the star in the flux images.
- 2) *StarAlignmentModule*: Align flux images using cross correlation in Fourier space.
- 3) *FitCenterModule*: Derive position of the host star in flux images.
- 4) *ShiftImagesModule*: Centre flux images around the centre calculated in the previous module.
- 5) *SortParangModule*: Sort science images using the PARANG attribute.
- 6) *DerotateAndStackModule*: Derotate science images using the PARANG attribute. The resulting output is used to check the quality of the reduction.
- 7) *DerotateAndStackModule*: Average flux images to produce one flux image per wavelength. This module must be executed within the `IfsSupportFunction` to ensure stacking the images correctly.
- 8) *CropImagesModule*: Resize flux images. Ideally the flux images should have the same size as the science images. If this is not possible, they can be smaller.

Most of the module parameters used in the above Pipeline are universal for all datasets (or only need slight adjustments). The only exception is the stars position in the flux images which can differ for each observation¹⁵.

Pipeline 3:

After preparing the images, a PCA reduction can be used to remove residual star light and remaining instrument effects. The `PcaPsfSubtractionModule` contains all important PCA reduction steps and can directly create the final images. This module includes the newly added advanced differential imaging techniques. See chapter 2.4 for a description of the different techniques and chapter 3.4 for their implementation into PynPoint.

- 1) *PcaPsfSubtractionModule*: Process the input data according to chapter 3.4. To find companions, either the average over all processed images or the STIM detection map can be used.

Because it is not a priori clear which advanced differential imaging technique achieves the best results, *'processing_type'* parameter and the number of principal components *'pca_numbers'* allow to easily switch between them.

Pipeline 4:

To calculate the spectrum of a companion, two cases have to be distinguished: bright companions and faint companions. A companion is considered bright if its signal has a $\text{SNR} > 5$ even if no PCA is used. To determine the spectrum of bright companions, the following PynPoint modules are used in the given order:

- 1) *DerotateAndStackModule*: Derotate the reduced science images and average them on each wavelength channel separately. This module must be executed within the `IfsSupportFunction` to ensure correct wavelength handling
- 2) *SdiAperturePhotometryModule*: Calculate the position and contrast of the companion to its host star. The position is calculated by fitting a Gaussian around a rough estimation of a possible companion's position. The contrast is calculated using aperture photometry. Because this calculation has to be done for each wavelength separately, this module must be executed within the `IfsSupportFunction`.
- 3) *SpectralCharModule*: Calculate flux and Vega magnitude spectrum. Additionally, this module can be used to classify found objects as bound or background using model based rejection (see chapter 5).

¹⁵Pypelines 1 and 2 include only preparation steps and therefore can be used before applying further Pypelines.

Pypline 5:

Faint companions are harder to detect and thus PCA is necessary. Aperture photometry is not suitable for PCA reduced images as the signal of the companion might suffer from self-subtraction (see chapter 4.3). The *SdiSimplexMinimizationModule* uses simplex minimization to stepwise inject fake negative planets at the position of a possible companion. If they cancel each other out completely, the position of the fake companion is the same as the real one and their magnitudes are the exact opposite of each other. To execute this minimization the following PynPoint modules are used in the given order:

- 1) *PSFpreparationModule*: Apply centre and edge masks to minimise the influence of instrument artefacts like the coronagraph and reduce computational intensity.
- 2) *SdiSimplexMinimizationModule*: Calculate the contrast between host star and companion for each wavelength using simplex minimization¹⁶. The error is either given by the stopping criteria of the minimization process or the detection limits of the image.
- 3) *SpectralCharModule*: Calculate flux and Vega magnitude spectrum. Additionally, this module can be used to classify found objects as bound or background using model based rejection (see chapter 5).

Pypline 6:

To determine the detection limits, the contrast curve can be calculated. This is done by injecting fake planets in various position and processing them equivalent to the *PcaPsfSubtractionModule*. To calculate the contrast curve, the following PynPoint modules can be used:

- 1) *ContrastCurveModule*: Calculates the contrast curves according to the input parameters. The spatial resolution can be varied but the computational time increases significantly with higher resolutions. The computation time of the *ContrastCurveModule* strongly depends on the input image size, therefore cropping the images to a reasonable size helps to reduce its computational intensity¹⁷.
- 2) *PlotContrastCurveModule*: Plots the contrast curve from the results of the previous module. This module requires a stellar spectrum of the host star which can be obtained from the VOSA web page¹⁸ (Bayo et al. [2008]).

¹⁶It is not required to use this module within the *IFSsupportFunction* as it can handle separate wavelength channels internally

¹⁷The image size should be at least 5 times the largest selected separation (see chapter 2.4)

¹⁸Available at <http://svo2.cab.inta-csic.es/theory/vosa/>

Testing Differential Imaging

In this chapter, the advanced differential imaging techniques listed in chapter 2.4 are tested. The three targets Beta Pictoris, 51 Eridani and HR 8799 were selected as test targets because they have publications to compare the results with. First it is tested, which technique detects the companions with the highest SNR and which technique achieves the most favourable contrast. Afterwards, the techniques performance depending on integration time Δt , total rotation $\Delta\alpha$, wavelength range $\Delta\lambda$ and target brightness Δmag is analysed. Additionally, the performance of the STIM module and the iterative usage of PCA was tested. All tests were conducted using the implementation of the advanced differential imaging techniques into PynPoint as described in chapter 3.

Table 1: All observations were performed with SPHERE/IFS (PI: J. Beuzit). DIT stands for detector integration time and NDIT is the total number of images taken. Each dataset has a total rotation of $\Delta\alpha$. Each image contains 39 wavelength frames equally spread over the wavelength range λ . The atmospheric seeing is given as approximate value for the atmospheric distortions during the whole observation.

Object Name	ESO ID	Date	DIT[s] x NDIT	$\Delta\alpha$ [$^\circ$]	λ [μm]	Seeing["]
Beta Pictoris	096.C-0241(B)	2015-11-30	4 x 760	41.1	0.95-1.35	≈ 1
HR 8799	095.C-0298(D)	2015-09-28	16 x 256	23.8	0.95-1.68	≈ 1
51 Eridian	198.C-0209(J)	2017-09-28	32 x 154	52.0	0.95-1.68	< 0.8

Of the three targets, Beta Pictoris has the brightest exoplanet with an absolute magnitude of 12.56 ± 0.08 in the J-band (Chilcote et al. [2017]). In the selected dataset, Beta Pictoris b is at a separation of 0.249 ± 0.001 arcsec (Wang et al. [2016]). The whole dataset contains 760 images which is an additional advantage as it can be split into different subsets depending on the tests. Detailed information about how the subsets were chosen is given in the description of each test.

The exoplanets of HR 8799 and 51 Eridani are more difficult targets because they are fainter than Beta Pictoris b. 51 Eridani b has an absolute magnitude of

17.40 ± 0.71 in the J-band and is at a separation of 0.455 ± 0.006 arcsec (Rosa et al. [2015]). HR8799 has the additional advantage that two companions are within the FOV of SPHERE/IFS. The closer companion HR 8799 e is at a separation of 0.381 ± 0.007 arcsec and is therefore entirely within the FOV for all differential imaging techniques. It has an absolute magnitude of 15.42 ± 0.21 in the J-band. The second companion HR 8799 d is at a separation of 0.654 ± 0.007 arcsec and is therefore only partially within the FOV. It has a magnitude of 15.61 ± 0.37 in the J-band (Separations taken from Apai et al. [2016]; Magnitudes taken from Zurlo et al. [2016]). The definition of partial FOV is given in chapter 2.4.

An important factor for all tests was the computational time of the advanced differential imaging techniques implemented into PynPoint because it limited the number of tests which could be conducted. In cases where only one target could be selected, the dataset of Beta Pictoris was chosen because its small separation allowed to crop the images to a small size (120x120 pixel). This reduced the computational time while still keeping Beta Pictoris b in the full FOV.

The signal to noise ratio (SNR) for all tests was calculated using the `get_false_alarm_probability` function of PynPoint. The function uses aperture photometry to calculate the signal at the position of the companion and compares it with the noise of reference apertures at the same radius. For the exact implementation see appendix B, listing 2.

4.1 Iterative PCA

In direct imaging, residual star light can be reduced considerably using PCA. Normally, all PCA components are fitted and subtracted at the same time (single PCA) but it is also possible to apply them iteratively (iterative PCA). In this chapter, the difference between single PCA and iterative PCA is analysed. An example showing the difference between the two PCA methods performed on a subset of Beta Pictoris containing 132 images over an angular range of 37.6° can be seen in figure 10.

The difference between single and iterative PCA is important because iterative PCA enables to use different differential imaging techniques after each other. In fact, the processing types SAP and ASP do exactly that. For example, the processing type ASP first performs SDI using a single PCA reduction with N components and afterwards performs ADI using a single PCA reduction with N components. (e.g. $ADI(N) \rightarrow SDI(N)$). In theory, combining ADI and SDI with different numbers of PCA components would also be possible (e.g. $ADI(N) \rightarrow SDI(M)$). Different SDI and ADI combinations are discussed in chapters 4.2 and 4.6.

Method and Results

To quantify the difference between single PCA and iterative PCA, the SNR of a subset of Beta Pictoris containing 132 images over an angular range of 37.6° was calculated. All images were first reduced with EsoReflex (Freudling et al. [2013]) before being prepared using Pypeline 1. For iterative PCA, a PCA reduction with 1 principal component is repeated N times. For single PCA, the data is reduced

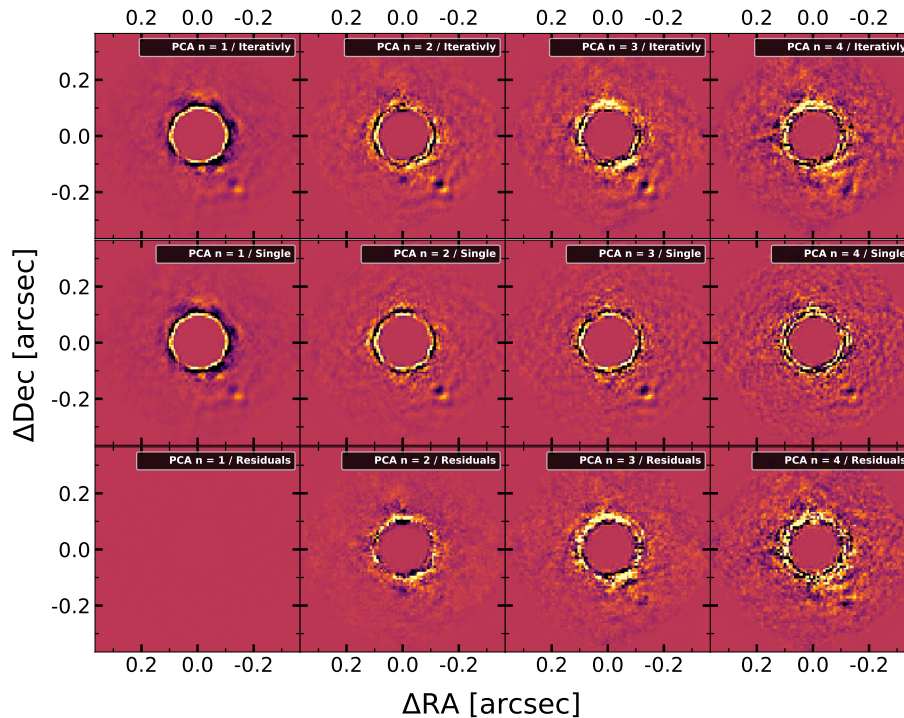


Figure 10: Example of iterative PCA (using n PCA reductions each with 1 principal component) compared to using a single PCA reduction (using 1 PCA reductions each with n principal components). The target is a subset of Beta Pictoris containing 132 images over a angular range of 37.6° . All images were processed using SAP (for further explanation see chapter 2.4) and median averaging was used to create the final images. The residuals were calculated by subtracting the single PCA from iterative PCA. The colour-bar of each image is set arbitrary.

using 1 PCA reduction with N principal components. The PCA reductions were done using Pypeline 3. Additionally, the radial and azimuthal displacements of Beta Pictoris b were calculated using equation 8 and 9.

The results of the SNR comparison between iterative and single PCA reduction for different numbers N can be seen in figure 11 and is equivalent to the principal component number. For the selected dataset of Beta Pictoris the radial displacement is $\Delta r = 0.11$ arcsec and the azimuthal displacement is $\Delta_{rot} = 0.16$ arcsec.

Discussion

The results in figure 11 show a generally low SNR. This was expected, as only a small subset of Beta Pictoris was chosen to minimise the computational intensity. For ADI, iterative PCA and single PCA achieve similarly results. For SDI, the single PCA achieves slightly higher SNRs than iterative PCA. The difference is explained

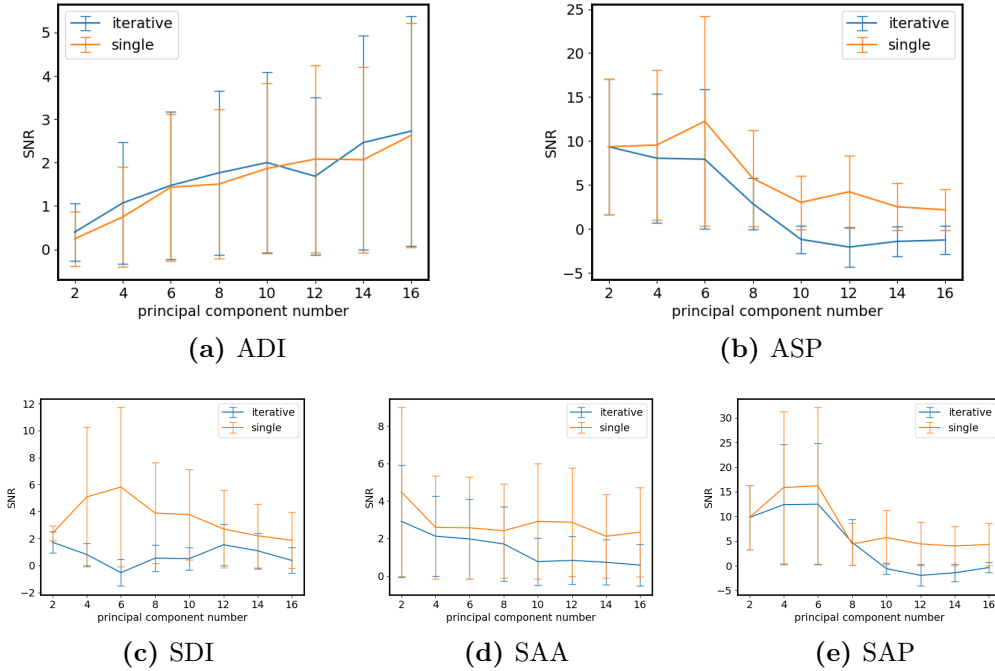


Figure 11: SNR of iterative PCA (using n PCA reductions each with 1 PCA component) compared to using a single PCA reduction (using 1 PCA reduction each with n principal component). The target is Beta Pictoris using subset containing 132 images over an angular range of 37.6° . The differential imaging techniques are explained in chapter 2.4.

as a result of the weak signal which can be influenced by the SDI (or ADI) tail around the exoplanets position.

The differential techniques combining ADI and SDI had similar SNRs for both single and iterative PCA. The slightly higher SNR for single PCA can be explained by the influence of the SDI tail which is a self-subtraction artefact. The stronger self-subtraction in SDI than in ADI is explained with the smaller radial displacement after rescaling (≈ 0.11 arcsec) than the rotational displacements (≈ 0.16 arcsec). Small approximation errors in iterative PCA could increase the self-subtraction of the companion. The influence of self-subtraction is further analysed in chapter 4.3. Additionally, the shape of the curves is discussed in chapter 4.2.

Overall, the results found in this chapter show that switching several times between ADI and SDI is feasible for Beta Pictoris b as the influence of applying PCA iteratively is small. For the course of this thesis it is assumed that the single and iterative PCA can be used interchangeably. To further test this assumption more targets could be analysed. This would be especially insightful as the performance of advanced differential imaging techniques can strongly depend on the observed target.

Because this result shows that every reduction step can be followed by another, many different combinations are possible. The number of possible combinations

goes exponentially with the number of principal components. For N principal components, there exist 2^N possible ADI / SDI combinations. Fortunately, if the target is bright enough that a few principal components suffice for a detection, the number of possible combinations becomes small enough to be tested.

4.2 Advanced Differential Imaging Techniques

ADI efficiently reduces non-rotating noise while SDI efficiently reduces noise which scales with wavelength. Combining both to advanced differential imaging techniques allows the efficient reduction of both confounding factors (see chapter 2.4). In this chapter, advanced differential imaging techniques are compared to ADI on Beta Pictoris, 51 Eridani and HR 8799. The goal is to determine which techniques achieve the highest SNR depending on the target and which achieve the most favourable contrasts.

Method and Results

All data used during this test was first reduced with EsoReflex (Freudling et al. [2013]) before being prepared with Pypeline 1 and 2. The differential imaging techniques were applied using Pypeline 3 with principal component numbers between 0 and 18 before calculating the SNR. To find the detection limit in the datasets, the contrast curve for 5 sigma detection limits were calculated using 4 principal components. The separation range of the contrast curves has a lower limit of 0.15" because of the inner working angle of the coronagraph (Wilby [2018]). The upper limit was set to 0.3" for a reasonable computational intensity. Especially the evaluation time of ADI-SDI combinations was a limiting factor. The selection of smaller subsets and cropping the images to a reasonable size (according to chapter 3.7) allowed to reduce the computation time. On the other hand, this also limited the analysis to a smaller FOV.

For Beta Pictoris a subset containing 132 images over an angular range of 37.6° was selected. The calculated SNRs can be seen in figure 12a. Examples of final images can be seen in the appendix, figure 37. The HR 8799 system consists of 4 known exoplanets but only e is within the full FOV of SPHERE/IFS after cropping the images. The SNR values using different reduction processes on HR 8799 e can be seen in figure 12c. The SNR values using different reduction processes on 51 Eridani b can be seen in figure 12e.

Because SAA and ADI were expected to achieve higher SNRs with principal components larger than 18, they were tested using Pypeline 3 on the Beta Pictoris subset with principal component numbers up to 780 for SAA and 120 for ADI. The result can be seen in figure 13.

To quantify the limitations of the different reduction processes, the contrast curves were calculated. Each reduction process has its highest SNR at a specific number of PCA components but because of computational limitations, only a few PCA components could be selected. The contrast curve for the same subset of the

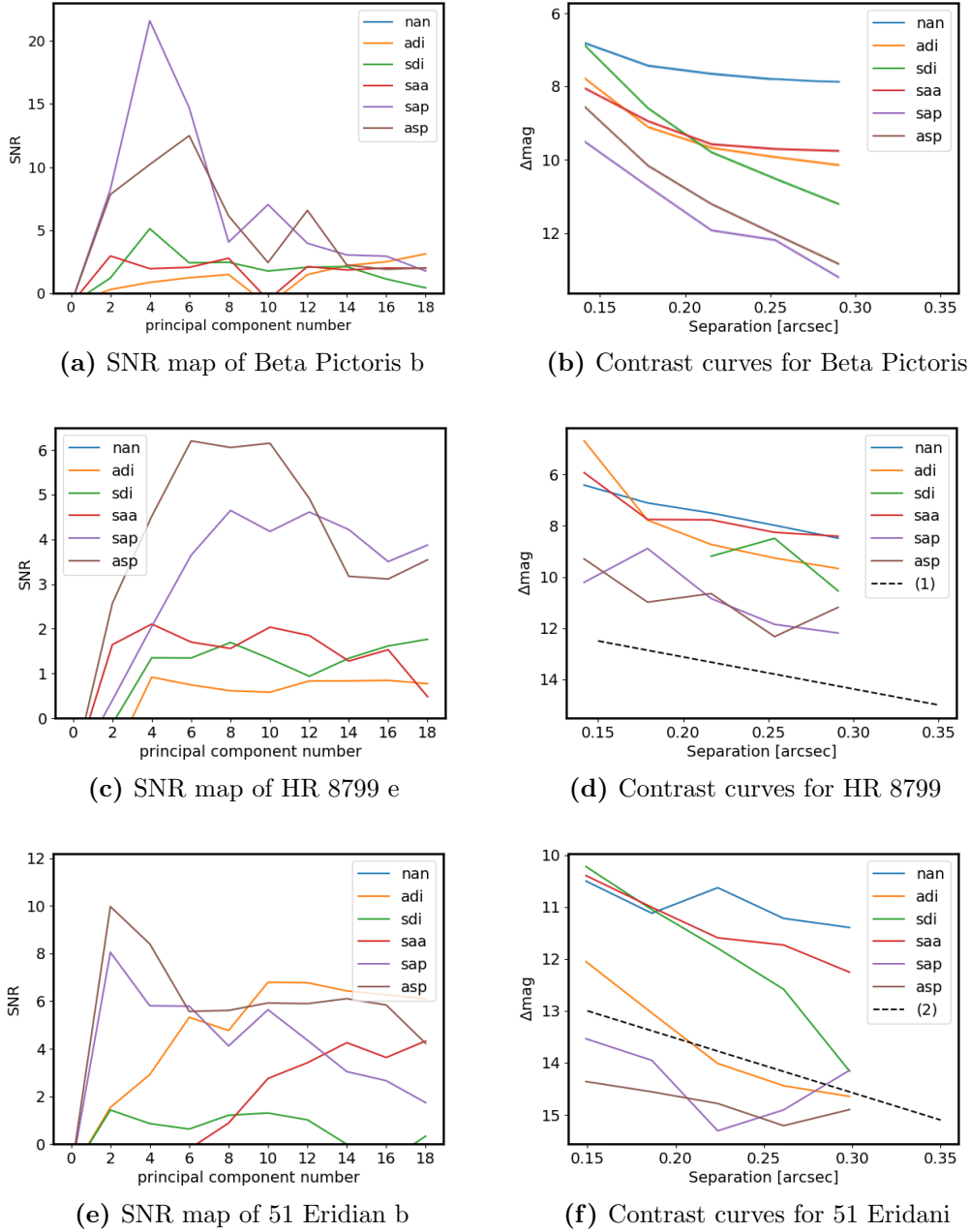
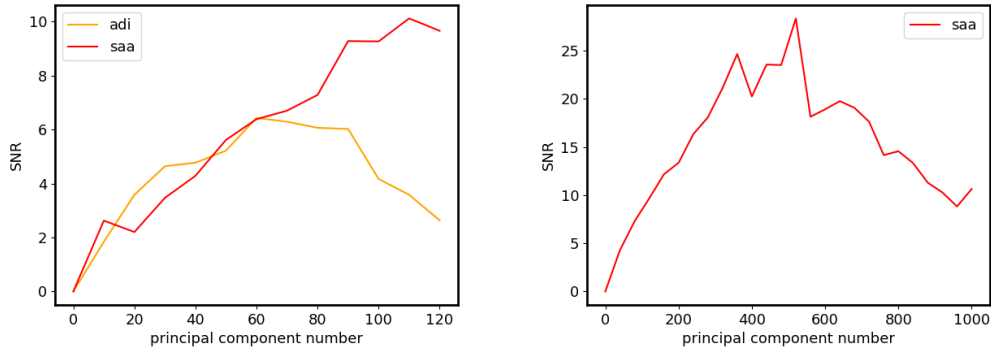


Figure 12: SNRs larger than 0 and contrast curves of the three test targets for different reduction processes (PI: J. Beuzit). For Beta Pictoris a subset of 132 images over a range of 37.6° was used. All contrast curves were calculated using 4 PCA components. The lower separation limit of 0.1 arcsec is given by the inner working angle of the coronagraph. The contrast curves of HR 8799 are compared to an approximation of (1): Zurlo et al. [2016]; the contrast curves of 51 Eridani are compared an approximation to (2): Samland et al. [2017]. The differential imaging techniques are explained in chapter 2.4. NAN was also calculated for all targets but all SNRs were below 0.



(a) ADI for 0 to 120 principal components (b) SAA for 0 to 1000 principal components

Figure 13: SNR using SAA and ADI on a subset of Beta Pictoris b containing 132 images over an angular range of 37.6° . The differential imaging techniques are explained in chapter 2.4.

Beta Pictoris as used for the SNR calculation can be seen in figure 12b. The contrast curves for 51 Eridani and HR 8799 can be seen in figure 12f and 12d, respectively.

Discussion - Detections

For the detection of Beta Pictoris b, the best combination according to figure 12a is SAP using 4 principal components ($\text{ADI}(2) \rightarrow \text{SDI}(2)$). The SNR becomes lower if more principal components are used which can be explained by self-subtraction of the companion (see chapter 4.3). The generally low SNR of ADI for principal component numbers less than 18 can be explained by the short integration time and the strong influence of the speckles. This result shows the advantage of the advanced differential imaging technique especially in speckle limited cases. The integration time after which Beta Pictoris b is speckle limited is determined in chapter 4.5.

The result for 51 Eridani b in figure 12e shows the highest SNR for ASP using 2 principal components ($\text{ADI}(1) \rightarrow \text{SDI}(1)$). Similar to Beta Pictoris b, the drop in SNR of SAP and ASP with increasing principal components is explained by self-subtraction. Unlike Beta Pictoris b, ADI can achieve a 7 sigma detection of 51 Eridani b using 10 principal components. This was expected, as the larger separation ($\approx 0.45''$) reduces the influence of speckles. Overall, the results show that SAP and ASP achieve higher SNRs than using only ADI.

HR 8799 e is at a slightly shorter separation (0.38 arcsec) from its host star than 51 Eridani b (0.45 arcsec) but is also considerably fainter (≈ 2 mag). The result in figure 12c shows that the maximum SNR is achieved using ASP with 6 principal components. With HR 8799 e, ADI does not achieve a detection over 2 sigma which was expected because of the strong speckle influence. Therefore, the advanced differential imaging techniques allowed to detect an exoplanet which was not detectable with ADI alone.

As mentioned in chapter 2.4, SAA uses only one PCA reduction where, on the other hand, SDI and ADI use several (the exact number depends on the dataset).

Therefore, it was expected, that SAA has a lower SNR than other advanced differential imaging techniques at low numbers of principal components. Comparing the results of Beta Pictoris b from figure 13b with the ones from figure 12a shows that after using a sufficient number of principal components (≈ 400), the SNRs of SAA are higher than SAP. A similar analysis was conducted for ADI and the results can be seen in figure 13a. Its highest SNR was found for roughly 60 principal components. As expected, this is still lower than all other SDI/ADI combinations. Unfortunately, because of computational limitations, a comparison between the advanced differential imaging techniques using more than 18 principal components was not feasible for 51 Eridani b and HR 8799 e.

Overall, the newly implemented advanced differential imaging techniques achieve higher detection limits and have clearer detections for the three selected targets. The faint and close in HR 8799 e profited the most from adding SDI to ADI as it was not detectable using only ADI. Nevertheless, only three targets were tested and the results differed for all of them. To make a general statement about the advanced differential imaging techniques, more targets need to be analysed.

Discussion - Contrast Limits

The detection limits of the advanced differential imaging techniques applied to the Beta Pictoris dataset can be seen in the contrast curves of figure 12b. SAP and ASP achieve the highest contrasts. Compared to ADI, they can detect fainter exoplanets especially at larger separations. Because only a subset of Beta Pictoris was chosen, its contrast curves were expected to be less favourable than HR 8799 or 51 Eridani and no further conclusions were drawn from this contrast curve.

The contrast curves for HR 8799 in figure 12d show the most favourable contrasts for SAP and ASP. They improve the contrast of ADI by roughly 2 magnitudes for all tested separations. SAA and SDI performed similar to ADI and no significant difference between these three was found. [Zurlo et al. \[2016\]](#) also analysed 51 Eridani and their results can be compared to the ones found in this chapter. They used different datasets than this thesis with a total integration time of ≈ 1.7 h. Their reduction resulted in a contrast of 11 to 15 Δ mag in the innermost $0.35''$. To avoid self-subtraction, they selected the reduction frames for each image according to the exoplanets position to minimise PSF overlap. Compared to the results found by the tested advanced differential imaging techniques, they achieved contrasts roughly 2 magnitudes more favourable which is explained by less self-subtraction due to their selective reduction frames.

Similar to Beta Pictoris and HR 8799, the most favourable contrasts of 51 Eridani in figure 12d are achieved with SAP and ASP. Compared to ADI, they improve the contrast by roughly 1 magnitude for separations smaller than 0.25 arcsec. At larger separations, now clear difference between ADI, SAP and ASP can be seen. The result of 51 Eridani can be compared to the contrasts calculated by [Samland et al. \[2017\]](#). They used different datasets with a total integration time of ≈ 4.5 h. Their reduction resulted in a contrast of 11 to 15 Δ mag in the innermost $0.35''$. Similar to this thesis, they used a combination of ADI and SDI. They first performed ADI on wavelength channels in which no planetary flux is expected because

of methane and water absorption. Then they only used those channels for SDI before reducing the whole cube with ADI. In their case, using selective reference frames did not achieve better results than found with the tested advanced differential imaging techniques. Especially at short separations, SAP and ASP can detect exoplanets over 1 magnitude fainter than they could.

Overall, the advanced differential imaging techniques SAP and ASP achieved better contrast curves than ADI in all three targets. No clear separation dependence of their performance could be found as neither SAP nor ASP could significantly outperform the other. Furthermore, [Samland et al. \[2017\]](#) and [Zurlo et al. \[2016\]](#) carefully selected their reduction frames for each image and hence later achieved more favourable contrasts in HR 8799 than found in this chapter. As the newly implemented SDI now allows to efficiently analyse SPHERE/IFS data, those selective reduction frame techniques could be combined with the implemented advanced differential imaging techniques to further improve the contrast limits.

4.3 Companion Brightness

PCA reduces the stellar PSF and helps to detect faint companions. Because of the companion's azimuthal and radial (after wavelength rescaling) shift during the observation, its signal is smeared out and thus should not be reduced by the PCA. Unfortunately, the PSF of a bright companion can have considerable overlap and thus it could also be partially removed. This effect is called self-subtraction. The same can happen to faint companions in higher order principal components. In this chapter the SNR dependence on the target's brightness is tested.

Method and Results

To analyse the influence of a companion's brightness on the final SNR, a subset of the Beta Pictoris dataset containing 132 images over an angular range of 37.6° was selected. All data used during this test was first reduced with EsoReflex ([Freudling et al. \[2013\]](#)) before being prepared with Pypeline 1. Afterwards fake planets with a given magnitude were injected at $SEP = 0.25$ arcsec and $PA = 0^\circ$ using the FakePlanetModule of PynPoint. The fake planet and Beta Pictoris b have a rotational offset of approximately 135° to prevent interference. Afterwards, the prepared images were processed using Pypeline 3 with 4 and 10 principal components. The results can be seen in figure 14. Additionally, the rotational and radial displacements of the dataset were calculated with equations 8 and 9 and were found to be $\Delta r = 0.11$ arcsec and $\Delta rot = 16$ arcsec.

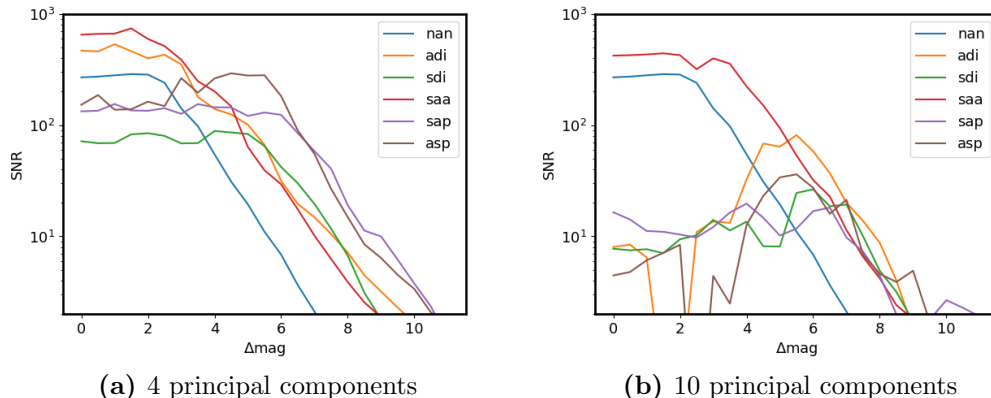


Figure 14: SNR for injected fake companions with different magnitudes. The dataset used for the injection is a subset of Beta Pictoris containing 132 images over the angular range 37.6° (PI: J. Beuzit). The fake companion was injected at $SEP = 0.25$ arcsec and $PA = 0^\circ$. Only SNR values larger than 2 are displayed. The differential imaging techniques are explained in chapter 2.4

Discussion

Generally, fainter companions have a lower SNR as their signal is weaker. In figure 14a, this trend can be seen in all differential imaging techniques. For faint companions ($\Delta\text{mag} < 6$), SAP and ASP achieve the highest SNR which agrees with the contrast curves in chapter 4.2. Those techniques can be used to detect companions approximately 1 magnitude fainter than with ADI. In figure 14a, the SNR for bright targets ($\Delta\text{mag} > 4$) stagnates at a constant value for all differential imaging techniques. Because NAN is also affected, this test shows that not only PCA can cause self-subtraction. Furthermore, it shows that for small reductions (less than 5 principal components or classical ADI) the self-subtraction exactly cancels the signal gain of bright companions.

Comparing the results from figure 14a and figure 14b shows an increasing importance of self-subtraction with higher principal component number. For 10 principal components (see figure 14b), self-subtraction is dominant up to $\Delta\text{mag} = 6$. Therefore, the tests indicate that SAP, ASP, ADI or SDI might result in lower SNRs for targets with $\Delta\text{mag} < 6$ than only derotating and stacking would achieve. For companions with $\Delta\text{mag} < 4$, ADI and SAA achieve better results than SAP and ASP. Especially SAA only shows minimal self-subtraction, which was expected for this method as 4 and 10 principal components only slightly reduces the images.

Self-subtraction is caused by PSF overlap. Because the PSF overlap not only depends on the brightness of the companion but also on the azimuthal displacements Δrot and radial displacements Δr (see chapter 4.4), the lower Δmag limits for the differential imaging techniques cannot be derived from companion brightness alone. In figure 14, the self-subtraction of SDI is stronger than of ADI. Both use displacements in a single direction but the radial displacements are smaller ($\Delta r =$

0.11 arcsec) than the angular displacement ($\Delta rot = 0.16$ arcsec). This explains the lower SNR of SDI as smaller displacements cause higher self-subtraction (see chapter 4.4).

As discussed in chapter 4.4, rotation and separation of a dataset strongly affect self-subtraction. The injection was only done for one separation of 0.25 arcsec. Further tests for different separations would help to analyse the combined dependence of separation and target brightness.

4.4 Rotation and Wavelength Range

An important aspect of ADI is the total azimuthal rotation $\Delta\alpha$ during the observation. Insufficient field rotation (and therefore small rotational displacements Δrot) lead to PSF overlap and this, in turn, would lead to a lower SNR because of the companion's self-subtraction. SDI on the other hand, does not use azimuthal displacements, and thus does not depend on $\Delta\alpha$. However, it does depend on the total radial displacement Δr which is caused by the rescaling according to the wavelength range $\Delta\lambda$ of the observations. Analogous to the rotation, the larger the wavelength range, the lower the PSF overlap. In this chapter the performances of the advanced differential imaging techniques are analysed under different total rotations $\Delta\alpha$ and different wavelength ranges $\Delta\lambda$.

Method and Results

For the rotation test, the dataset of Beta Pictoris was split into subsets. Each subset contained 20 images with different total rotations. This sample size was chosen to allow a reasonable rotational resolution. The images of each subset were chosen evenly spaced over their total rotation (e.g: the subset corresponding to 10° contained the images with the companion at approximate azimuthal positions of $\{0^\circ, 0.5^\circ, 1^\circ, \dots, 9^\circ, 9.5^\circ\}$). The dataset of Beta Pictoris therefore allowed to scan rotation angles from 0.97° up to 37.4° . All subsets were reduced with EsoReflex (Freudling et al. [2013]) before being prepared with Pypeline 1. Afterwards, they were processed using the advanced differential imaging techniques applied with Pypeline 3. The SNR dependence on the total rotation $\Delta\alpha$ can be seen in figure 15.

To test the SNR's dependence on wavelength range, a subset of the Beta Pictoris dataset containing 132 images over an angular range of 37.6° was chosen and reduced with EsoReflex. This subset was used to create five new subsets each containing seven wavelength frames taken from each of the 132 images¹⁹. The wavelength difference $\Delta\lambda$ within the subsets is: $0.07\mu\text{m}$, $0.14\mu\text{m}$, $0.22\mu\text{m}$, $0.29\mu\text{m}$ and $0.36\mu\text{m}$. All subsets were prepared using Pypeline 1. Afterwards, they were processed using the advanced differential imaging techniques applied with Pypeline 3. The SNR dependence on the total wavelength range $\Delta\lambda$ can be seen in figure 16.

For comparable results, the displacements are also given in FWHM of Beta Pictoris. The average FWHM was calculated using the flux images of Beta Pictoris

¹⁹After being processed with EsoReflex each image contains 39 wavelength frames.

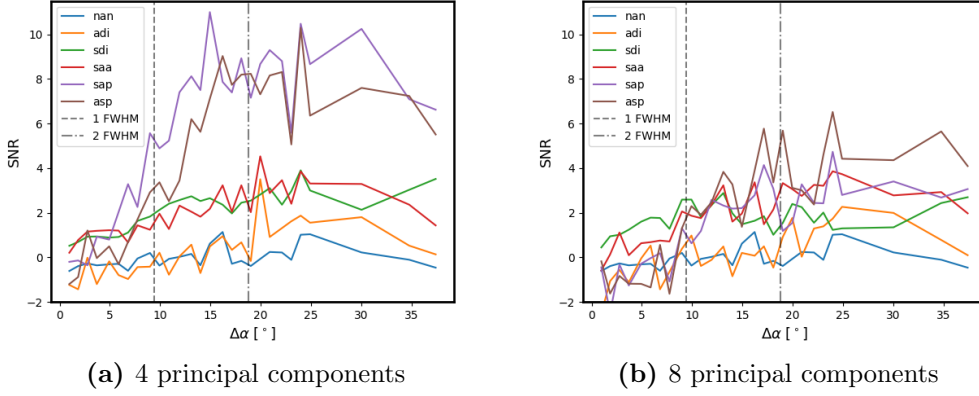


Figure 15: SNR for different total rotation angles $\Delta\alpha$. The test target is Beta Pictoris (PI: J. Beuzit) using subsets containing 20 images with different total rotations. All images of the subsets are evenly spaced over their total rotation. The FWHM was calculated using the flux images of Beta Pictoris at $\lambda = 1.16\mu\text{m}$. At the separation of Beta Pictoris b (0.25 arcsec), a rotation of 9.40° causes a 1 FWHM displacement. The differential imaging techniques are explained in chapter 2.4.

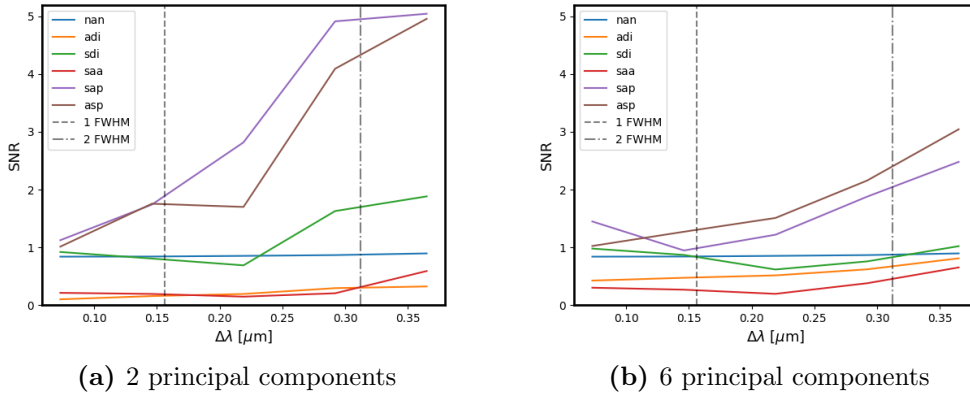


Figure 16: SNR for different total wavelength ranges $\Delta\lambda$. The test target is Beta Pictoris using a subset of 132 images over a wavelength range of 37.6° (PI: J. Beuzit). To scan different wavelength ranges, these subsets are further divided into sets containing 7 frames from each of the 132 images. All frames of the subsets are evenly spaced over their total wavelength range. The FWHM was calculated using the flux images of Beta Pictoris at $\lambda = 1.16\mu\text{m}$. The wavelength range of the Beta Pictoris dataset is $0.95 - 1.35\mu\text{m}$ and therefore a wavelength difference of $0.158\mu\text{m}$ causes a 1 FWHM displacement. The differential imaging techniques are explained in chapter 2.4.

at $\lambda = 1.16\mu\text{m}$ and 1 FWHM was found to be 0.041 arcsec. Using equations 8, 9 and setting $\Delta r = \Delta rot = \text{FWHM}$, the rotation and wavelength ranges equivalent to a displacement of 1 FWHM are: $\Delta\alpha_{FWHM} = 9.40^\circ$ and $\Delta\lambda_{FWHM} = 0.156\mu\text{m}$.

Discussion

The reduction processes SAP and ASP show a linear SNR increase for small $\Delta\alpha$. After a certain $\Delta\alpha$, the PSF overlap is no longer dominant, and thus at larger $\Delta\alpha$ the SNR does not increase significantly. Using SAP or ASP with 4 principal components, this happens at $\Delta\alpha \approx 15^\circ$ (equivalent to ≈ 1.6 FWHM). Because of self-subtraction the SNR gets significantly lower for SAP and ASP using 8 principal components. Nevertheless, a small increase in SNR up to approximately 4 sigma can be seen for SAP, ASP and SAA. The SNR values for ADI and SDI are generally below 2 and thus dominated by noise and processing artefacts. Their low SNR can be explained by the short integration time and the low number of principal components selected for which Beta Pictoris b was not visible in chapter 4.2 using these techniques.

In the results of the wavelength test in figure 16, the reduction processes SAP and ASP increase approximately linearly with $\Delta\lambda$. Similar to the wavelength range, the increase is weaker if more principal components are used which can again be explained by the companion's self-subtraction. Because of the low resolution of SPHERE/IFS, only wavelength ranges between $0.07\mu\text{m}$ and $0.36\mu\text{m}$ could be analysed. An additional effect which must be considered in this test is the varying brightness of Beta Pictoris b depending on wavelength. For the wavelength range $0.95 - 1.35\mu\text{m}$ of this dataset, the measurements of Chilcote et al. [2017] show an approximately linear increase in brightness for longer wavelengths. Averaging their results over the same $\Delta\lambda$ as the subsets shows, that the averaged signal of Beta Pictoris b no more than doubles from $\Delta\lambda = 0.07\mu\text{m}$ to $\Delta\lambda = 0.36\mu\text{m}$. Therefore, the higher SNR for larger $\Delta\lambda$ in figure 16a cannot only be caused by the increasing brightness of Beta Pictoris b but also by reduced self-subtraction due to larger Δr .

The results for the tests on $\Delta\alpha$ and $\Delta\lambda$ both show increased SNRs for larger ranges. Therefore, to optimise the advanced differential imaging techniques, the SPHERE/IFS wavelength range of $0.95 - 1.68\mu\text{m}$ should be used. Additionally, the dataset should have a total rotation resulting in an azimuthal displacement of at least 1.6 FWHM. The exact rotation value depends on the target, because companions at smaller separations need a larger total rotation.

To reduce the self-subtraction even in cases with only small displacements, datacube libraries can be used where the reduction frames are selected individually for each image. As mentioned in chapter 4.2, Pueyo et al. [2015] and Zurlo et al. [2016] used them on HR 8799 to achieve better detection limits. They created the datacube library by skipping all wavelength frames where the PSF overlap was larger than a given threshold therefore reducing self-subtraction. Adding selection criteria for reduction frames into the PynPoint modules could help to achieve higher SNRs.

4.5 Integration Time

In this chapter, the SNR dependence on total integration time is analysed. As the FOV of SPHERE/IFS is small, its images are mostly limited by the residual noise of the star (e.g. speckles). Therefore, a longer integration time might not result in a higher SNR. The goal of this test is to determine in which cases a longer integration time can improve detections and if the advanced differential imaging techniques help to reduce the speckle's influence. This is especially important as telescope time is rare and expensive.

Method and Results

The dataset of Beta Pictoris was used as a test target as its short detector integration time of 4 seconds per image allows for a detailed analysis. All images were reduced with EsoReflex (Freudling et al. [2013]) before being prepared with Pipeline 1. Afterwards, several subsets with different integration times were created. Each subset contains subsequent images with a total integration time of Δt (e.g. subset $_{\Delta t=80} = \{\text{image 1, image 2, image 3, \dots, image 19, image 20}\}$ and subset $_{\Delta t=240} = \{\text{image 1, image 2, image 3, \dots, image 59, image 60}\}$). Therefore, the rotational difference between subsequent images is the same for all datasets but the total rotation $\Delta\alpha$ increases with integration time. Each subset was then processed according to Pipeline 3 before calculating the SNR of Beta Pictoris b. The results can be seen in figure 17.

To compare the results with the SNR increase of the photon noise limited case, a slope proportional to \sqrt{t} is plotted. If the noise is only due to short integration time, the SNR is expected to follow this curve.

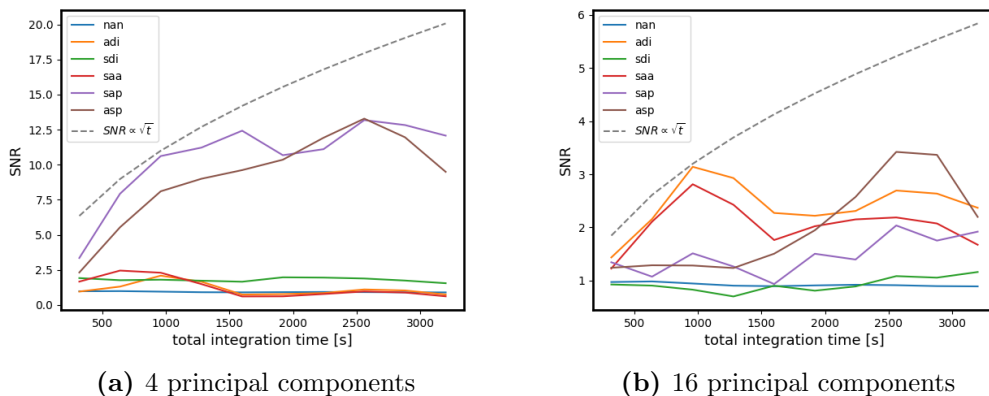


Figure 17: SNR dependence on integration time. The test target is Beta Pictoris b (PI: J. Beuzit). A curve proportional to \sqrt{t} is shown to compare the SNR increase of the observation to the photon noise limited case. The differential imaging techniques are explained in chapter 2.4.

Discussion

In figure 17a, the SNR of SAP and ASP roughly follows the photon noise curve for $\Delta t < 1500$ s. This was expected, as short integration times lead to photon noise limited observations. Afterwards, no clear increase with integration time can be seen. This stagnation is presumably because of the stellar speckles which limits the detection. In comparison, ADI in figure 17b never shows more than a 2.5 sigma detection and only follows the photon noise curve up to $\Delta t < 1000$ s. As mentioned in chapter 2.4, SAP and ASP should help to reduce the speckle noise. The results confirm this as SAP and ASP scale better with integration time than ADI.

Overall, using integration times over 1500 seconds (roughly 30 minutes) does not increase the SNR significantly. This result is also influenced by the selection of the subset. Because the images were chosen subsequently and not spread out as in other tests, they have a larger PSF overlap and therefore are more likely to be affected by self-subtraction. Additionally in figure 17b, self-subtraction effects could be an explanation of the increasing SNR for ASP after 1500 seconds because $\Delta\alpha$ increases with Δt (see chapter 4.4). In all other tests, SAP and ASP were self-subtraction dominated if more than 10 principal components were used.

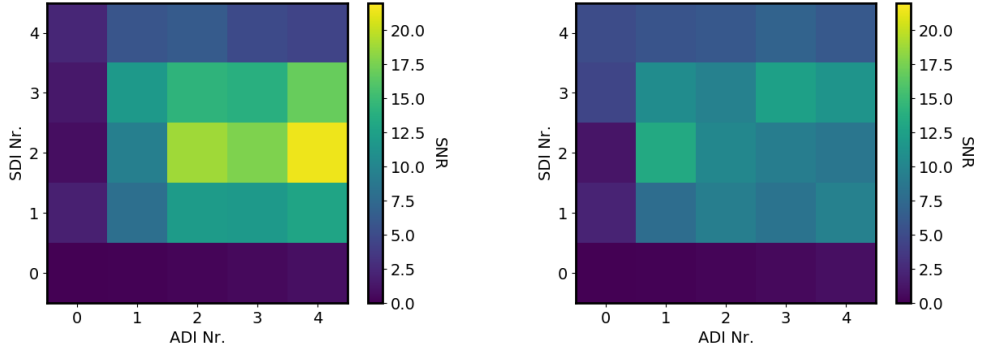
Janson et al. [2007] analysed the integration time dependence of ADI and SDI combinations for ϵ Eridani. In contrast to this chapter's test, they used three narrow band filters for SDI (1.575 μm , 1.600 μm and 1.625 μm). Additionally, they only choose two time instances for the ADI reduction. Similar to the results in figure 17a they found that the errors first increased according to the photon noise curve before slightly deviating. Overall, the results from this thesis are in agreement with their results.

4.6 Further ADI/SDI Combinations

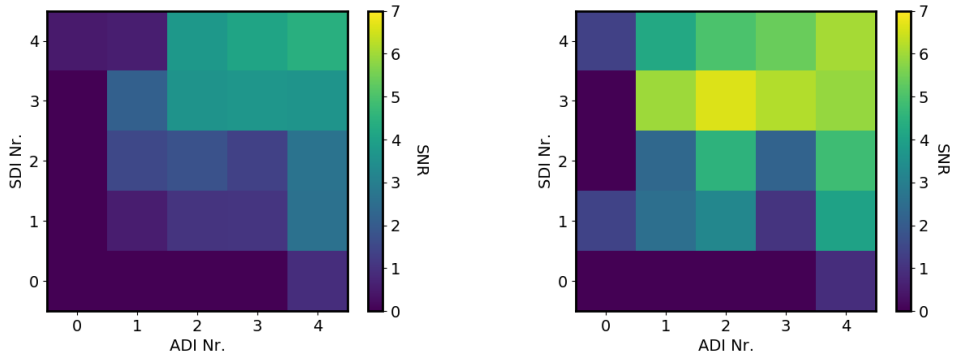
As described in chapter 2.4, many different combinations of ADI and SDI are possible. All previous tests used SAP or ASP which performed ADI and SDI one after the other with the same number of principal components (e.g. SAP with 4 principal components is: SDI(2) \rightarrow ADI(2)). A priori it is not clear whether using SDI and ADI with an equal number of principal components results in the highest SNR. Additionally, the best reduction for one target is not necessarily the best for all. In this chapter, SAP and ASP with different ADI and SDI strengths were analysed (e.g. SDI(M) \rightarrow ADI(N) and ADI(N) \rightarrow SDI(M)).

Method and Results

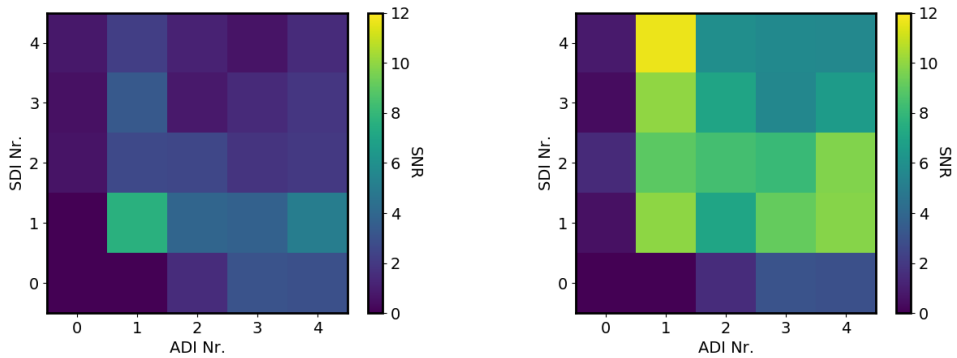
To test further ADI and SDI combination, a subset of the Beta Pictoris dataset containing 132 images over an angular range of 37.6° was analysed. All images were reduced with EsoReflex (Freudling et al. [2013]) before being prepared with Pipeline 1. Afterwards, Pipeline 3 was used twice to first apply ADI with N principal components and then used again to apply SDI with a number of M principal components. The same was done using first SDI than ADI. The maximum number of



(a) Beta Pictoris b using first SDI then ADI (b) Beta Pictoris b using first ADI then SDI



(c) HR 8799 e using first SDI then ADI (d) HR 8799 e using first ADI then SDI



(e) 51 Eridani b using first SDI then ADI (f) 51 Eridani b using first ADI then SDI

Figure 18: SNR maps of three test targets (PI: J. Beuzit) processed with the differential techniques $\text{SDI}(M) \rightarrow \text{ADI}(N)$ and $\text{ADI}(N) \rightarrow \text{SDI}(M)$ on a grid of 0 to 4 principal components. For Beta Pictoris a subset of 132 images over an angular range of 37.6° was chosen. For 51 Eridani and HR 8799, the full dataset was used.

principal components per reduction step was limited to 4 ($0 \leq N \leq 4, 0 \leq M \leq 4$). This principal component range was chosen based on the first analysis of SAP and ASP in chapter 4.2 where the best reduction was within this range and because of computational limitations. The SNR values for $\text{SDI}(M) \rightarrow \text{ADI}(N)$ and $\text{ADI}(N) \rightarrow \text{SDI}(M)$ can be seen in figures 18a and 18b, respectively.

The same analysis was conducted for 51 Eridani b and the SNR values for $\text{SDI}(M) \rightarrow \text{ADI}(N)$ and $\text{ADI}(N) \rightarrow \text{SDI}(M)$ can be seen in figures 18e and 18f, respectively. Lastly, HR 8799 e was analysed and its SNR values for $\text{SDI}(M) \rightarrow \text{ADI}(N)$ and $\text{ADI}(N) \rightarrow \text{SDI}(M)$ can be seen in figures 18c and 18d, respectively.

Discussion

The SNR maps for Beta Pictoris b in figures 18a and 18b show the highest SNR for using $\text{ADI}(4) \rightarrow \text{SDI}(2)$. Therefore confirming, that the best reduction technique not necessarily requires $M = N$. As the number of principal components was capped at 4, using more principal components in the ADI step of SAP might result in a higher SNR. A similarity between the results in this chapter and the ones from chapter 4.2 is a strong decrease in SNR if more than 2 principal components in SDI are used. This effect is explained by self-subtraction.

The results in figure 18e and 18f for 51 Eridani b show a maximum SNR for $\text{ADI}(1) \rightarrow \text{SDI}(4)$. In both SAP and ASP no clear trend with number of principal components in ADI and SDI can be seen. Therefore, it is possible that the best combination has not been found yet. As 51 Eridani b is at a separation of 0.45 arcsec it is less influenced by speckles than the other targets. Thus, it was expected that only a small number of principal components in SDI would suffice but the results show that the best technique uses the highest number of all three test targets. A possible explanation for this result is that the small radial shifts close to the host star (see equation 8) cause interpolation effects which limit the quality of the SDI reduction. At larger separations, the PSF is shifted more and therefore can be better modelled by the PCA. Another explanation would be the waffle spots which are present in all images of 51 Eridani, Beta Pictoris and HR 8799. Creating the waffle spots also leads to additional residual star light at separations larger than 0.45 arcsec. On the other hand, because no remnants of this pattern can be found in the processed images (e.g. appendix A, figure 39), the influence of the waffle spots is considered neglectable.

In agreement with chapter 4.2, HR 8799 e does not have its maximum SNR at the minimum number of principal components. The highest SNR is achieved using $\text{ADI}(2) \rightarrow \text{SDI}(3)$ and therefore the best differential imaging technique is not limited by the boundaries of M or N . On the other hand, the best reduction technique could be a local maximum and therefore, it is still possible that a reduction technique outside of the tested parameter space achieves a higher SNR. Similar to 51 Eridani b, the higher number of principal components in SDI compared to Beta Pictoris is explained by a better reduction of the stellar PSF at larger separations.

Not using ADI ($\text{SDI}(m) \rightarrow \text{ADI}(0)$ or $\text{ADI}(0) \rightarrow \text{SDI}(p)$) is equivalent to SDI and this technique achieves significantly lower SNRs in all three targets. The same holds true if no SDI is used (equivalent to ADI). Therefore, the results in figure 18 confirm

that combining SDI and ADI achieves higher SNRs at low principal component numbers. As ADI generally achieves better results at principal component numbers above 10 (see chapter 4.2), it is expected that the SNR increases for ADI(>10). On the other hand, ADI did not achieve higher SNRs than SAP or ASP in chapter 4.2 and therefore it is not expected that it outperforms them if more principal components are used. Because of computational limitations, it was not possible to explore a larger parameter space.

Overall, the results show that for each target another differential imaging technique achieves the highest SNR. If observations are searched for new companions it is therefore best to use all advanced differential imaging techniques. Using these techniques with $M \neq N$ increases the chance of finding new companions but also increases the computational time considerably.

4.7 STIM Detection Map

The detection maps of all tests were created by averaging over the whole dataset using the median. This has the advantage that photometry is still possible on the final image, but it might not be the best way to create a detection map. During this thesis, the STIM module proposed by [Pairet et al. \[2019\]](#) was implemented (see section 3.5). In this chapter the STIM module is tested and compared to median averaging.

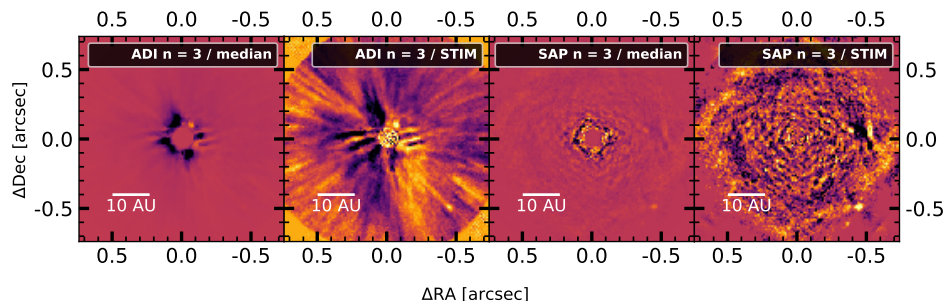
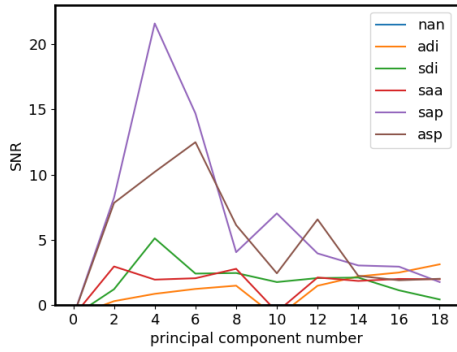


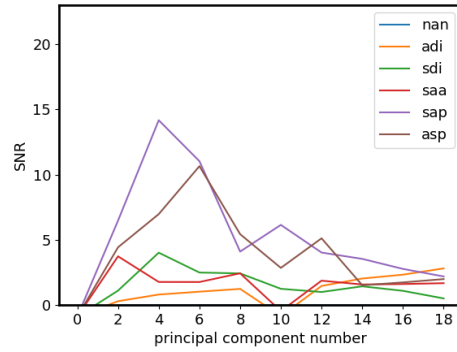
Figure 19: Example of detection maps using median averaging and the STIM map proposed by [Pairet et al. \[2019\]](#). The target is Beta Pictoris using a subset of 132 images over an angular range of 37.6° (PI: J. Beuzit). The colour-bar of each image is set arbitrary and brighter colours represent higher values.

Method and Results

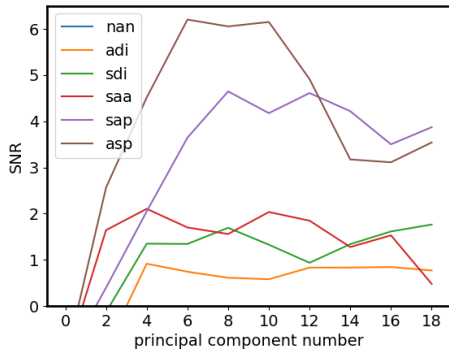
To analyse the STIM module, the tests of chapter 4.2 were repeated using the same datasets. This includes reducing them with EsoReflex ([Freudling et al. \[2013\]](#)) before preparing them with Pypeline 1. Afterwards, Pypeline 3 is applied but instead of averaging to get the final image, the STIM map was produced. These maps were



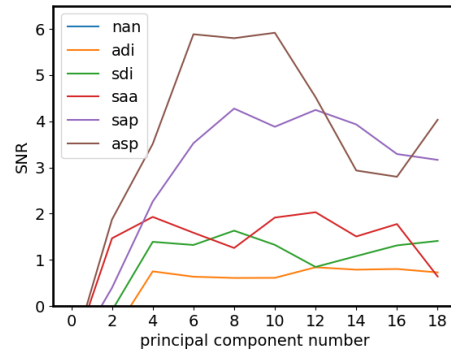
(a) SNR map of Beta Pictoris b using median averaging



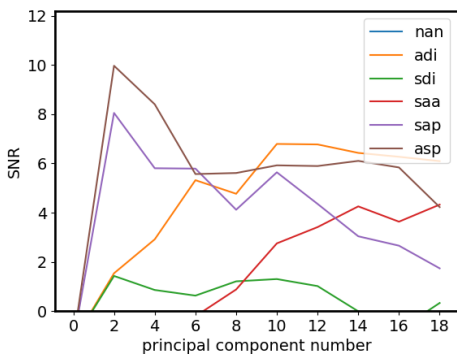
(b) SNR map of Beta Pictoris b using the STIM detection map



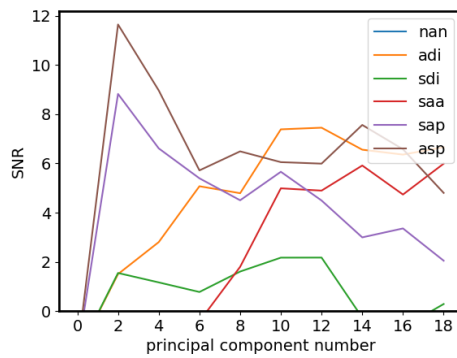
(c) SNR map of HR 8799 e using median averaging



(d) SNR map of HR 8799 e using the STIM detection map



(e) SNR map of 51 Eridani b using median averaging



(f) SNR map of 51 Eridani b using the STIM detection map

Figure 20: SNR detections larger than 0 of three different targets (PI: J. Beuzit) using the STIM module. For comparison the results of chapter 4.2 are displayed. For Beta Pictoris a subset of 132 images over an angular range of 37.6° was chosen. For 51 Eridani and HR 8799, the full dataset was used. The differential imaging techniques are explained in chapter 2.4. NAN was also calculated for all targets but all SNRs were below 0.

calculated using the implementation in PynPoint as described in chapter 3.5. The resulting SNR of the STIM maps for Beta Pictoris, HR 8799 and 51 Eridani can be seen in figures 20b, 20f and 20d, respectively. For comparison, the targets results from chapter 4.2 are displayed in figures 20a, 20e and 20c, respectively.

A visual comparison between a median and a STIM detection map can be seen in figure 19. The target shown is a subset of the Beta Pictoris dataset containing 132 images over an angular range of 37.6° .

Discussion

The change in SNR from the median averaged image to the STIM map is different for all three targets: 51 Eridani b shows a slightly higher SNR compared to median averaging, HR 8799 e does not show significant differences and Beta Pictoris b has a significantly lower SNR. [Pairet et al. \[2019\]](#) claim that their detection map could improve the detection of exoplanets. The results of this thesis only confirm this in one of three cases. Similar to the advanced differential imaging technique, the best detection map can strongly depend on the dataset. The STIM detection map could result in better detections for some targets but as no significant improvement could be found in this chapter, the STIM module was not further used during this thesis.

Background Star Rejection

In chapter 2.5, two classification criteria currently in use are described which can be used to determine if an observed companion candidate is bound or background. The first method uses co-movement measurements for which two observations at least several months apart are necessary. Because a second observation is not always accessible, this method is not suitable for all targets. The second method uses molecular absorption lines to characterise a companion candidate. Unfortunately, the resolution of SPHERE/IFS is not high enough to characterise an object purely on absorption lines. To resolve this problem the model based rejection was developed which allows to identify background sources with a single, low resolution measurement.

The model based rejection is explained in chapter 5.1. To derive a distance estimation to companion candidates, the temperature-radius relation for brown dwarfs is derived in chapter 5.2. Additionally, rejection methods which were investigated during this thesis but did not perform better than the model based rejection are presented in chapter 5.3. Lastly, the model based rejection was tested on 51 Eridani b and the results can be seen in chapter 5.4.

5.1 Model Based Rejection

The model based rejection was developed to classify a companion candidate as bound or background source with a single, low resolution measurement. It compares the observed spectrum (for example from SPHERE/IFS) of a companion candidate with exoplanet atmosphere models to derive its basic characteristics (T_{eff} , $\log g$, metallicity and distance). This information is then used to classify the companion candidate.

First, an exoplanet atmosphere model grid is set up. As the companion candidate can be a planet or a star, a model²⁰ $F_{\text{model}}(T_{\text{eff}}, \log g, \text{FeH})$ with the parameters of both object types is required. For this thesis, the Bt-Settl model was chosen ([Allard](#)

²⁰It would also be possible to combine several models for a more detailed search over a larger parameter space.

[2013]) with a resolution of $\Delta T = 200\text{K}$, $\Delta \log g = 0.5$ and $\Delta \text{FeH} \approx 0.5$ over the range of $T_{\text{eff}} = [2000\text{K}, 9800\text{K}]$, $\log g = [2.0, 5.0]$ and $\text{FeH} = [-2.0, 0.0]$.

The models $F_{\text{model}}(T_{\text{eff}}, \log g, \text{FeH})$ do not yet account for the distance to or the size of the companion candidate. The flux increases linearly with the surface of the object (for a sphere: $F \propto A = 4\pi R_{\text{obj}}^2$) and decreases quadratically with the distance ($F \propto \frac{1}{4\pi D^2}$). The flux $F_{MD}(T_{\text{eff}}, \log g, \text{FeH}, R_{\text{obj}}, D)$ at a distance D can therefore be written as:

$$F_{MD}(T_{\text{eff}}, \log g, \text{FeH}, R_{\text{obj}}, D) = \frac{4\pi R_{\text{obj}}^2}{4\pi D^2} F_{\text{model}}(T_{\text{eff}}, \log g, \text{FeH}) \quad (12)$$

The object radius R_{obj} cannot be directly measured with direct imaging and hence must be deduced from measurable quantities. Therefore, in chapter 5.2 the results of [Stassun et al. \[2012\]](#) were used to derive a linear $T_{\text{eff}} - R$ relation for objects with temperatures between 3300 - 4200K:

$$R_{\text{obj}} = B_0 T_{\text{eff}} + Q_0 = (2.9 \times 10^{-3} \frac{R_{\text{jup}}}{K}) T_{\text{eff}} - 5.5 R_{\text{jup}} \quad (13)$$

With the parameters $B_0 = 2.9 \times 10^{-3} R_{\text{jup}}/K$ and $Q_0 = -5.5 R_{\text{jup}}$. Comparing objects with temperature below 3300K to the linear approximation showed that this approximation is valid down to 2200K (see chapter 5.2). Combining equation 12 and 13 results in the relation:

$$F_{MD}(T_{\text{eff}}, \log g, \text{FeH}, D) = \left(\frac{B_0 T_{\text{eff}} + Q_0}{D} \right)^2 F_{\text{model}}(T_{\text{eff}}, \log g, \text{FeH}) \quad (14)$$

In theory other effects which are not yet considered in the above formula could influence the spectrum. Two possible effects are reddening caused by circumstellar dust (especially as direct imaging usually targets young stars) and interstellar reddening. For this thesis interstellar reddening is neglectable because the interstellar medium around the sun is relatively transparent ($E_{B-V} < 0.03$, [Whittet \[2002\]](#)) and all considered targets are within 140pc. Circumstellar disks can cause significant reddening (e.g. 2MASS 10065573-6352086 has a visual extinction of $A_V = 0.16 \pm 0.04 \text{mag}$) but many targets are not affected at all ([Pecaut and Mamajek \[2016\]](#)). For this thesis, circumstellar reddening was also neglected.

The adjusted model grid F_{MD} can then be used to characterise companion candidates found in observations. In a first step, each model of the grid is fitted to the spectrum using only the distance D of equation 14 as a free parameter. Afterwards, the correlation between the fitted model and the observed spectrum can be calculated to find the best fit model. The parameters of this model are equivalent to a rough estimation of the companion candidate's characteristics. For most observations, the distance D_{obs} to the observed target is known and can be compared to the estimated distance of the best fit model D_{est} .

To determine if an object is bound, the error of the distance estimation needs to be calculated. A first lower estimation of the error σ_D is derived in chapter 5.2. The error estimation σ_D on the distance estimation D_{est} can be calculated with the following equation:

$$\sigma_D = D_{\text{est}} \frac{1.25}{T_{\text{eff}} \times 2.9 \times 10^{-3} \frac{1}{K} - 5.5} \quad (15)$$

Using the estimated distance D_{est} and the characteristics found through model fitting, classification criteria can be defined. In this thesis, a companion candidate is classified as a bound companion if either of the following criteria is fulfilled:

- 1) $|D_{\text{obs}} - D_{\text{est}}| < 2\sigma_D$
- 2) $T_{\text{eff}} \leq 2400\text{K}$

Objects with a temperature lower than 2400K might not be fitted accurately and might not result in a reasonable distance estimation. To minimise false negatives an object it therefore classified as bound if its temperature is below 2400K.

5.2 Temperature-Radius Relation for Brown Dwarfs

The measured flux of an astrophysical point source depends to first order on its temperature, distance, and size. An object is brighter if it is hotter, closer or larger. The temperature of an object can be derived using its spectral information (see chapter 5.1) but the distance and radius are degenerate. As the flux increases linearly with the surface of the object (for a sphere: $F \propto A = 4\pi R_{\text{obj}}^2$) and decreases quadratically with the distance ($F \propto \frac{1}{4\pi D^2}$), a measured object with a given temperature is either be small and close by or large and far away and would produce the same signal. In this section a relation between the temperature and radius of brown dwarfs and M-dwarfs is derived to lift this degeneracy.

The mass, temperature, radius and luminosity of main-sequence stars can be approximated using simple relations. For example, [Kuiper \[1938\]](#) found the empirical relation $L/L_{\odot} = (M/M_{\odot})^4$ for stars with $M < 50M_{\odot}$. Similarly, the temperature-radius degeneracy of main sequence stars can be lifted using the simplified relation $R/T \approx \text{const.}$ As brown dwarfs are significantly colder than main-sequence stars, this relation might no longer hold perfectly.

[Stassun et al. \[2012\]](#) derived an empirical $T_{\text{eff}} - R$ relation for low mass stars between 3300K to 4200K using fourth order polynomials²¹. For this thesis, a linear approximation of their result was chosen using a Taylor approximation of their polynomials around $0.5M_{\odot}$. This leads to the following $T_{\text{eff}} - R$ relation:

$$R = B_0 T_{\text{eff}} + Q_0 = (2.9 \times 10^{-3} \frac{R_{\text{jup}}}{K}) T_{\text{eff}} - 5.5 R_{\text{jup}} \quad (16)$$

Where the parameters $B_0 = 2.9 \times 10^{-3} R_{\text{jup}}/K$ and $Q_0 = -5.5 R_{\text{jup}}$ were calculated using a first order Taylor approximation around $0.5M_{\odot}$.

²¹[Stassun et al. \[2012\]](#) only derived the relations: temperature-mass and radius-mass. The first order Taylor approximation of their derived radius-mass relation around $0.5M_{\odot}$ results in: $M = 0.96(R - 0.5) - 0.49 \approx R$. Therefore, for this thesis, the temperature-mass relation was directly related to the temperature-radius relation.

Quality of the Linear Approximation

To test if objects with $T_{\text{eff}} < 3300K$ follow the derived linear approximation, the temperature and radii of 159 brown dwarfs²² (including some low mass stars) with temperatures between 330K and 3300K were compared to the prediction of the linear $T_{\text{eff}} - R$ model. The comparison of the dataset and the linear approximation can be seen in figure 21.

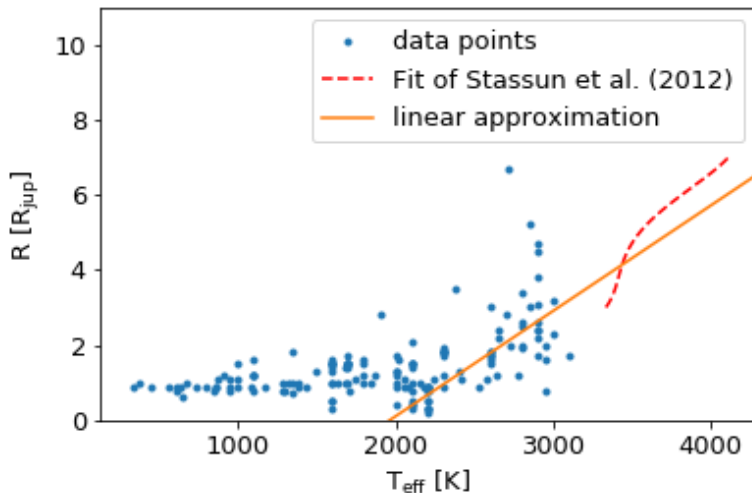


Figure 21: Temperature-radius relation for 159 brown dwarfs (including some low mass stars) compared to the linear approximation derived from the empirical result of Stassun et al. [2012]. The temperatures and radii of the objects represented in this plot are taken from <http://www.johnstonsarchive.net/astro/browndwarflist.html>.

The result displayed in figure 21 indicate that the linear approximation is valid for objects down to approximately 2200K. The radius of objects with a lower temperature stays roughly constant at $1 R_{jup}$. The model grid in chapter 5.1 is limited to 2000K and therefore the linear relation $R = (2.9 \times 10^{-3} R_{jup}/K)T_{\text{eff}} + 5.5R_{jup}$ holds to a reasonable degree within the models parameter space selected for this master thesis. A more detailed $T_{\text{eff}} - R$ relation could be derived to include brown dwarfs with $T_{\text{eff}} < 2000K$ and therefore extending the valid range of the $T_{\text{eff}} - R$ relation.

Error Estimation

Even though the linear approximation fits the general $T_{\text{eff}} - R$ trend of brown dwarfs above 2200K, a large spread in radii for a given temperature can be seen in figure 21 ($0.8 - 5.2R_{jup}$ at $3000 \pm 200K$). This leads to a relative error in radius calculations of up to 80% and therefore is a dominant error source for the model based rejection. To estimate the error, the standard deviations of the data to the linear approximation

²²Data taken from <http://www.johnstonsarchive.net/astro/browndwarflist.html>

was calculated for all objects between 2200K and 3500K. This lead to a standard deviation of $\sigma_{R,1} = 1.09R_{\text{jup}}$.

An additional important error source is the fitting accuracy of the model based rejection (see chapter 5.1). Because the grid has a resolution of 200K, it has an error on the temperature estimation of at least $\sigma_T = 200K$. Using Gaussian error propagation this leads to an error in the radius calculation of $\sigma_{R,2} = B_0\sigma_T = 0.58R_{\text{jup}}$. As $\sigma_{R,1}$ and $\sigma_{R,2}$ are independent, the resulting error on the radius can be written as:

$$\sigma_R = \sqrt{\sigma_{R,1}^2 + \sigma_{R,2}^2} \approx 1.25R_{\text{jup}} \quad (17)$$

To calculate the resulting error estimation on the distance estimation caused by the degeneracy $F \propto (\frac{R}{D})^2$, Gaussian error propagation can be used:

$$c_{fit}^2 = \left(\frac{R}{D}\right)^2 \quad (18)$$

$$\sigma_D = \sigma_R \frac{1}{c_{fit}} = \sigma_R \frac{D}{R} = \sigma_R \frac{D}{B_0 T_{\text{eff}} + Q_0} \quad (19)$$

5.3 Unsuitable Rejection Criteria

During the development of the background star rejection as described in chapter 5.1 many different attempts were made to find a suitable rejection criteria. For completeness, the most important ideas including their advantages and disadvantages are listed in this chapter.

Black Body Fitting

A rough estimation of the temperature could be enough to determine the distance to a companion candidate (using the approximation in equation 13). Therefore, it was tested if a simple black body fit would achieve a reasonable accuracy.

A planetary companion with a temperature between 1800K and 3000K would have its black body peak (according to Wien's Law) in the wavelength range of SPHERE/IFS. A stellar companion would have a peak at wavelengths shorter than the range of SPHERE/IFS covers. Therefore, in theory, a simple black body fit could be used to determine if the temperature is planetary or stellar. On the other hand, the SPHERE/IFS wavelength range of 0.95 - 1.68 μm includes several dominant water absorption bands which change the shape of the spectrum. Because the absorption lines do not follow a black body shape, they bias the fitting substantially.

Simple black body fitting was applied to the Bt-Settl models (Allard et al. [2012]) with the goal to recover their model temperature. The accuracy of the fit strongly depended on the temperature of the model. At low temperature ($T < 2400\text{K}$), the estimation was off by several hundred Kelvin. At high temperatures ($T > 3000\text{K}$), the estimated values from black body fitting were off over 2000K. Therefore, simple black body fitting cannot be used to determine a companion candidate's temperature.

Colour Determination

SPHERE/IRDIS observes in several bands from $0.95 - 2.32\mu\text{m}$, therefore covering a similar range as SPHERE/IFS but with only a few spectral data points. If no SPHERE/IFS data was taken, those data points can be used to calculate a 'colour' of an object. To calculate a 'colour', one broadband filter is subtracted by another. The measured 'colour' can then be compared to model values for a rough characterisation.

This analysis is very similar to the model based rejection with the only difference of using lower resolution measurements (e.g. the broad band filters of SPHERE/IRDIS). As this thesis was focused around SPHERE/IFS, this technique was not further investigated. However, it can be useful if the found objects are outside the FOV of SPHERE/IFS and no spectrum was observed.

Molecular Band Fitting

The shape of a companion candidate's spectrum is given by its black body emission and absorption lines. Because SPHERE/IFS data only observes low resolution spectra, narrow absorption lines ($\text{FWHM} < 0.01\mu\text{m}$) are not detectable but larger absorption bands ($\text{FWHM} > 0.02\mu\text{m}$) are. The idea of molecular band fitting is to use only the absorption bands to fit the model spectra to the observations. The absorption bands are extracted by fitting and subtracting the black body continuum to the observed spectrum and each model in the model grid²³.

This method was tested using the Bt-Settl model (Allard et al. [2012]) on the objects 2MASS J 11555771-5254008 (Ob1) and 2MASS J 13381128-5214251 (Ob2). Ob1 shows a clear absorption band at $1.3 - 1.6\mu\text{m}$ (see figure 22b). Ob2 on the other hand does not have clear features and follows a general black body shape (see figure 22d). The molecular band fitting for Ob1 and Ob2 can be seen in figure 22a and 22c, respectively.

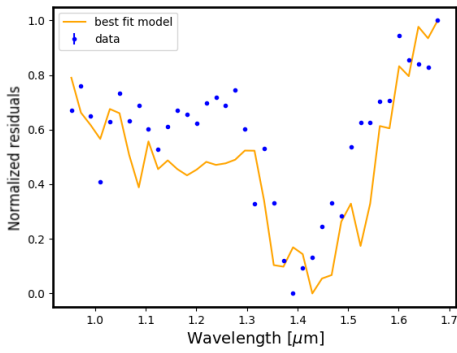
Using molecular band fitting, the water feature around $1.4\mu\text{m}$ in Ob1 was correctly fitted by the model. The best fit calculated with molecular band fitting compared to the non-subtracted spectrum can be seen in figure 22b. It shows that the best fit model starts to deviate from the measurements at shorter wavelengths. The black body subtracted spectrum of Ob2 including the best fit model using molecular band fitting can be seen in figure 22c. The subtracted spectrum only showed a small absorption feature at roughly $1.1\mu\text{m}$. Even though this feature is approximately the same in the best fit model, comparing the non-subtracted model with the observed spectrum in figure 22d shows clear deviation.

Overall, the test results show that the absorption bands are too weak to result in a reasonable fit. Removing the continuum lowers the accuracy of the fit and therefore the accuracy of the temperature estimation.

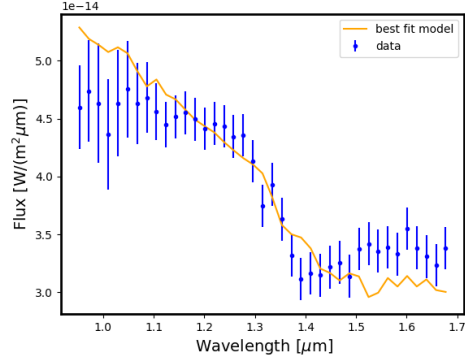
Additionally, a different type of molecular band fitting was implemented into the SpectralCharMod via the parameter *mol_fit* (see chapter 3.6). The module currently supports two different ways to calculate the correlation value: '*full*' and '*H2O*'. If set to '*full*', the whole wavelength range is used to first fit the model to the observed

²³As discussed in this chapter, the black body fit of the models can be biased by absorption lines but the same bias would be present in the observed spectrum. Therefore, the black body subtracted model and the black body subtracted spectrum should have similar shapes.

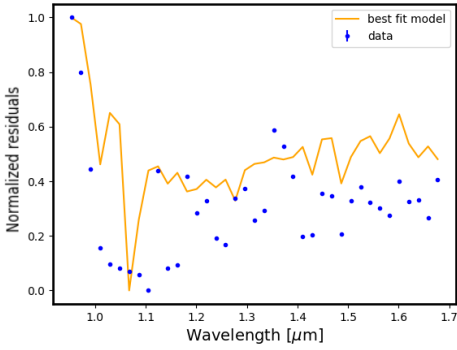
spectrum. Afterwards, the correlation between the fit and the observed spectrum is calculated, again, using the whole wavelength range. If 'H₂O' is selected, only the wavelength range 1.1 - 1.25 μm is used to fit the spectrum as this range has no strong water absorption bands. To calculate the correlation value, the range 1.3 - 1.6 μm is used because it contains a strong water band. Because of time limitations, the H₂O-fitting could not be tested for this thesis and therefore all data was evaluated setting $mol_fit = 'full'$.



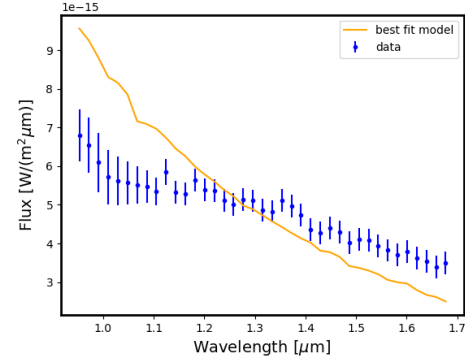
(a) Black Body subtracted and normalised spectrum of Ob1 including best fit model



(b) Observed spectrum of Ob1 including best fit Bt-Settl model



(c) Black Body subtracted and normalised spectrum of Ob2 including best fit model



(d) Observed spectrum of Ob2 including fitted Bt-Settl model

Figure 22: Best fit Bt-Settl models (Allard et al. [2012]) derived with molecular band fitting. The specification of Ob1 and Ob2 are given in table 2. The best fit parameter of Ob1 are: $T_{\text{eff}} = 5800$, $\log g = 2.0$ and $\text{FeH} = 0.5$. The best fit parameter of Ob2 are: $T_{\text{eff}} = 3400$, $\log g = 3.0$ and $\text{FeH} = 1.5$.

5.4 Testing

Methods and Results

To test the model based rejection, the datasets of 51 Eridani from chapter 4 was used²⁴. After a first reduction with EsoReflex, the dataset was prepared using Pipeline 1 and 2. To extract the spectrum of 51 Eridani b, the SimplexMinimizationModule was used with a tolerance of 0.1 magnitude. The model based rejection was applied using the SpectralCharacterizationModule (see chapter 3.6). To calculate the flux, the host stars spectrum is needed which was calculated using the 'Bt-NextGen (AGSS2009)' (Allard et al. [2012]) fitting of the VOSA web page²⁵ (Bayo et al. [2008]). The best fit parameters for the target star are $T_{\text{eff}} = 7200\text{K}$, $\log g = 4$ and $\text{FeH} = 0.0$.

The model based rejection found a best fit for the parameters of 51 Eridani b of $T_{\text{eff}} = 2000\text{K}$, $\log g = 1.0$ and $\text{FeH} = 0.0$. The distance estimation from the fitting of the best fit model is $70 \pm 310\text{pc}$. Because of the temperature criterion ($T_{\text{eff}} < 2400\text{K}$), 51 Eridani b is classified as bound companion.

The extracted spectrum can be seen in figure 23a. The correlation values for all models can be seen in figure 23c and the best fit model compared to the spectrum can be seen in figure 23b. Additionally in figure 23d, the correlation values were averaged over $\log g$ and FeH to analyse the temperature dependence of the correlation values.

Discussion

The spectrum calculated with the SimplexMinimizationModule (see figure 23a) can be compared to the one obtained by Samland et al. [2017] (see figure 24). The three peaks around $1.1\mu\text{m}$, $1.3\mu\text{m}$ and $1.6\mu\text{m}$ can be seen in both figures. On the other hand, the peaks values are slightly smaller in the spectrum calculated by the SimplexMinimizationModule. This could indicated systematic errors from the module which were not taken into account. Additionally, data points below the 5σ curve have only a weak signal and therefore the simplex minimization might not result in accurate flux measurements.

Samland et al. [2017] calculated the following parameters for 51 Eridani b: $T_{\text{eff}} = 760 \pm 20\text{K}$, $\log g = 4.26 \pm 0.25$ and $\text{FeH} = 1.0 \pm 0.1$. The difference between their values and the ones calculated with the model based rejection is explained by the boundaries of the model grid. Especially the lower effective temperature limit of 2000K distorts the results. The correlation values in figures 23c and 23d confirm this explanation because the highest correlation values are found for boundary parameters. Additionally, the difference between the observed spectrum and the best fit model can be seen in figure 23b where especially the spectrum's peak around $1\mu\text{m}$ is not in agreement with the model prediction.

Feigelson et al. [2006] calculated a distance to 51 Eridani of 30pc which can be compared to the $70 \pm 310\text{pc}$ found by the model based rejection. The large error can be explained by the wrongly estimated effective temperature and because the

²⁴Furthermore, in chapters 6.1 and 6.2, the model based rejection was tested on stellar like companion candidates which temperature estimates was within the range of the model grid.

²⁵Available at <http://svo2.cab.inta-csic.es/theory/vosa/>

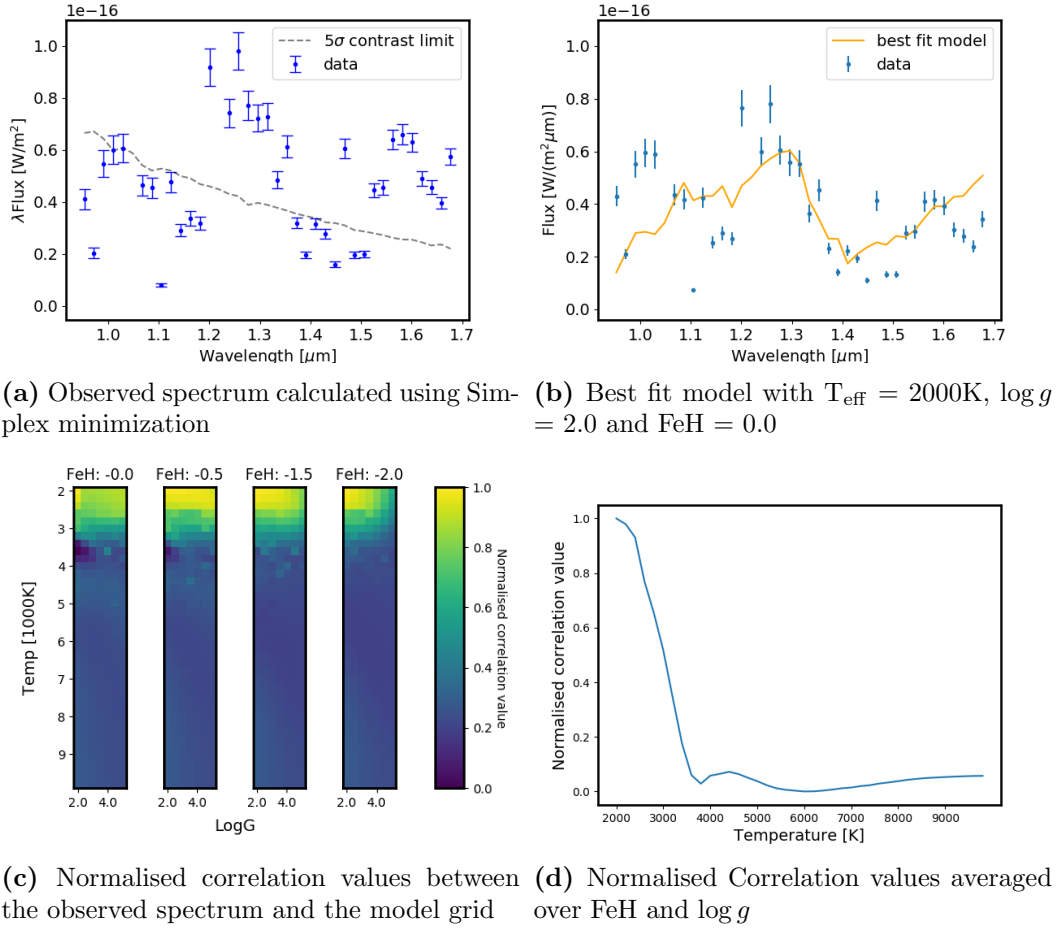


Figure 23: Spectral analysis of 51 Eridani b (PI: J. Beuzit). The flux values were calculated using the SimplexMinimizationModule of PynPoint with a tolerance of 0.1 magnitude. The correlation values were calculated using the model based rejection as described in chapter 5.1. The contrast limit of approximately $\Delta\text{mag} = 15$ magnitudes was taken from figure 12f. The parameters of the best fit model are $T_{\text{eff}} = 2000\text{K}$, $\log g = 1.0$ and $\text{FeH} = 0.0$

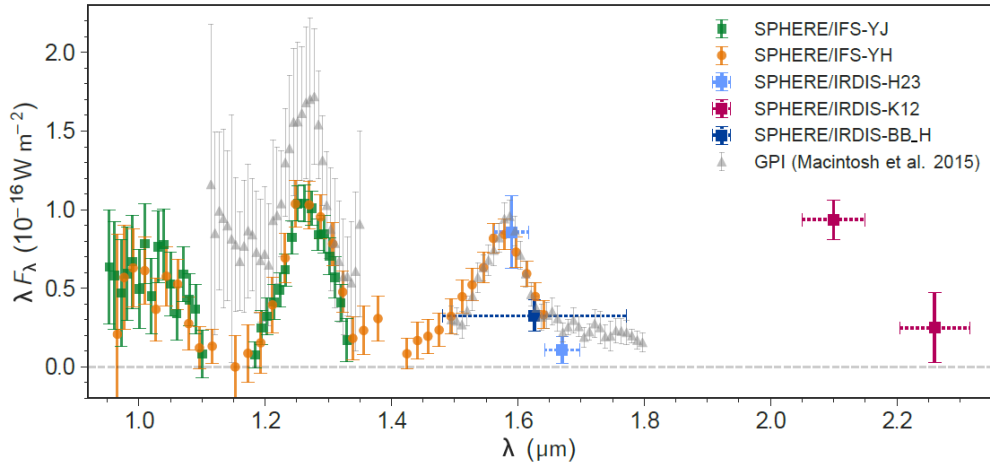


Figure 24: Spectrum of 51 Eridani b obtained by [Samland et al. \[2017\]](#) using SPHERE. Additionally, they compared their spectrum to the one obtained by [Macintosh et al. \[2015\]](#) who discovered 51 Eridani b with the Gemini Planet Imager (GPI).

linear $T_{\text{eff}} - R$ relation is no longer valid at this temperatures. Therefore, this test shows that objects with parameters outside the model grid are not characterised accurately. For accurate results at low temperature, the range of the model grid and the $T_{\text{eff}} - R$ relation's range of validity needs to be expanded.

Overall, a co-movement analysis most likely achieves a better distance estimation and high-resolution spectroscopy would result in a more precise characterisation. Nevertheless, the model based rejection allows to classify companion candidates and roughly characterise them using a single, low resolution measurement.

Search for Exoplanets

Until now, the newly implemented SDI and spectral characterisation tools have only been used on known objects to test the quality of the methods and to find their advantages and disadvantages. In this chapter, the advanced differential imaging techniques are applied to five unpublished datasets (PI: A.J. Bohn). All objects were previously observed but only with SPHERE/IRDIS (PI: M. Kenworthy) and therefore these previous observations were not used for this thesis. All targets are objects in the Sco-Cen association which is around 15 Myr old (Pecaut and Mamajek [2016]). This association is ideal to search for exoplanets via direct imaging because it contains many young, low mass stars.

Table 2: All observations were done using SPHERE/IFS in IRDIFS_EXT mode over the wavelength range 0.95 - 1.68 μ m. DIT stands for detector integration time and NDIT is the total number of images taken. Each dataset has a total rotation of $\Delta\alpha$. Each image contains 39 wavelength frames equally spread over the wavelength range $\Delta\lambda$. The atmospheric seeing is given as approximate value for the atmospheric distortions during the whole observation. (PI: A.J. Bohn; ESO ID: 0101.C-0341(A))

Alias	OB Name	Date	DIT[s] x NDIT	$\Delta\alpha$ [$^\circ$]	Seeing["]
Ob1	2MASS J11555771-5254008	2019-03-27	16 x 32	4.6	<0.8
Ob2	2MASS J13381128-5214251	2019-03-11	64 x 60	32.4	\approx 0.8
Ob3	2MASS J12123577-5520273	2019-03-16	64 x 60	29.6	\approx 0.9
Ob4	2MASS J13251211-6456207	2019-03-22	64 x 6	2.5	>0.9
Ob5	2MASS J13233587-4718467	2019-04-06	64 x 60	38.6	<0.8

All five observations were taken with SPHERE/IFS in IRDIFS_EXT mode. Therefore, each image taken contains the information of 39 wavelength channels over the range 0.95 - 1.68 μ m. After processing the datasets with EsoReflex (Freudling et al. [2013]), this leads to a total of NDIT x 39 frames per observation. The flux images of the target star were taken over the same wavelength range using the ND

1.0 filter and a DIT of 16 seconds. The centring frames were taken separately and therefore the science images do not have waffle spots.

6.1 Object 1: 2MASS J 11555771-5254008

Processing and Results

The target 2MASS J 11555771-5254008 (Ob1) was observed on 27.03.2019 with a total integration time of 8.5 minutes. The distance to Ob1 is 104.9 ± 0.4 pc (taken from GAIA DR2 via the VOSA web page²⁶ (Bayo et al. [2008])). The dataset was first reduced with EsoReflex and afterwards with the PynPoint Pypelines 1 and 2 (as described in chapter 3.7). To search Ob1 for exoplanets, the advanced differential imaging techniques were applied with Pypeline 3 for a range of 0 to 18 principal components. An example of the final detection maps can be seen in figure 25.

Ob1 has a bright point source which is already visible in the raw images. The SNRs of this companion candidate were calculated using the `get_false_alarm_probability` function of PynPoint. The resulting SNRs for all advanced differential imaging techniques using different numbers of principal components can be seen in figure 26a. To determine the detection limits, the contrast curves were calculated using Pypeline 6 for a range of 0 to 18 principal components. The contrast curves discussed in this chapter can be seen in figure 26b; all other contrast curves can be seen in the appendix A, figure 40. The resulting contrasts were compared to the observational limitations calculated with the SPHERE/IFS exposure time calculator²⁷. Because of computational limitations, it was not possible to remove the companion candidate for the calculation of the contrast curve.

To determine the spectrum and position of the companion candidate, Pypeline 4 was used. No advanced differential imaging techniques were applied because the source is sufficiently bright ($\text{SNR} > 5$ without using differential imaging). The contrast between the point source and the target star depends on the wavelength and is between 2.8 ± 0.05 mag (for $\lambda = 1.68\mu\text{m}$) and 3.3 ± 0.1 mag (for $\lambda = 0.95\mu\text{m}$). The position of the point source calculated with the `get_false_alarm_probability` function yielded $SEP = 0.371 \pm 0.003$ arcsec, $PA = 16.8 \pm 0.4^\circ$.

Within Pypeline 4, the spectrum of the point source was analysed using the model based rejection (see chapter 3.6). As the `SdiAperturePhotometryModule` only calculates the contrast of the point source to its host star, the host star's spectrum is needed which was calculated using the 'Bt-NextGen (AGSS2009)' (Allard et al. [2012]) fitting of the VOSA web page. The best fit parameters for the target star are $T_{\text{eff}} = 4500\text{K}$, $\log g = 2.5$ and $\text{FeH} = -0.5$. After calculating the flux of the point source, the model based rejection was used with a full spectrum fit. Its results and the companion candidate's spectrum can be seen in figure 27. The best fit for the companion candidate was found for $T_{\text{eff}} = 3000\text{K}$, $\log g = 4.5$, $\text{FeH} = -0.5$. The distance estimation from the fitting of the best fit model is 60 ± 25 pc.

²⁶Available at <http://svo2.cab.inta-csic.es/theory/vosa/>

²⁷Available at <https://www.eso.org/observing/etc/bin/gen/form?INS.NAME=SPHERE+INS.MODE=IFS>

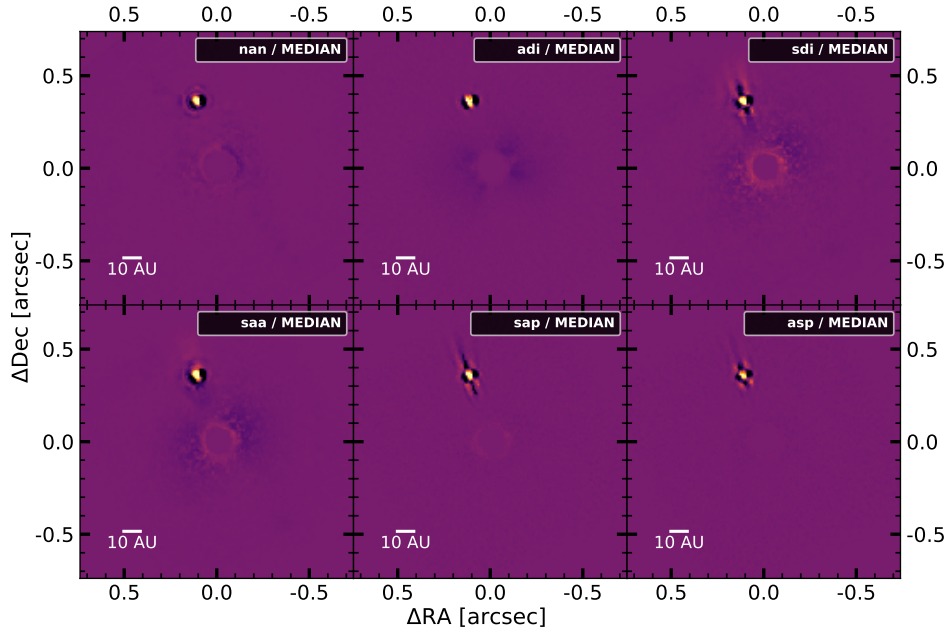
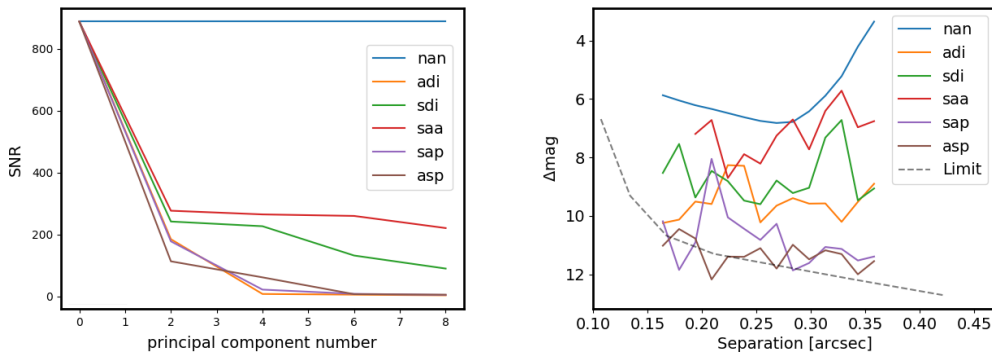
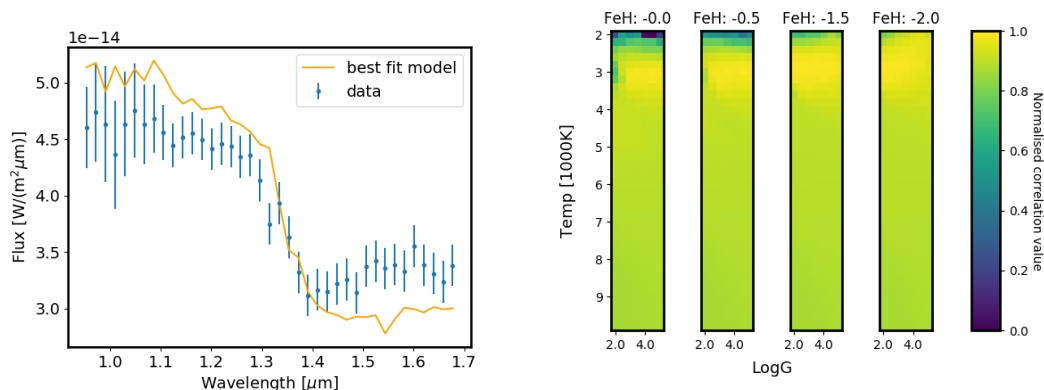


Figure 25: Processed images of Ob1 (Target: 2MASS J 11555771-5254008; PI: A.J. Bohn) using different advanced differential imaging techniques. All images displayed were processed using 2 principal components (except NAN which used 0). The differential imaging techniques are explained in chapter 2.4. The colour-bar of each image is set arbitrary and brighter colours represent higher values.



(a) SNR of the companion candidate using advanced differential imaging techniques **(b)** Contrast curve for 5σ detections using 18 principal components

Figure 26: Analysis of Ob1 (Target: 2MASS J 11555771-5254008; PI: A.J. Bohn) including a companion candidate at $SEP = 0.371 \pm 0.003$ arcsec, $PA = 16.8 \pm 0.4^\circ$. The contrast curves show the 5σ detection limits for further companions. The 'Limit' curve indicates the observational limit and was calculated using the SPHERE/IFS exposure time calculator available at <https://www.eso.org/observing/etc/bin/gen/form?INS.NAME=SPHERE+INS.MODE=IFS>.



(a) Spectra of Ob1 and its best fit from model based rejection (b) Normalised correlation values between the observed spectrum and the model grid

Figure 27: Spectral analysis of the companion candidate found in the dataset Ob1 (Target: 2MASS J 11555771-5254008; PI: A.J. Bohn) using model based rejection (see chapter 5). The model used for the fitting is 'Bt-NextGen (AGSS2009)' (Allard et al. [2012]). The best fit was found for $T_{\text{eff}} = 3000\text{K}$, $\log g = 4.5$, $\text{FeH} = -0.5$. The derived distance estimation to the companion candidate is $60 \pm 25\text{pc}$.

A.J. Bohn analysed Ob1 in two epochs and measured the co-movement of the companion candidate. He disclosed in private communication, that his results indicate that the candidate is bound.

Discussion

The point source found near Ob1 is bright enough to be seen in the raw images. The calculated SNRs in figure 26a show that using advanced differential imaging techniques only reduces the signal through self-subtraction, therefore supporting the findings from chapter 4.3 that PCA is not suitable for targets with a contrast $\Delta\text{mag} < 4$.

Similar to chapter 4.2, SAP and ASP achieve the most favourable contrasts. For the separation range in figure 26b, they reach the observable limit if 18 principal components are used and therefore using more than 18 principal components would not increase the detectable contrast. ADI does not reach that limit but might reach it if more than 18 principal components were used. Similarly, the exact behaviour of SAA could not yet be determined because of the limited principal component number. The results in chapter 4.2 suggest, that SAA could achieve similar contrast curves as SAP or ASP if approximately 300 to 500 principal components are used. Additionally, the unfavourable detection limits of NAN at separation 0.35 can be explained by the influence of the bright companion candidate. Furthermore, the difference between SAP/ASP and ADI becomes bigger for larger separations. This result is in agreement of the one from chapter 4.6 where SDI become more important at larger separations due to a better sampling of the PSF.

The model based rejection predicts a distance of $60 \pm 25\text{pc}$ for the companion candidate compared to the distance to Ob1 of $104.9 \pm 0.4\text{pc}$. This is a 1.8σ difference

and therefore the source is classified as bound. This result matches the findings of A.J. Bohn’s co-movement analysis. The derived characteristics ($T_{\text{eff}} = 3000\text{K}$, $\log g = 4.5$, $\text{FeH} = -0.5$) suggest that the companion candidate is a bound M-dwarf. This estimation could be used as starting parameters for different characterisation methods to characterise the companion more accurately.

6.2 Object 2: 2MASS J 13381128-5214251

Processing and Results

The target 2MASS J 13381128-5214251 (Ob2) was observed on 11.03.2019 for a total integration time of 64 minutes. The distance to Ob2 is $138 \pm 2\text{pc}$ (taken from GAIA DR2 via the VOSA web page²⁸ (Bayo et al. [2008])). The dataset was reduced analogously to Ob1 because it also has a bright point source which is already visible in the raw images.

The SNRs of the companion candidate for all advanced differential imaging techniques can be seen in figure 29a and the contrast curves discussed in this chapter can be seen in figure 29b; all other contrast curves can be seen in appendix A, figure 41. Because of computational limitations, it was not possible to remove the companion candidate for the calculation of the contrast curves. The contrast between the point source and the target star depends on the wavelength and is between $4.96 \pm 0.05\text{mag}$ (for $\lambda = 1.68\mu\text{m}$) and $5.54 \pm 0.12\text{mag}$ (for $\lambda = 1.68\mu\text{m}$). The position of the companion candidate was found to be at $SEP = 0.151 \pm 0.007$ arcsec, $PA = 166 \pm 3^\circ$.

To calculate the flux, the host stars spectrum is needed which was calculated using the 'Bt-NextGen (AGSS2009)' (Allard et al. [2012]) fitting of the VOSA web page. The best fit parameters for the target star are $T_{\text{eff}} = 5200\text{K}$, $\log g = 2.5$ and $\text{FeH} = -0.5$. After calculating the flux of the companion candidate, the model based rejection was used with a full spectrum fit. Its results can be seen in figure 30. The best fit was found for $T_{\text{eff}} = 3600\text{K}$, $\log g = 5.0$ and $\text{FeH} = -2.0$. The distance estimation from the fitting of the best fit model is $360 \pm 90\text{pc}$.

A.J. Bohn analysed Ob2 in two epochs and measured the co-movement of the companion candidate. He disclosed in private communication, that his results indicate that the candidate is bound.

Discussion

The companion candidate found near Ob2 is bright enough to be seen in the raw images. The calculated SNRs in figure 29a show that using advanced differential imaging techniques only reduces the signal through self-subtraction, therefore agreeing with the findings in chapter 4.3 that PCA can cause significant self-subtraction for targets with a contrast $\Delta\text{mag} < 6$. There is a slight increase in SNR for SAP and SAA at 4 principal components. In chapter 4.3 it was found that SAA using less than 12 principal components could increase the SNR of bright targets without

²⁸ Available at <http://svo2.cab.inta-csic.es/theory/vosa/>

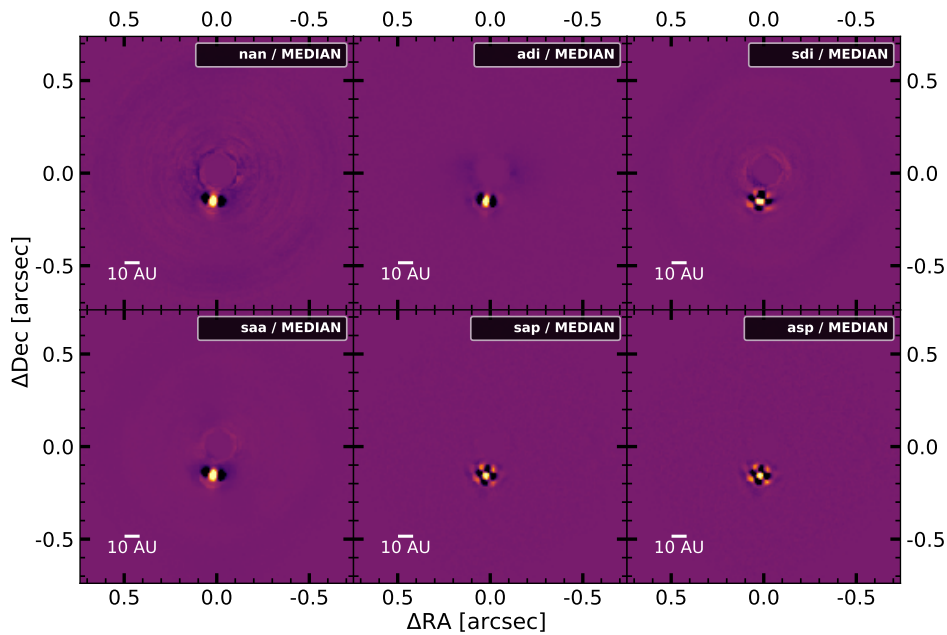


Figure 28: Processed images of Ob2 (Target: 2MASS J 13381128-5214251; PI: A.J. Bohn) using different advanced differential imaging techniques. All images displayed were processed using 2 principal components (except NAN which used 0). The differential imaging techniques are explained in chapter 2.4. The colour-bar of each image is set arbitrary and brighter colours represent higher values.

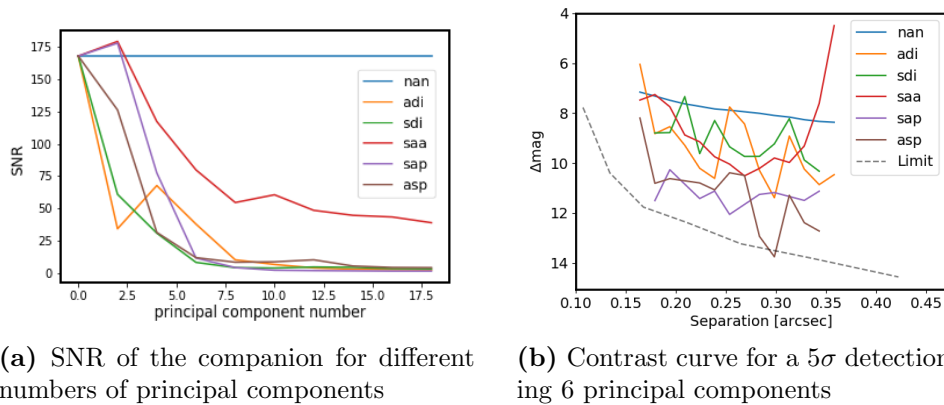
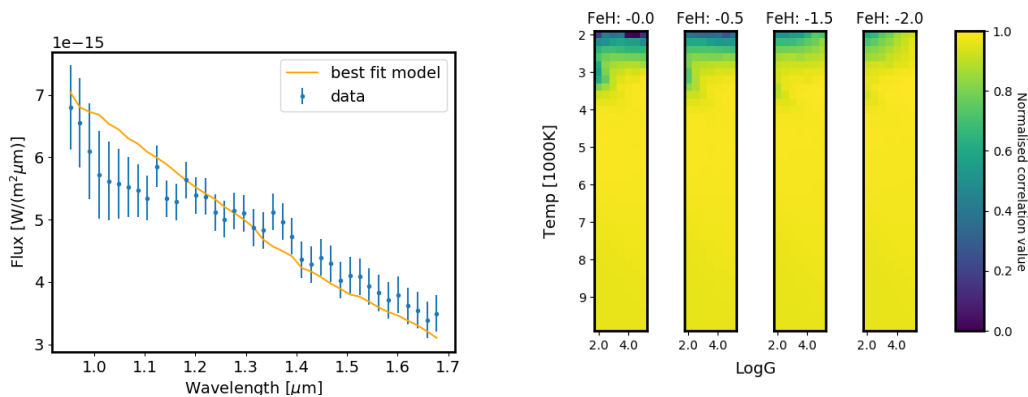


Figure 29: Analysis of Ob2 (Target: 2MASS J 13381128-5214251; PI: A.J. Bohn) including a companion candidate at $SEP = 0.151 \pm 0.007$ arcsec, $PA = 166 \pm 3^\circ$. The contrast curves show the 5σ detection limits for further companions. The 'Limit' curve indicates the observational limit and was calculated using the SPHERE/IFS exposure time calculator available at <https://www.eso.org/observing/etc/bin/gen/form?INS.NAME=SPHERE+INS.MODE=IFS>.



(a) Spectra of Ob2 and its best fit from (b) Normalised correlation values between model based rejection the observed spectrum and the model grid

Figure 30: Spectral analysis of the companion candidate found in the dataset Ob2 (Target: 2MASS J 13381128-5214251; PI: A.J. Bohn) using model based rejection (see chapter 5). The model used for the fitting is 'Bt-NextGen (AGSS2009)' (Allard et al. [2012]). The best fit was found for $T_{\text{eff}} = 3600\text{K}$, $\log g = 5.0$ and $\text{FeH} = -2.0$. The derived distance estimation to the companion candidate is $360 \pm 90\text{pc}$.

significant self-subtraction. The equivalent increase of SAP might hint to a preference of this method over ASP for close in bright targets. Because the performance of the advanced differential imaging techniques vary strongly depending on the target, more datasets need to be analysed to make a generalizable statement. On the other hand, typical companions found via direct imaging are faint and therefore a further analysis would not be applicable to most observations.

Similar to Ob1, SAP and ASP achieve the highest contrast. Compared to ADI, they can detect companions up to 2 magnitudes fainter. This result contradicts expectations, because the relative performance of ADI and the advanced differential imaging techniques was expected to depend on the separation. An explanation would be, the seeing of ≈ 0.8 arcsec for this measurement which could increase the influence of the stellar PSF. A calculation of the contrast curves at separations larger than 0.35 arcsec would help to further study this effect.

The model based rejection predicts a distance of $360 \pm 90\text{pc}$ for the companion candidate compared to the distance to Ob2 of $138 \pm 2\text{pc}$ which is a 2.4σ difference. Additionally, the estimated temperature $T_{\text{eff}} = 3600\text{K}$ is above 2400K . Therefore, according to the classification criteria of the model based rejection, the companion candidate is classified as background source. This result matches the findings of A.J. Bohn's co-movement analysis. The derived characteristics ($T_{\text{eff}} = 3600\text{K}$, $\log g = 5.0$, $\text{FeH} = -2.0$) suggest that the companion candidate is a K star. This estimation could be used as starting parameters for different characterisation methods to characterise the companion more accurately.

6.3 Object 3: 2MASS J 12123577-5520273

Processing and Results

The target 2MASS J 12123577-5520273 (Ob3) was observed on 27.03.2019 with a total integration time of 64 minutes. The distance to Ob3 is 113.3 ± 0.4 pc (taken from GAIA DR2 via the VOSA web page²⁹ (Bayo et al. [2008])). The dataset was first reduced with EsoReflex and afterwards with the PynPoint Pypelines 1 and 2 (as described in chapter 3.7). To search Ob3 for exoplanets, the advanced differential imaging techniques were applied with Pypeline 3 for a range of 0 to 18 principal components. An example of the final images can be seen in figure 31.

To determine the detection limits, the contrast curves were calculated using Pypeline 6 for a range of 0 to 18 principal components. The contrast curves discussed in this chapter can be seen in figure 32; all other contrast curves can be seen in appendix A, figure 42. The resulting contrasts were compared to the observational limitations calculated with the SPHERE/IFS exposure time calculator³⁰.

Discussion

In all final images of Ob3, no possible companion was found. Some residual structure is still visible after using SAP or ASP with less than 6 principal components. In all images processed with SAP and ASP using more than 6 principal components the whole image consists of homogeneous noise. In comparison to Ob4 or Ob5 the remaining structure does not resemble residual star noise but rather forms an ellipse around the central star at a separation of $\approx 0.4 - 0.6$ arcsec. The structure is slightly better visible using SAP than using ASP but it can be detected with both. Using only ADI or SDI no clear structure is visible.

A possible explanation for this source would be a circumstellar disk. Unfortunately, circular symmetric signals are removed using ADI as the rotation does not lead to an offset in signal. The same holds true for SDI and radial symmetries. Thus, it was not expected that SAP or ASP would detect disk like structures as it did in Ob3. To investigate if SAP or ASP are indeed suitable to detect circumstellar disks, further targets (ideally with known disks) need to be analysed.

The contrast curves in figure 32 show that, out of the advanced differential imaging techniques tested SAP, ASP and ADI can detect the faintest exoplanets for all separations. Combining SDI with ADI does not increase the detection limits for this dataset. Additionally, the contrast of SAA and ADI in figure 32b achieve similar results than SAP or ASP. This was not expected, as SAA typically needs more principal components ($\approx 300 - 500$). The similar contrast curves for SAP, ASP, SAA and ADI can be explained with the residual structure found. Similar to stellar speckles, such a structure (e.g. a circumstellar disk) would cover the signal of a companion and limit the detections. Therefore, it is not expected that longer integration times would lead to a more favourable contrast curve.

²⁹ Available at <http://svo2.cab.inta-csic.es/theory/vosa/>

³⁰ Available at <https://www.eso.org/observing/etc/bin/gen/form?INS.NAME=SPHERE+INS.MODE=IFS>

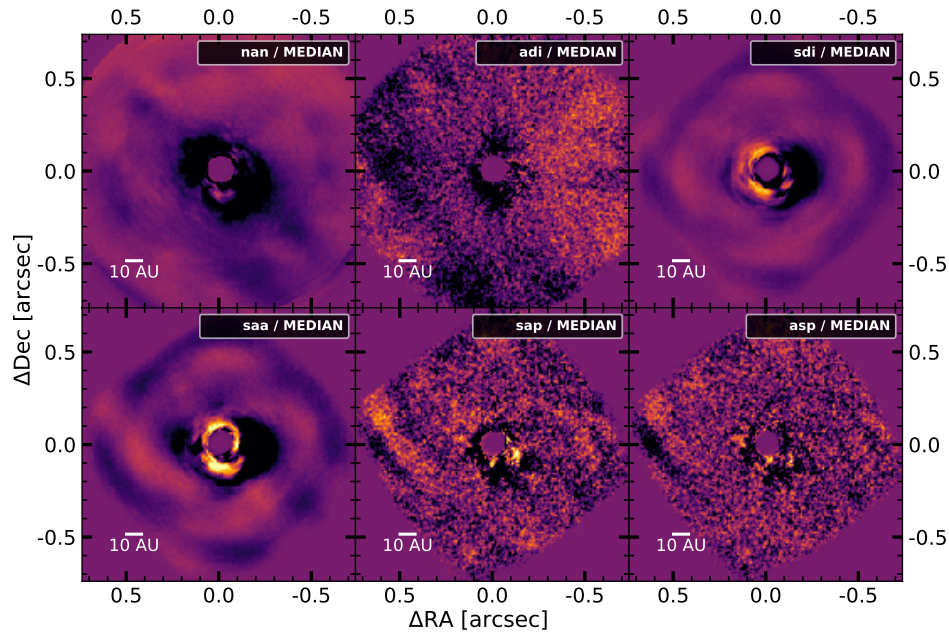


Figure 31: Processed images of Ob3 (Target: 2MASS J 12123577-5520273; PI: A.J. Bohn) using different advanced differential imaging techniques. All images displayed were processed using the principal component number at which the residual structure is best visible (0 for NAN; 4 for ADI, SDI, SAA; 2 for SAP, ASP). The differential imaging techniques are explained in chapter 2.4. The colour-bar of each image is set arbitrary and brighter colours represent higher values.

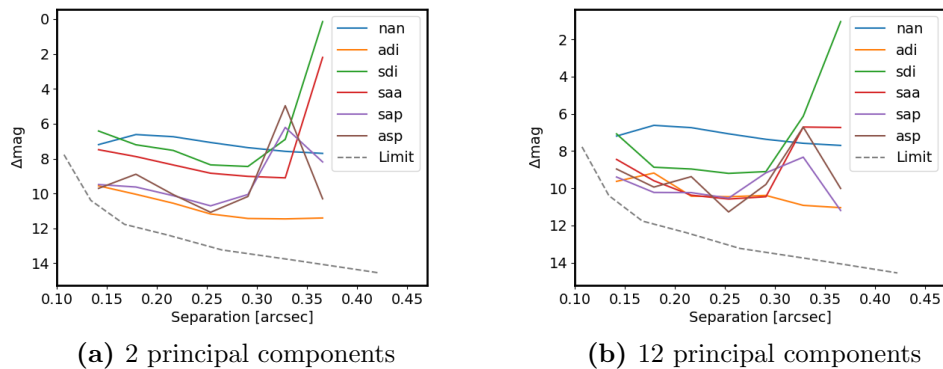


Figure 32: Analysis of Ob3 (Target: 2MASS J 12123577-5520273; PI: A.J. Bohn). The contrast curves show the 5σ detection limits for further companions. The 'Limit' curve indicates the observational limit and was calculated using the SPHERE/IFS exposure time calculator available at <https://www.eso.org/observing/etc/bin/gen/form?INS.NAME=SPHERE+INS.MODE=IFS>.

6.4 Object 4: 2MASS J 13251211-6456207

Processing and Results

The target 2MASS J 13251211-6456207 (Ob4) was observed on 22.03.2019 with a total integration time of 6.4 minutes. The distance to Ob4 is 95 ± 1 pc (taken from GAIA DR2 via the VOSA web page³¹ (Bayo et al. [2008])). The observation was aborted after 6 images due to bad weather conditions (seeing > 1 arcsec and $\tau \approx 3$ ms).

The dataset was first processed with EsoReflex and afterwards with the PynPoint Pypelines 1 and 2 (as described in chapter 3.7). To search Ob4 for exoplanets, the advanced differential imaging techniques were applied with Pypeline 3 for a range of 0 to 4 principal components. An example of the final images can be seen in figure 33. The principal components were limited to 5 because only 6 images were taken.

To determine the detection limits, the contrast curves were calculated using Pypeline 6 for a range of 0 to 4 principal components. The contrast curves can be seen in figure 34. The resulting contrasts were compared to the observational limitations calculated with the SPHERE/IFS exposure time calculator³².

Discussion

Because this observation was terminated after 6 images, low contrast curves as seen in figure 34 were expected. On the other hand, the higher contrasts achieved by ADI compared to SAP or ASP were not expected. The high atmospheric seeing (seeing > 1 arcsec) increases the speckles caused by NCPAs which were expected to be better removed by SDI-ADI combinations than with ADI alone. A closer inspection of the images processed with ADI revealed several pixel values smaller than 10^{-50} . A possible explanation for these low values is over-subtraction from the PCA. Because of the low number of images, a PCA reduction using 4 principal components already substantially subtracts the image. This could also affect SAP, ASP, SAA and SDI but no close-to-zero values were found for them. This difference could be caused by the rescaling, which adds a radial shift to all images. This effect could be further analysed by reducing a nominal dataset with a large number of principal components. On the other hand, most datasets have a sufficient number of images and therefore a further analysis would not be applicable to most observations.

Furthermore, the very similar contrast limits of SAA and SDI for 2 and 4 principal components in figure 34 was not expected. The behaviour can be partially explained with the low number of images in this dataset. Because the number of PCA reductions used in SDI is equivalent to the number of images taken, this dataset only uses 6 PCA reductions to perform SDI (e.g. Ob2 uses 60 PCA reductions). ADI on the other hand still uses 39 PCA reduction and therefore reduces the images stronger than SAA. A further comparison between ADI, SDI and SAA might reveal how these differential imaging techniques reduce noise. This insight could be used to further improve the advanced differential imaging techniques.

³¹ Available at <http://svo2.cab.inta-csic.es/theory/vosa/>

³² Available at <https://www.eso.org/observing/etc/bin/gen/form?INS.NAME=SPHERE+INS.MODE=IFS>

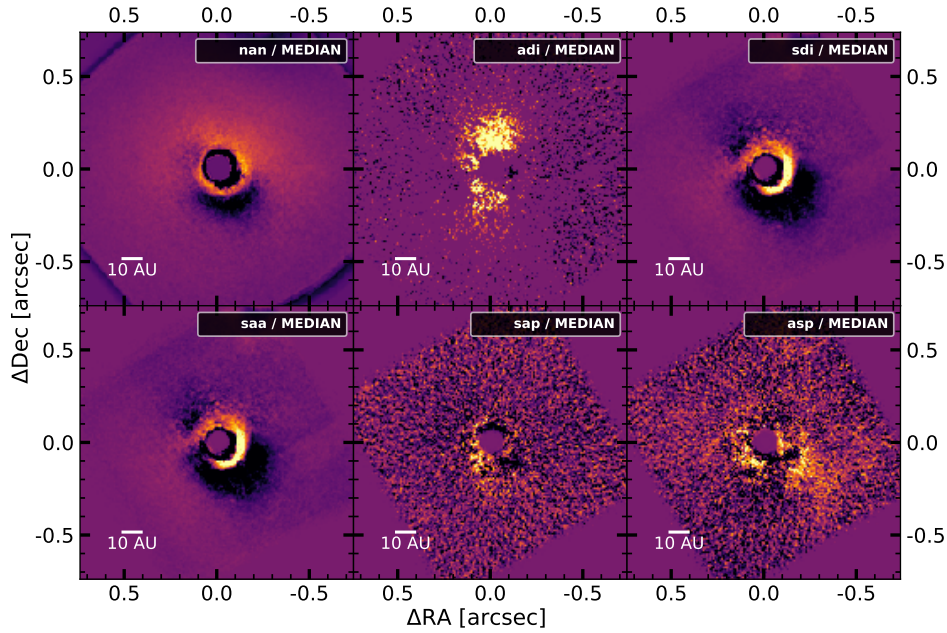


Figure 33: Processed images of Ob4 (Target: 2MASS J 13251211-6456207; PI: A.J. Bohn) using different advanced differential imaging techniques. The observation was aborted after 6 images due to bad weather conditions (seeing $> 1''$ and $\tau \approx 3\text{ms}$). All images displayed were processed using 2 principal components (except NAN which used 0). The differential imaging techniques are explained in chapter 2.4. The colour-bar of each image is set arbitrary and brighter colours represent higher values.

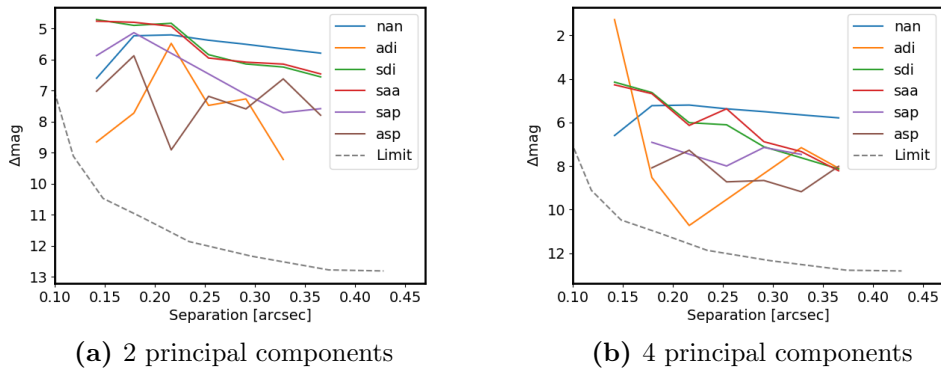


Figure 34: Analysis of Ob4 (Target: 2MASS J 13251211-6456207; PI: A.J. Bohn). The contrast curves show the 5σ detection limits for further companions. The 'Limit' curve indicates the observational limit and was calculated using the SPHERE/IFS exposure time calculator available at <https://www.eso.org/observing/etc/bin/gen/form?INS.NAME=SPHERE+INS.MODE=IFS>.

6.5 Object 5: 2MASS J 13233587-4718467

Processing and Results

The target 2MASS J 13233587-4718467 (Ob5) was observed on 06.04.2019 with a total integration time of 64 minutes. The distance to Ob5 is 122 ± 1 pc (taken from GAIA DR2 via the VOSA web page³³ (Bayo et al. [2008])). The dataset was first processed with EsoReflex and afterwards with the PynPoint Pypelines 1 and 2 (as described in chapter 3.7). To search Ob5 for exoplanets, the advanced differential imaging techniques were applied with Pypeline 3 for a range of 0 to 18 principal components. An example of the final images can be seen in figure 35.

To determine the detection limits, the contrast curves were calculated using Pypeline 6 for a range of 0 to 18 principal components. The contrast curves discussed in this chapter can be seen in figure 36; all other contrast curves can be seen in appendix A, figure 43. The resulting contrasts were compared to the observational limitations calculated with the SPHERE/IFS exposure time calculator³⁴.

Discussion

In all final images of Ob5, no companion candidate was found. Some residual structure of the stellar PSF is still visible after using SAP or ASP with less than 8 principal components. All images processed with SAP and ASP using more than 8 principal components consist of homogeneous noise. The same holds true for ADI with a threshold of 14 principal components. SDI and SAA still show residual structures at >18 principal components. In the case of SAA, this was expected as this technique typically achieves the best results at over 200 principal components (see section 4.2). In the case of SDI, circular patterns remain. Because no ADI is used, rotationally static sources (e.g. instrumentation effects) are not reduced well. After derotating and stacking the dataset to create the final image, these effects can lead to circular residuals.

The contrast curves in figure 36 show that, out of the advanced differential imaging techniques tested SAP, ASP and ADI can detect the faintest exoplanets for all separations. Combining SDI with ADI does not increase the detection limits therefore contradicting expectations. Additionally, the contrast of SAA in figure 36b is equivalent to the one from ADI. This was not expected, as SAA typically needs more principal components ($\approx 300-500$) to achieve similar results as SAP or ASP. Similar to Ob3, this effects could be explained by an additional faint source around Ob5. For example, a circumstellar disk around Ob5 could explain the low detection limits.

Comparing the contrast curves of Ob1 to Ob5, no contrast larger than 12 magnitude was found. Therefore, an additional limiting factor from the instrument or image processing which is not considered in the 'Limit' calculation could be an explanation for the difference to the measured contrast curves. This explanation could be tested by re-analysing an archived dataset with optimal observation conditions.

³³ Available at <http://svo2.cab.inta-csic.es/theory/vosa/>

³⁴ Available at <https://www.eso.org/observing/etc/bin/gen/form?INS.NAME=SPHERE+INS.MODE=IFS>

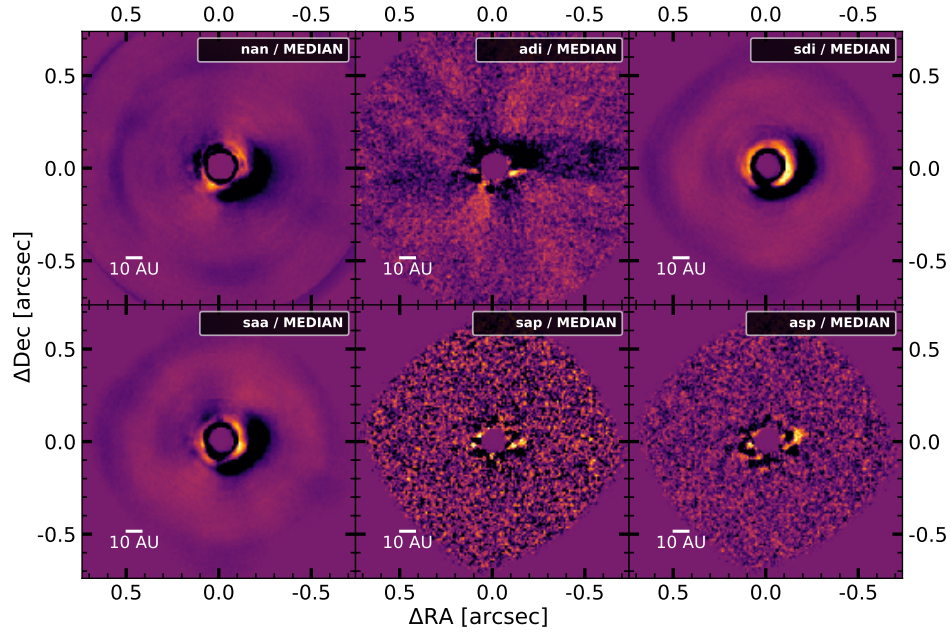


Figure 35: Processed images of Ob5 (Target: 2MASS J 13233587-4718467; PI: A.J. Bohn) using different advanced differential imaging techniques. All images displayed were processed using 4 principal components (except NAN which used 0). The differential imaging techniques are explained in chapter 2.4. The colour-bar of each image is set arbitrary and brighter colours represent higher values.

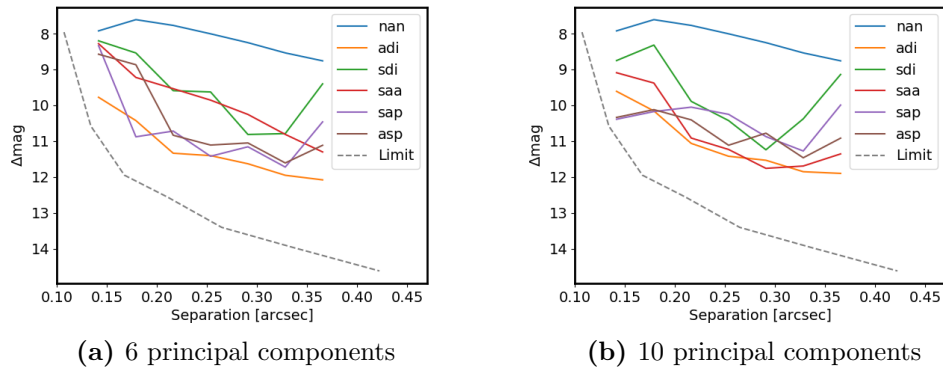


Figure 36: Analysis of Ob5 (Target: 2MASS J 13233587-4718467; PI: A.J. Bohn). The contrast curves show the 5σ detection limits for further companions. The 'Limit' curve indicates the observational limit and was calculated using the SPHERE/IFS exposure time calculator available at <https://www.eso.org/observing/etc/bin/gen/form?INS.NAME=SPHERE+INS.MODE=IFS>.

Conclusion

In this thesis, SPHERE/IFS support was added to the python package PynPoint thus allowing to use spectral information to process direct imaging data and to extract the spectrum of observed objects. The implementations were then used to achieve the three goals of this thesis:

- **Goal 1:** Implement and test the power of advanced differential imaging techniques, based on the spectral and angular diversity in the data, and determine the detection limits of the corresponding reductions.
- **Goal 2:** Develop tools for characterisation of potential companions and rejection of background contaminants by spectral analysis.
- **Goal 3:** Use advanced differential imaging techniques to search for companion candidates in five unpublished datasets and, if successful, characterise the source as bound to the observed star or as background object.

In this section the conclusion for the three main goals is drawn according to the findings of chapters 4, 5 and 6.

Goal 1: Advanced Differential Imaging Techniques

During this thesis, SDI was implemented into the framework of PynPoint using the spectral information of SPHERE/IFS. Because PynPoint already supports ADI, the newly implemented SDI could be combined with ADI to create three advanced differential imaging techniques: ASP, SAP and SAA. In PynPoint, the advanced differential imaging techniques were added to the PcaPsfSubtractionModule, allowing to select the advanced differential imaging techniques by keyword. Additionally, several data preparation and reduction modules were adjusted to enable the same processing for SPHERE/IFS data as for SPHERE/IRDIS data. The only step not yet included is the initial reduction from raw data to wavelength cubes which is done with the EsoReflex pipeline.

The advanced differential imaging techniques were tested up to 18 principal components by applying them on Beta Pictoris b, 51 Eridani b and HR 8799 e.

In all cases, the techniques SAP and ASP could detect the exoplanets with higher SNRs than ADI. This improvements come at the cost of longer computational times. For these analysed targets, SAP and ASP achieved their highest SNRs when using no more than 12 principal components whereas SAA required over 300. Because of this difference and computational limitations, SAA could not be analysed with its ideal number of principal components. Using SDI alone always lead to lower SNRs than using only ADI.

Furthermore, the contrast curves of the three objects were calculated with up to 18 principal components for the innermost 0.3 arcsec. Depending on the target, ASP and SAP can detect objects 1-2 magnitudes fainter than ADI in this inner region. Comparing the results of 51 Eridani to [Samland et al. \[2017\]](#) and HR 8799 to [Zurlo et al. \[2016\]](#) showed that SAP and ASP can achieve similar contrast values than used in current publication.

The SNR dependence on target brightness Δmag , observed wavelength range $\Delta\lambda$, total angular rotation $\Delta\alpha$ and total integration time Δt was analysed using Beta Pictoris as test target. The test on companion brightness showed, that PCA analysis is not suitable for targets with $\Delta\text{mag} < 4$ because of strong self-subtraction effects. For the wavelength range dependence, it was found that the SNRs increase for larger wavelength ranges for the techniques SAP and ASP. Therefore, detections with SAP and ASP can be optimised by observing larger wavelength ranges. The test on total angular rotation, showed a linear increase in SNR for $\Delta\alpha \leq 1.6$ FWHM of the companion's PSF. At larger total rotations, no significant SNR increase with increasing $\Delta\alpha$ was found. For short integration times, the SNR increases according to the photon noise limit with the square root of Δt . After a certain Δt , the stellar speckles become the dominant noise source and the SNR does no longer increase with integration time. In the case of Beta Pictoris reduced with SAP or ASP, the SNR increased up to $\Delta t = 1500s$ after which no SNR increases was found. As the performance of the advanced differential imaging techniques strongly depended on the target, analysing more targets could help generalizing these results.

All advanced differential imaging techniques implemented into Pynpoint use the same number of principal components for ADI and SDI (e.g. $\text{SDI}(K) \rightarrow \text{ADI}(K)$). A further investigation in the differential imaging techniques $\text{SDI}(N) \rightarrow \text{ADI}(M)$ and $\text{ADI}(M) \rightarrow \text{SDI}(N)$ with $0 \leq M, N \leq 4$ showed that the best combination of M and N is target specific. None of the three targets Beta Pictoris b, 51 Eridani b and HR 8799 e achieved the highest SNR with the same reduction technique therefore confirming that the best technique can differ depending on the target. A similarity found in all three targets was significantly lower SNRs if only ADI or SDI was used. Therefore, showing that advanced differential imaging techniques achieve higher SNRs than ADI alone.

Additionally, the STIM detection map proposed by [Pairet et al. \[2019\]](#) was implemented and tested on the targets Beta Pictoris b, 51 Eridani b and HR 8799 e. For Beta Pictoris b it resulted in lower SNRs, for 51 Eridani it achieved slightly higher SNRs and no difference could be found for HR 8799 e. Therefore, their claim that the STIM module is useful to detect companions at small separations could not be confirmed.

Goal 2: Characterisation and Background Rejection

The SPHERE/IFS support to PynPoint allows for a faster extraction of spectra from observations without manually splitting the dataset into its wavelength channels. Additionally, the pre-existing modules were adjusted to correctly handle wavelength information.

To classify companion candidates as bound companions or background sources, the model based rejection was developed and implemented into PynPoint within the SpectralCharModule. This method uses a low resolution model grid ($\Delta T_{\text{eff}} = 200\text{K}$, $\Delta \log g = 0.5$, $\Delta \text{FeH} \approx 0.5$) of the Bt-Settl model (Allard [2013]) which is fitted to the observed spectrum. It then calculates the correlation value to find the best fit model and a distance estimation via the fitting parameter. For this thesis, a companion candidate was classified as bound if the estimated distance is within 2σ of the known distance to the observed star. To minimise false negatives, an object was also classified as bound if its temperature is below 2400K because of the model grid limitations. Additionally, the parameters of the best fit model allow for a rough characterisation of the found object.

The classification from model based rejection is less precise than co-movement analysis but it allows to classify companion candidates as bound or background using a single observation with SPHERE/IFS. Additionally, T_{eff} , $\log g$, FeH and distance estimations can be used for a rough characterisation of companion candidates in order to determine their value for follow-up studies.

Goal 3: Search for Exoplanets

The newly implemented advanced differential imaging techniques and the model based rejection were used to analyse five targets: 2MASS J 11555771-5254008 (Ob1), 2MASS J 13381128-5214251 (Ob2), 2MASS J 12123577-5520273 (Ob3), 2MASS J 13251211-6456207 (Ob4) and 2MASS J 13233587-4718467 (Ob5). All were searched for exoplanets and the detection limits were determined using the advanced differential imaging techniques with up to 18 principal components. Ob1 and Ob2 each contain a bright companion candidate which was already visible in the raw images, but no additional companion was found. No companion was found in Ob3, Ob4 or Ob5.

The companion candidates found in the datasets Ob1 and Ob2 were analysed using the model based rejection. The candidate in Ob1 was found at $SEP = 0.371 \pm 0.003$ arcsec, $PA = 16.8 \pm 0.4^\circ$ and it was classified as a bound M-dwarf with estimated characteristics: $T_{\text{eff}} = 3000\text{K}$, $\log g = 4.5$ and $\text{FeH} = -0.5$. Its distance was estimated at $60 \pm 25\text{pc}$. The candidate in Ob2 was found at $SEP = 0.151 \pm 0.007$ arcsec, $PA = 166 \pm 3^\circ$ and it was classified as a background K-dwarf with estimated characteristics: $T_{\text{eff}} = 3600\text{K}$, $\log g = 5.0$ and $\text{FeH} = -2.0$. Its distance was estimated at $360 \pm 90\text{pc}$. A.J. Bohn analysed both Ob1 and Ob2 in two epochs and confirmed the classification by the model based rejection in private communication.

Outlook

This thesis covered many topics around SPHERE/IFS data including the advanced differential imaging techniques and spectral characterisation tools. This outlook of future research will focus on the next steps necessary to build on the research accomplished in this master thesis. Finally, the perspective will be broadened to the future of exoplanetary research and an insight on what to expect in the next decade.

8.1 Next Steps

The first part of this thesis focused on goal 1: the implementation of SDI into PynPoint and its testing. The second part dealt with goal 2: the processing and analysis of spectra from exoplanets and on how to distinguish background sources. During both parts, many other topics were touched upon but because of time limitations not further investigated. This chapter lists the next steps to advance these parts, ordered in rank of importance.

Update PynPoint

One of the major advantages of PynPoint is its easy handling of direct imaging data and large repository of different processing modules. It allows to set up adjustable pipelines to process and analyse, for example, SPHERE/IRDIS data. These Pipelines can be used on all observations with only minor adjustments which allows to prepare for future observations or to re-analyse archive data.

Therefore, an important next step would be to include the new functionalities in the official version of PynPoint. The version of PynPoint developed over the course of this thesis³⁵ can be used to gradually update PynPoint and to add the necessary functionalities to evaluate SPHERE/IFS data. This requires changes in the core functions of PynPoint and therefore needs to be done with care and requires time. Additionally, rigorous testing would be necessary to ensure the quality of the final

³⁵Available on GitHub: https://github.com/Kiefersv/PynPoint/tree/MasterThesis_Sven_Kiefer

product. Nevertheless, it is well worth the effort because the spectral information gained allows to investigate exoplanet atmospheres and therefore PynPoint should fully support it.

Furthermore, the implementation of the advanced differential imaging techniques substantially increases computational intensity. During this thesis, multiprocessing support was added to some of the more computationally intensive modules (e.g. ContrastCurveModule and SimplexMinimizationModule). Unfortunately, this only helps distribute the workload but not reduce it. Therefore, an important next step is to optimise the computational time of PynPoint’s advanced differential imaging techniques. This was not done during this thesis which focused on their implementation and testing.

Further Improvements and Testing

The test results of chapter 4 are very promising regarding SAP and ASP. Because of the computational limitation, they could only be tested on one to three datasets. As the performance of the advanced differential imaging techniques strongly depends on the target, the conclusions might not generalise to all targets. With an official update of PynPoint, testing becomes more accessible and the tests done during this thesis can be repeated on other targets to generalise the presented results.

Furthermore because of the computational limitations, the advanced differential imaging technique SAA could not be analysed properly. It can require over 300 principal components to achieve similar results as SAP and ASP. Repeating the tests in section 4 and comparing the results of the advanced differential imaging techniques used with their optimal number of principal components might lead to new insights on these techniques. Before such a comparison is feasible, the implementation of SDI and its combination with ADI needs to be optimised to reduce computing time.

In chapter 4, the effect of various influences on the SNR was analysed. Because many different parameters influence the SNR (e.g. rotation, wavelength range, integration time and target brightness), each test tried to isolate one factor by keeping the others constant. In doing so, only a small subspace of the whole parameter space was tested. To see how the SNR can be optimised, it would help to investigate the whole parameter space at once. Using for example MCMC or machine learning techniques, the SNRs dependence on various factors could be determined more accurately.

Furthermore, all tests in chapter 4 for SAP or ASP were conducted using the same principal component number in ADI and SDI but the results from chapter 4.6 showed, that using different principal component numbers can increase their performance. Because the number of possible reduction steps goes exponentially with the principal component number, an efficient way to search these differential imaging techniques needs to be developed.

Zurlo et al. [2016] and Samland et al. [2017] carefully selected the reduction images for each frame. Currently, PynPoint does not support a simple handling of such a method. Adding a module which selects reduction frames according to selection criteria (e.g. companion offset between frames) might increase the SNR of the detections obtained with the advanced differential imaging techniques.

Investigate Archival Data

Because for this thesis the SPHERE/IFS support first had to be implemented into PynPoint, only three known and five new targets could be analysed. Fortunately, as the framework to evaluate SPHERE/IFS data is now developed, spectral data can be analysed faster. Because the results showed a clear advantage of advanced differential imaging techniques over ADI, they can now be used to further investigate archived SPHERE/IFS data.

First, data of known exoplanets can be analysed. This allows to compare the found results with publications and therefore to further test the PynPoint implementation of the advanced differential imaging techniques. This difference can thus help to improve the PynPoint implementation. Possible targets can be found in the paper by [Bowler et al. \[2020\]](#).

As a next step, large surveys can be used to search for exoplanets using advanced differential imaging techniques. For example, the ongoing SPHERE infrared survey for exoplanets (SHINE) observes 400-600 stars ([Chauvin et al. \[2017\]](#)) which could be analysed using PynPoint. This would help to improve the implementation of the techniques and might result in the discovery of new exoplanets.

Improve Model Based Rejection

The model based rejection derived in chapter 5.1 can help to distinguish companions from background sources and therefore eliminate targets not worth a second observation. This saves time and resources. In this thesis, the model based rejection correctly classified three previously analysed targets: 51 Eridani b, the companion of Ob1 and the background source of Ob2.

To further improve classification and to reduce the false negative rate, the model based rejection as presented in chapter 5.1 should be improved. First, the range of the model grid should be increased. The framework of the model based rejection even allows to combine several models, therefore a larger parameter space could be covered. Especially the temperature range needs to be extended below 2000K as exoplanets are expected to be colder than that. Possible models would be the 'Drift-Pheonix' ([Baron et al. \[2003\]](#)) or AMES-Cond 2000 ([Baraffe et al. \[2003\]](#)) both of which extend below 2000K. Additionally, the temperature-radius relation for brown dwarfs should be improved. The linear approximation leads to larger errors and a better determination of the radius would also reduce the error on the distance estimation. A possible next step to improve the relation could be using the $\log g$ estimation from the best fit model and relating it to the radius. Additionally, the derived error on the distance estimation is influenced by the fitting error. For this thesis, the lower limit given by the model grid was used. For a more precise error calculation, it should be derived from the correlation values.

Even though, the model based rejection only allows rough characterisations, improving it could help build tools which improve observations by determining interesting targets faster.

8.2 The Future of Exoplanet Research

Finding exoplanets is difficult and characterising them is even more challenging. To tackle this task, state-of-the-art instrumentations are constantly improved and data processing techniques are developed and refined. Together, they lead to thousands of exoplanet discoveries over the past 30 years. Some of these were characterised by comparing atmospheric models of various complexity to the observations with techniques like atmospheric retrieval (Madhusudhan [2018]).

This thesis built on the processing techniques for direct imaging developed over the past decades and contributed to them by granting new insights into the advanced differential imaging techniques. By implementing these techniques in the framework of PynPoint, they become accessible for further studies and will hopefully help to discover new exoplanets. The newly developed model based rejection can identify background sources with a single, low resolution measurement. This allows to optimise future observations and helps identifying interesting targets for follow up studies.

The diversity of exoplanets and planetary systems in our galaxy are slowly uncovered. The discovery of the Trappist-1 (Gillon et al. [2016]) and the HR 8799 system (Marois et al. [2008]) proofed that the solar system is not the only multi-planetary object and, at the same time, showed that such systems can be substantially different than ours. It is now known that most stars have one or more exoplanets (Cassan et al. [2012]) but if solar like planetary systems are common remains to be discovered.

In the next decade, many new and exciting telescopes are going to be built and launched. No elaboration on exoplanet research would be complete without mentioning the James Webb Space Telescope, which (hopefully) will be launched next year. On the ground, the successor of the VLT is coming: the extremely large telescope (ELT). Those instruments mark the start of a new area of exoplanet research. Hopefully, they will lead to many exoplanet discoveries including small, rocky exoplanets

For the first time in history, mankind will be able to actively search for other habitable planets. Even though many answers have been found in the last 30 years and many more question have arisen, the possible existence of life outside earth remains unsolved and the answer to the question of life, the universe and everything remains to be found.

Acknowledgement

First and foremost, I want to thank Alexander J. Bohn for supervising my master thesis. He gave me the opportunity to work together with him at Leiden University and organised an interesting and challenging project through which I could gather hands on experience in exoplanet research. He was always ready to help and kept motivating me to go beyond the initial goals.

Secondly, I want to thank Sascha P. Quanz who supervised my thesis and helped me shape the direction of my work. He gave me the freedom to develop my own research plan while still keeping my work on track. Likewise, I want to thank Matthew Kennworthy who supported me at Leiden University.

Additionally, I want to thank the various people who helped me with their expertise. Especially, Vanessa Sennrich for correcting my thesis and teaching me how tough referees can be. Moreover, I want to thank Julian Lang, Alex van Vorstenbosch, Hritam Chakraborty, Callum Griffiths, Elise Sanger, Chandramoham Vaishali and Marit Mol Lous for interesting discussions and helpful insights.

Lastly, I want to thank all my colleges from office 401 (especially Macron) and its various guests for creating a friendly and supportive environment. I had an amazing time and hope to someday have the pleasure to work with you again.

Index of Abbreviations

ADI	-	angular differential imaging	PCA	-	principal component analysis
AO	-	adaptive optics	PSF	-	point spread function
ASP	-	ADI then SDI using PCA	SAA	-	SDI and ADI using PCA
DIT	-	detector integration time	SAP	-	SDI then ADI using PCA
FOV	-	field of view	SDI	-	spectral differential imaging
FWHM	-	full width half maximum	SEP	-	separation
IFS	-	integrated field spectroscopy	SNR	-	signal to noise ratio
NCPA	-	non-common path aberration	VLT	-	very large telescope
PA	-	parallactic angle			

References

- F. Allard. The BT-Settl Model Atmospheres for Stars, Brown Dwarfs and Planets. *Proceedings of the International Astronomical Union*, 8(S299):271–272, June 2013. ISSN 1743-9213, 1743-9221. doi: 10.1017/S1743921313008545. URL <https://www.cambridge.org/core/journals/proceedings-of-the-international-astronomical-union/article/btsettl-model-atmospheres-for-stars-brown-dwarfs-and-planets/3D928FD81B6F9B774F69131F4BB7D73F>. Publisher: Cambridge University Press.
- F. Allard, D. Homeier, and B. Freytag. Models of very-low-mass stars, brown dwarfs and exoplanets. *Philosophical Transactions of the Royal Society A: Mathematical, Physical and Engineering Sciences*, 370(1968):2765–2777, June 2012. doi: 10.1098/rsta.2011.0269. URL <https://royalsocietypublishing.org/doi/full/10.1098/rsta.2011.0269>.
- A. Amara, S. P. Quanz, and J. Akeret. PynPoint code for exoplanet imaging. *Astronomy and Computing*, 10:107–115, April 2015. ISSN 2213-1337. doi: 10.1016/j.ascom.2015.01.003. URL <http://www.sciencedirect.com/science/article/pii/S2213133715000049>.
- Adam Amara and Sascha P. Quanz. PYNPOINT: an image processing package for finding exoplanets. *Monthly Notices of the Royal Astronomical Society*, 427:948–955, December 2012. ISSN 0035-8711. doi: 10.1111/j.1365-2966.2012.21918.x. URL <http://adsabs.harvard.edu/abs/2012MNRAS.427..948A>.
- Dániel Apai, Markus Kasper, Andrew Skemer, Jake R. Hanson, Anne-Marie Lagrange, Beth A. Biller, et al. HIGH-CADENCE, HIGH-CONTRAST IMAGING FOR EXOPLANET MAPPING: OBSERVATIONS OF THE HR 8799 PLANETS WITH VLT/SPHERE SATELLITE-SPOT-CORRECTED RELATIVE PHOTOMETRY. *The Astrophysical Journal*, 820(1):40, March 2016. ISSN 1538-4357. doi: 10.3847/0004-637X/820/1/40. URL <http://stacks.iop.org/0004-637X/820/i=1/a=40?key=crossref.0215eb03bbb7b7d1ecd621ee6a89af23>.
- R. Bacon, G. Adam, A. Baranne, G. Courtes, D. Dubet, J. P. Dubois, et al. 3D spectrography at high spatial resolution. I. Concept and realization of the integral field spectrograph TIGER. *Astronomy and Astrophysics Supplement Series*, 113:347, October 1995. ISSN 0365-0138. URL <http://adsabs.harvard.edu/abs/1995A%26AS..113..347B>.
- I. Baraffe, G. Chabrier, T. S. Barman, F. Allard, and P. H. Hauschildt. Evolutionary models for cool brown dwarfs and extrasolar giant planets. The case of HD 209458. *Astronomy & Astrophysics*, 402(2):701–712, May 2003. ISSN 0004-6361, 1432-0746. doi: 10.1051/0004-6361:20030252. URL <https://www.aanda.org/articles/aa/abs/2003/17/aa3343/aa3343.html>. Number: 2 Publisher: EDP Sciences.
- E. Baron, P. H. Hauschildt, F. Allard, E. J. Lentz, J. Aufdenberg, A. Schweitzer, and T. Barman. Highlights of Stellar Modeling with PHOENIX. 210:19, 2003. URL <http://>

- [//adsabs.harvard.edu/abs/2003IAUS..210...19B](https://adsabs.harvard.edu/abs/2003IAUS..210...19B). Conference Name: Modelling of Stellar Atmospheres Place: eprint: arXiv:astro-ph/0209052.
- A. Bayo, C. Rodrigo, D. Barrado y Navascués, E. Solano, R. Gutiérrez, M. Morales-Calderón, and F. Allard. VOSA: virtual observatory SED analyzer - An application to the Collinder 69 open cluster. *Astronomy & Astrophysics*, 492(1):277–287, December 2008. ISSN 0004-6361, 1432-0746. doi: 10.1051/0004-6361:200810395. URL <https://www.aanda.org/articles/aa/abs/2008/46/aa10395-08/aa10395-08.html>. Number: 1 Publisher: EDP Sciences.
- J.-L. Beuzit, A. Vigan, D. Mouillet, K. Dohlen, R. Gratton, A. Boccaletti, et al. SPHERE: the exoplanet imager for the Very Large Telescope. *Astronomy and Astrophysics*, 631: A155, November 2019. ISSN 0004-6361. doi: 10.1051/0004-6361/201935251. URL <http://adsabs.harvard.edu/abs/2019A%26A...631A.155B>.
- Jean-Luc Beuzit, Markus Feldt, Kjetil Dohlen, David Mouillet, Pascal Puget, Francois Wildi, et al. SPHERE: a planet finder instrument for the VLT. In *Ground-based and Airborne Instrumentation for Astronomy II*, volume 7014, page 701418. International Society for Optics and Photonics, July 2008. doi: 10.1117/12.790120. URL <https://www.spiedigitallibrary.org/conference-proceedings-of-spie/7014/701418/SPHERE-a-planet-finder-instrument-for-the-VLT/10.1117/12.790120.short>.
- A. J. Bohn, M. A. Kenworthy, C. Ginski, M. Benisty, J. de Boer, C. U. Keller, et al. Discovery of a directly imaged disk in scattered light around the Sco-Cen member Wray 15-788. *Astronomy & Astrophysics*, 624:A87, April 2019. ISSN 0004-6361, 1432-0746. doi: 10.1051/0004-6361/201834523. URL <http://arxiv.org/abs/1902.07723>. arXiv: 1902.07723.
- A. J. Bohn, M. A. Kenworthy, C. Ginski, C. F. Manara, M. J. Pecaut, J. de Boer, et al. The Young Suns Exoplanet Survey: Detection of a wide orbit planetary mass companion to a solar-type Sco-Cen member. *Monthly Notices of the Royal Astronomical Society*, 492(1): 431–443, February 2020. ISSN 0035-8711, 1365-2966. doi: 10.1093/mnras/stz3462. URL <http://arxiv.org/abs/1912.04284>. arXiv: 1912.04284.
- William J. Borucki. KEPLERMission: development and overview. *Reports on Progress in Physics*, 79(3):036901, February 2016. ISSN 0034-4885. doi: 10.1088/0034-4885/79/3/036901. URL <https://doi.org/10.1088%2F0034-4885%2F79%2F3%2F036901>.
- Brendan P. Bowler, Sarah C. Blunt, and Eric L. Nielsen. Population-level Eccentricity Distributions of Imaged Exoplanets and Brown Dwarf Companions: Dynamical Evidence for Distinct Formation Channels. *The Astronomical Journal*, 159:63, February 2020. ISSN 0004-6256. doi: 10.3847/1538-3881/ab5b11. URL <http://adsabs.harvard.edu/abs/2020AJ....159...63B>.
- A. Cassan, D. Kubas, J.-P. Beaulieu, M. Dominik, K. Horne, J. Greenhill, et al. One or more bound planets per Milky Way star from microlensing observations. *Nature*, 481 (7380):167–169, January 2012. ISSN 1476-4687. doi: 10.1038/nature10684. URL <https://www.nature.com/articles/nature10684>. Number: 7380 Publisher: Nature Publishing Group.
- G. Chauvin, A.-M. Lagrange, C. Dumas, B. Zuckerman, D. Mouillet, I. Song, et al. A giant planet candidate near a young brown dwarf - Direct VLT/NACO observations using IR wavefront sensing. *Astronomy & Astrophysics*, 425(2):L29–L32, October 2004. ISSN 0004-6361, 1432-0746. doi: 10.1051/0004-6361:200400056. URL <https://www.aanda.org/articles/aa/abs/2004/38/aagg222/aagg222.html>.

- G Chauvin, S Desidera, A Cheetham, M Bonnefoy, and M Meyer. SHINE, THE SPHERE INFRARED SURVEY FOR EXOPLANETS. page 5, 2017.
- Jeffrey Chilcote, Laurent Pueyo, Robert J. De Rosa, Jeffrey Vargas, Bruce Macintosh, Vanessa P. Bailey, et al. 1–2.4 μm Near-IR Spectrum of the Giant Planet β Pictoris b Obtained with the Gemini Planet Imager. *The Astronomical Journal*, 153(4):182, March 2017. ISSN 1538-3881. doi: 10.3847/1538-3881/aa63e9. URL <https://doi.org/10.3847/1538-3881/aa63e9>. Publisher: American Astronomical Society.
- R. U. Claudi, M. Turatto, J. Antichi, R. Gratton, S. Scuderi, E. Cascone, et al. The integral field spectrograph of SPHERE: the planet finder for VLT. page 62692Y, Orlando, Florida, USA, June 2006. doi: 10.1117/12.671949. URL <http://proceedings.spiedigitallibrary.org/proceeding.aspx?doi=10.1117/12.671949>.
- R. U. Claudi, M. Turatto, R. G. Gratton, J. Antichi, M. Bonavita, P. Bruno, et al. SPHERE IFS: the spectro differential imager of the VLT for exoplanets search. In *Ground-based and Airborne Instrumentation for Astronomy II*, volume 7014, page 70143E. International Society for Optics and Photonics, July 2008. doi: 10.1117/12.788366. URL <https://www.spiedigitallibrary.org/conference-proceedings-of-spie/7014/70143E/SPHERE-IFS--the-spectro-differential-imager-of-the-VLT/10.1117/12.788366.short>.
- Michael J. Crowe. A History of the Extraterrestrial Life Debate. *Zygon*[®], 32(2):147–162, 1997. ISSN 1467-9744. doi: 10.1111/0591-2385.801997079. URL <https://www.onlinelibrary.wiley.com/doi/abs/10.1111/0591-2385.801997079>.
- G. Cugno, S. P. Quanz, R. Launhardt, A. Musso Barcucci, S. S. Brems, A. Cheetham, et al. ISPY - the NaCo Imaging Survey for Planets around Young stars: A young companion candidate embedded in the R CrA cloud. *Astronomy & Astrophysics*, 624:A29, April 2019. ISSN 0004-6361, 1432-0746. doi: 10.1051/0004-6361/201935142. URL <http://arxiv.org/abs/1902.04092>. arXiv: 1902.04092.
- E. D. Feigelson, W. A. Lawson, M. Stark, L. Townsley, and G. P. Garmire. 51 Eridani and GJ 3305: A 10-15 Myr old Binary Star System at 30 Parsecs. *The Astronomical Journal*, 131(3):1730–1739, March 2006. ISSN 1538-3881. doi: 10.1086/499923. URL <https://doi.org/10.1086/499923>. Publisher: IOP Publishing.
- W. Freudling, M. Romaniello, D. M. Bramich, P. Ballester, V. Forchi, C. E. Garcia-Dablo, S. Moehler, and M. J. Neeser. Automated data reduction workflows for astronomy. *Astronomy & Astrophysics*, 559:A96, November 2013. ISSN 0004-6361, 1432-0746. doi: 10.1051/0004-6361/201322494. URL <http://arxiv.org/abs/1311.5411>. arXiv: 1311.5411.
- T. Fusco, C. Petit, G. Rousset, J.-F. Sauvage, K. Dohlen, D. Mouillet, et al. Design of the extreme AO system for SPHERE, the planet finder instrument of the VLT. page 62720K, Orlando, Florida, USA, June 2006. doi: 10.1117/12.670794. URL <http://proceedings.spiedigitallibrary.org/proceeding.aspx?doi=10.1117/12.670794>.
- Michaël Gillon, Emmanuël Jehin, Susan M. Lederer, Laetitia Delrez, Julien de Wit, Artem Burdanov, et al. Temperate Earth-sized planets transiting a nearby ultracool dwarf star. *Nature*, 533(7602):221–224, May 2016. ISSN 1476-4687. doi: 10.1038/nature17448. URL <https://www.nature.com/articles/nature17448>. Number: 7602 Publisher: Nature Publishing Group.
- Markus Janson, Wolfgang Brandner, Thomas Henning, Rainer Lenzen, Barbara McArthur, G. Fritz Benedict, et al. NACO-SDI Direct Imaging Search for the Exoplanet epsilon Eri

- b. *The Astronomical Journal*, 133(6):2442–2456, June 2007. ISSN 0004-6256, 1538-3881. doi: 10.1086/516632. URL <http://stacks.iop.org/1538-3881/133/i=6/a=2442>.
- M. Konacki, G. Torres, S. Jha, and D. Sasselov. A New Transiting Extrasolar Giant Planet. *arXiv Astrophysics e-prints*, pages arXiv:astro-ph/0301052, January 2003. URL <http://adsabs.harvard.edu/abs/2003astro.ph..1052K>.
- G. P. Kuiper. The Empirical Mass-Luminosity Relation. *The Astrophysical Journal*, 88:472, November 1938. ISSN 0004-637X. doi: 10.1086/143999. URL <http://adsabs.harvard.edu/abs/1938ApJ....88.472K>.
- B. Macintosh, J. R. Graham, T. Barman, R. J. De Rosa, Q. Konopacky, M. S. Marley, et al. Discovery and spectroscopy of the young jovian planet 51 Eri b with the Gemini Planet Imager. *Science*, 350(6256):64–67, October 2015. ISSN 0036-8075, 1095-9203. doi: 10.1126/science.aac5891. URL <https://science.sciencemag.org/content/350/6256/64>. Publisher: American Association for the Advancement of Science Section: Report.
- Nikku Madhusudhan. Atmospheric Retrieval of Exoplanets. *arXiv:1808.04824 [astro-ph]*, pages 2153–2182, 2018. doi: 10.1007/978-3-319-55333-7_104. URL <http://arxiv.org/abs/1808.04824>. arXiv: 1808.04824.
- Christian Marois, David Lafreniere, Rene Doyon, Bruce Macintosh, and Daniel Nadeau. Angular Differential Imaging: A Powerful High-Contrast Imaging Technique. *The Astrophysical Journal*, 641(1):556–564, April 2006. ISSN 0004-637X. doi: 10.1086/500401. URL <https://doi.org/10.1086%2F500401>.
- Christian Marois, Bruce Macintosh, Travis Barman, B. Zuckerman, Inseok Song, Jennifer Patience, et al. Direct Imaging of Multiple Planets Orbiting the Star HR 8799. *Science*, 322(5906):1348–1352, November 2008. ISSN 0036-8075, 1095-9203. doi: 10.1126/science.1166585. URL <https://science.sciencemag.org/content/322/5906/1348>. Publisher: American Association for the Advancement of Science Section: Research Article.
- Michel Mayor and Didier Queloz. A Jupiter-mass companion to a solar-type star. *Nature*, 378(6555):355–359, November 1995. ISSN 1476-4687. doi: 10.1038/378355a0. URL <https://www.nature.com/articles/378355a0>.
- Bertrand Mennesson, Scott Gaudi, Sara Seager, Kerri Cahoy, Shawn Domagal-Goldman, Lee Feinberg, et al. The Habitable Exoplanet (HabEx) Imaging Mission: preliminary science drivers and technical requirements. In *Space Telescopes and Instrumentation 2016: Optical, Infrared, and Millimeter Wave*, volume 9904, page 99040L. International Society for Optics and Photonics, August 2016. doi: 10.1117/12.2240457. URL <https://www.spiedigitallibrary.org/conference-proceedings-of-spie/9904/99040L/The-Habitable-Exoplanet-HabEx-Imaging-Mission--preliminary-science-drivers/10.1117/12.2240457.short>.
- Benoît Pairet, Faustine Cantalloube, Carlos A. Gomez Gonzalez, Olivier Absil, and Laurent Jacques. STIM map: detection map for exoplanets imaging beyond asymptotic Gaussian residual speckle noise. *Monthly Notices of the Royal Astronomical Society*, 487(2):2262–2277, August 2019. ISSN 0035-8711, 1365-2966. doi: 10.1093/mnras/stz1350. URL <http://arxiv.org/abs/1810.06895>. arXiv: 1810.06895.
- Mark J. Pecaut and Eric E. Mamajek. The Star-formation History and Accretion-Disk Fraction Among the K-Type Members of the Scorpius-Centaurus OB Association. *Monthly Notices of the Royal Astronomical Society*, 461(1):794–815, September 2016. ISSN 0035-8711, 1365-2966. doi: 10.1093/mnras/stw1300. URL <http://arxiv.org/abs/1605.08789>. arXiv: 1605.08789.

- Fabian Pedregosa, Gaël Varoquaux, Alexandre Gramfort, Vincent Michel, Bertrand Thirion, Olivier Grisel, et al. Scikit-learn: Machine Learning in Python. *Journal of Machine Learning Research*, 12:2825, October 2011. ISSN 1533-7928. URL <http://jmlr.csail.mit.edu/papers/v12/pedregosa11a.html>.
- C. Petit, J.-F. Sauvage, T. Fusco, A. Sevin, M. Suarez, A. Costille, et al. SPHERE extreme AO control scheme: final performance assessment and on sky validation of the first auto-tuned LQG based operational system. page 91480O, Montréal, Quebec, Canada, August 2014. doi: 10.1117/12.2052847. URL <http://proceedings.spiedigitallibrary.org/proceeding.aspx?doi=10.1117/12.2052847>.
- L. Pueyo, R. Soummer, J. Hoffmann, R. Oppenheimer, J. R. Graham, N. Zimmerman, et al. Reconnaissance of the HR 8799 Exosolar System. II. Astrometry and Orbital Motion. *The Astrophysical Journal*, 803:31, April 2015. ISSN 0004-637X. doi: 10.1088/0004-637X/803/1/31. URL <http://adsabs.harvard.edu/abs/2015ApJ...803...31P>.
- Robert J. De Rosa, Eric L. Nielsen, Sarah C. Blunt, James R. Graham, Quinn M. Konopacky, Christian Marois, et al. ASTROMETRIC CONFIRMATION AND PRELIMINARY ORBITAL PARAMETERS OF THE YOUNG EXOPLANET 51 ERIDANI b WITH THE GEMINI PLANET IMAGER. *The Astrophysical Journal*, 814(1):L3, November 2015. ISSN 2041-8213. doi: 10.1088/2041-8205/814/1/L3. URL <https://iopscience.iop.org/article/10.1088/2041-8205/814/1/L3>.
- Jean-Baptiste Ruffio, Bruce Macintosh, Jason J. Wang, Laurent Pueyo, Eric L. Nielsen, Robert J. De Rosa, et al. Improving and Assessing Planet Sensitivity of the GPI Exoplanet Survey with a Forward Model Matched Filter. *The Astrophysical Journal*, 842(1):14, June 2017. ISSN 0004-637X. doi: 10.3847/1538-4357/aa72dd. URL <https://doi.org/10.3847/2F1538-4357%2Faa72dd>. Publisher: American Astronomical Society.
- M. Samland, P. Mollière, M. Bonnefoy, A.-L. Maire, F. Cantalloube, A. C. Cheetham, et al. Spectral and atmospheric characterization of 51 Eridani b using VLT/SPHERE. *Astronomy & Astrophysics*, 603:A57, July 2017. ISSN 0004-6361, 1432-0746. doi: 10.1051/0004-6361/201629767. URL <http://www.aanda.org/10.1051/0004-6361/201629767>.
- Jean Schneider. The question “Are we alone ?” in different cultures. *Proceedings of the International Astronomical Union*, 5(S260):213–217, January 2009. ISSN 1743-9213, 1743-9221. doi: 10.1017/S1743921311002316. URL https://www.cambridge.org/core/product/identifier/S1743921311002316/type/journal_article.
- S. Seager. Exoplanet Transit Spectroscopy and Photometry. *Space Science Reviews*, 135(1):345–354, March 2008. ISSN 1572-9672. doi: 10.1007/s11214-008-9308-5. URL <https://doi.org/10.1007/s11214-008-9308-5>.
- Sara Seager. *Exoplanets*. University of Arizona Press, 2010. ISBN 978-0-8165-2945-2. Google-Books-ID: VLSVmxgPgGYC.
- Daniel G. Smith. *Field Guide to Physical Optics*. SPIE, April 2013. ISBN 978-0-8194-8549-6. doi: 10.1117/3.883971. URL <https://spiedigitallibrary.org/ebooks/FG/Field-Guide-to-Physical-Optics/eISBN-9780819485496/10.1117/3.883971>.
- Keivan G. Stassun, Kaitlin M. Kratter, Aleks Scholz, and Trent J. Dupuy. AN EMPIRICAL CORRECTION FOR ACTIVITY EFFECTS ON THE TEMPERATURES, RADII, AND ESTIMATED MASSES OF LOW-MASS STARS AND BROWN DWARFS. *The Astrophysical Journal*, 756(1):47, August 2012. ISSN 0004-637X. doi: 10.1088/0004-637X/756/1/47. URL <https://doi.org/10.1088%2F0004-637x%2F756%2F1%2F47>. Publisher: IOP Publishing.

-
- T. Stolker, M. J. Bonse, S. P. Quanz, A. Amara, G. Cugno, A. J. Bohn, and A. Boehle. PynPoint: a modular pipeline architecture for processing and analysis of high-contrast imaging data. *Astronomy and Astrophysics*, 621:A59, January 2019. ISSN 0004-6361. doi: 10.1051/0004-6361/201834136. URL <http://adsabs.harvard.edu/abs/2019A%26A...621A..59S>.
- Z Wahhaj, J Milli, F Rodler, J Girard, and A Vigan. SPHERE - User Manual. September 2019.
- Jason J. Wang, James R. Graham, Laurent Pueyo, Paul Kalas, Maxwell A. Millar-Blanchaer, Jean-Baptiste Ruffio, et al. THE ORBIT AND TRANSIT PROSPECTS FOR β PICTORIS b CONSTRAINED WITH ONE MILLIARCSECOND ASTROMETRY. *The Astronomical Journal*, 152(4):97, October 2016. ISSN 1538-3881. doi: 10.3847/0004-6256/152/4/97. URL <https://doi.org/10.3847%2F0004-6256%2F152%2F4%2F97>. Publisher: American Astronomical Society.
- D. C. B. Whittet. *Dust in the Galactic Environment, 2nd Edition*. CRC Press, October 2002. ISBN 978-0-7503-0624-9. Google-Books-ID: k21lk4sORpEC.
- M.J. Wilby. Painting with starlight : optical techniques for the high-contrast imaging of exoplanets, November 2018. URL <https://openaccess.leidenuniv.nl/handle/1887/67531>.
- A. Zurlo, A. Vigan, R. Galicher, A.-L. Maire, D. Mesa, R. Gratton, et al. First light of the VLT planet finder SPHERE - III. New spectrophotometry and astrometry of the HR 8799 exoplanetary system. *Astronomy & Astrophysics*, 587:A57, March 2016. ISSN 0004-6361, 1432-0746. doi: 10.1051/0004-6361/201526835. URL <https://www.aanda.org/articles/aa/abs/2016/03/aa26835-15/aa26835-15.html>. Publisher: EDP Sciences.

Chapter A

Additional Graphs

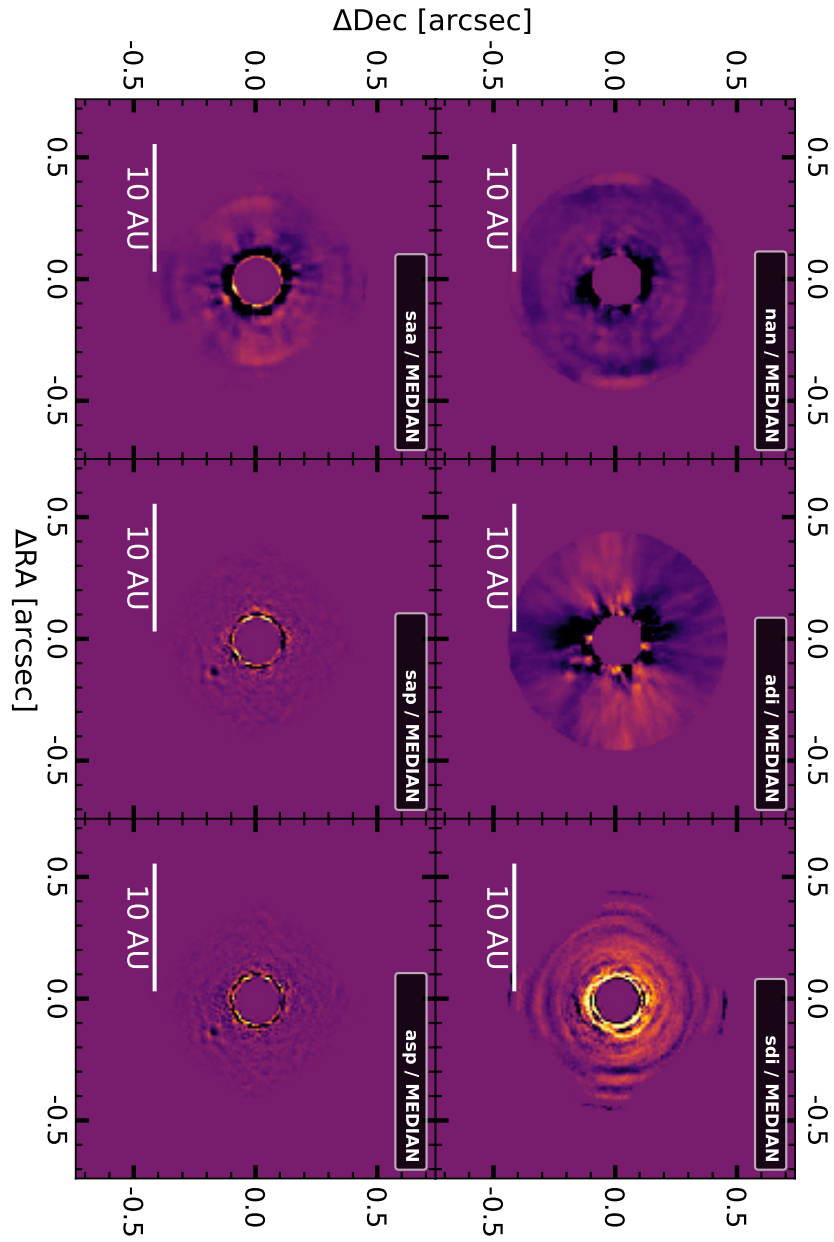


Figure 37: Reduced images of a subset of Beta Pictoris containing 132 images over an angular range of 37.6° (PI: J. Beuzit) using different advanced differential imaging techniques. All images were produced using the number of principal components resulting in the highest SNR of Beta Pictoris b according to chapter 4.2 (0 for NAN; 18 for ADI; 4 for SDI; 8 for SAA; 4 for SAP; 6 for ASP). The differential imaging techniques are explained in chapter 2.4. The colour-bar of each image is set arbitrary and brighter colours represent higher values.

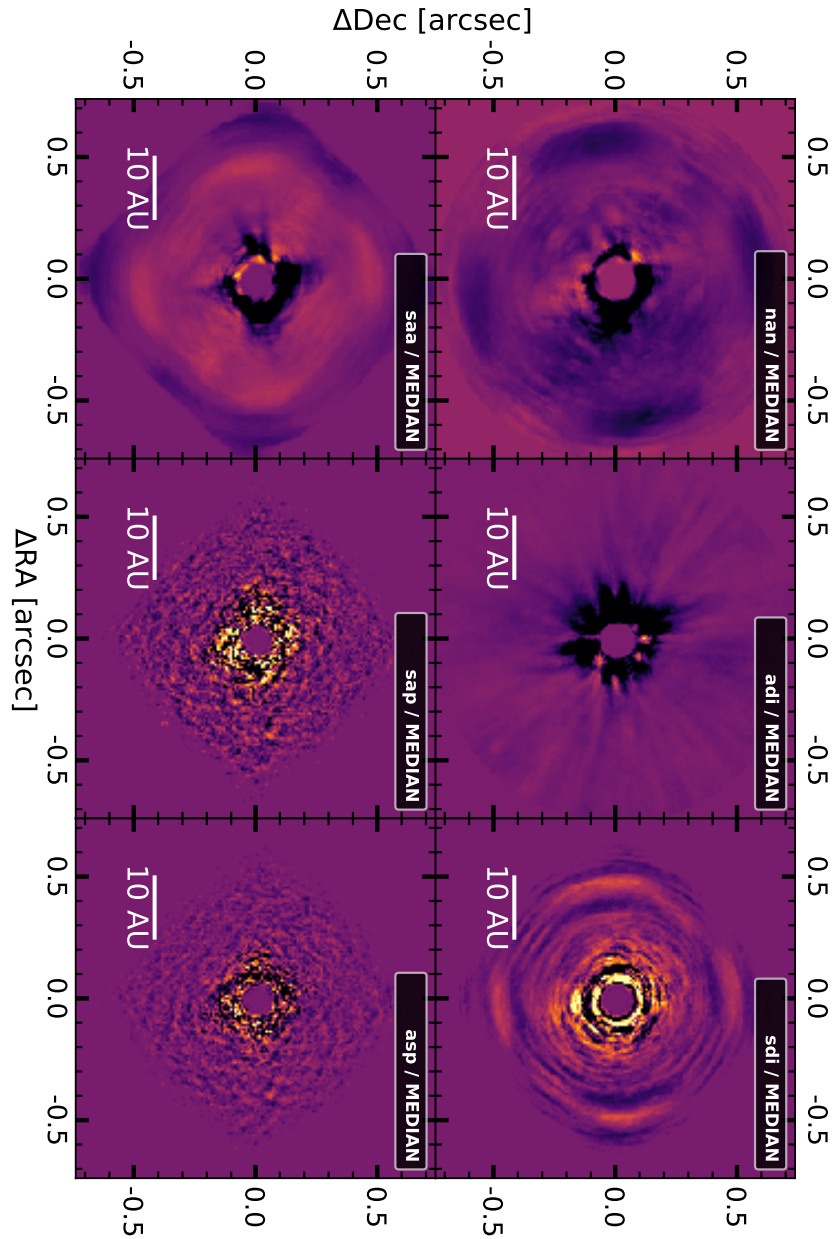


Figure 38: Reduced images of HR 8799 (PI: J. Beuzit) using different advanced differential imaging techniques. All images were produced using the number of principal components resulting in the highest SNR of HR 8799 e according to chapter 4.2 (0 for NAN; 2 for ADI, SDI, SAA; 4 for SAP, ASP). The differential imaging techniques are explained in chapter 2.4. The colour-bar of each image is set arbitrary and brighter colours represent higher values.

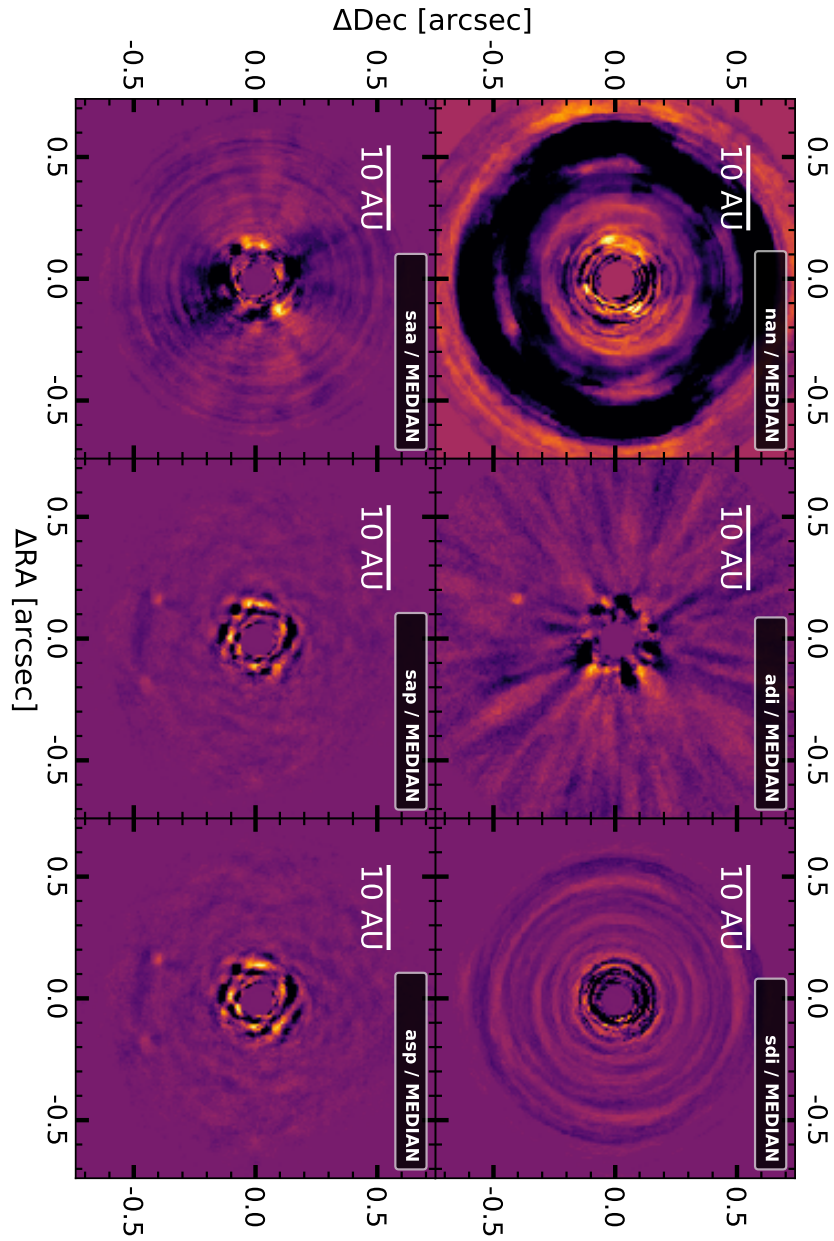
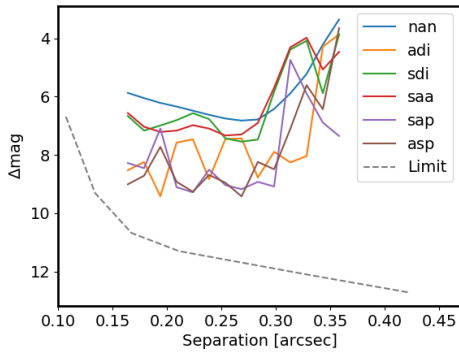
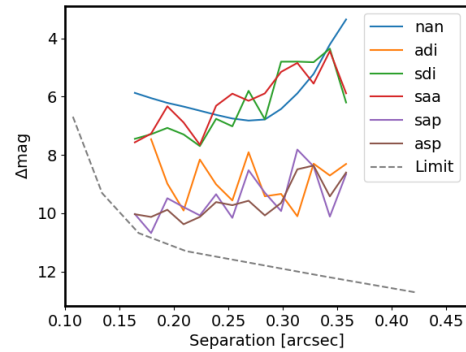


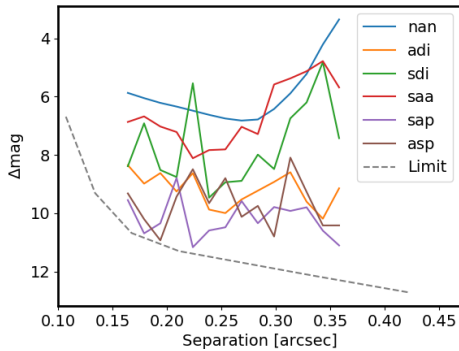
Figure 39: Reduced images of 51 Eridani (PI: J. Beuzit) using different advanced differential imaging techniques. All images were produced using the number of principal components resulting in the highest SNR of 51 Eridani b according to chapter 4.2 (0 for NAN; 12 for ADI; 8 for SDI; 4 for SAA; 12 for SAP; 10 for ASP). The differential imaging techniques are explained in chapter 2.4. The colour-bar of each image is set arbitrary and brighter colours represent higher values.



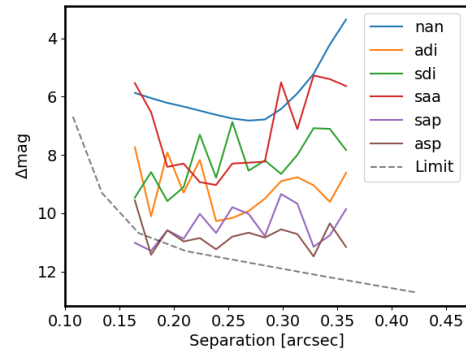
(a) 2 principal components



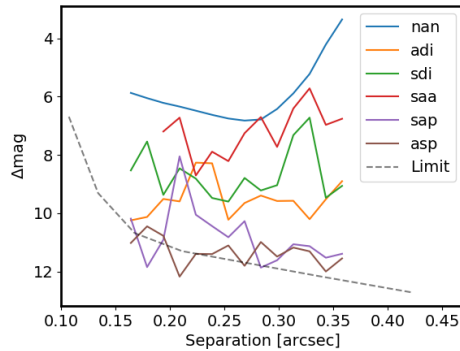
(b) 6 principal components



(c) 10 principal components

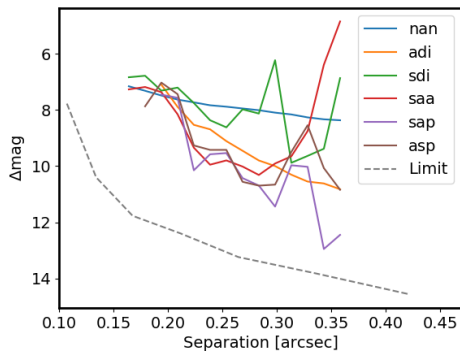


(d) 14 principal components

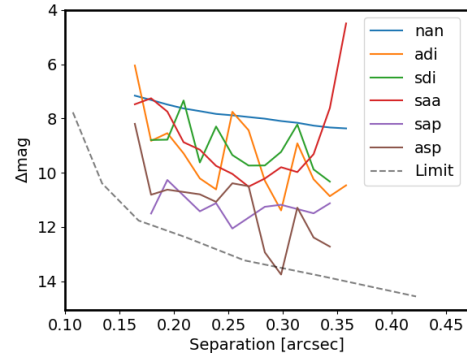


(e) 18 principal components

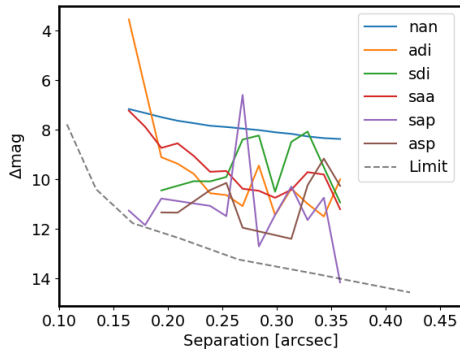
Figure 40: Additional contrast curves of Ob1 (Target: 2MASS J 11555771-5254008; PI: A.J. Bohn) including a companion candidate at $SEP = 0.371 \pm 0.003$ arcsec, $PA = 16.8 \pm 0.4^\circ$. The contrast curves show the 5σ detection limits for further companions. The Limit curve was calculated using the SPHERE/IFS exposure time calculator available at <https://www.eso.org/observing/etc/bin/gen/form?INS.NAME=SPHERE+INS.MODE=IFS>. The differential imaging techniques are explained in chapter 2.4



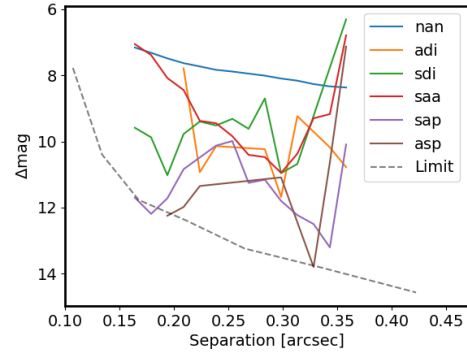
(a) 2 principal components



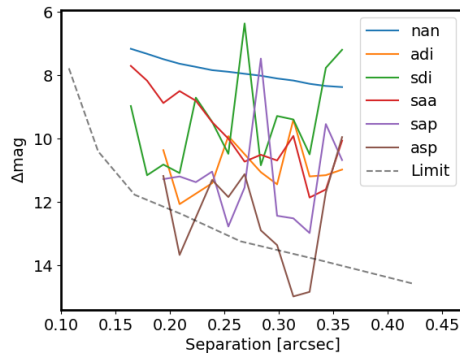
(b) 6 principal components



(c) 10 principal components

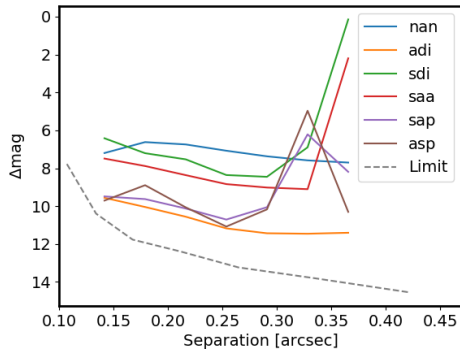


(d) 14 principal components

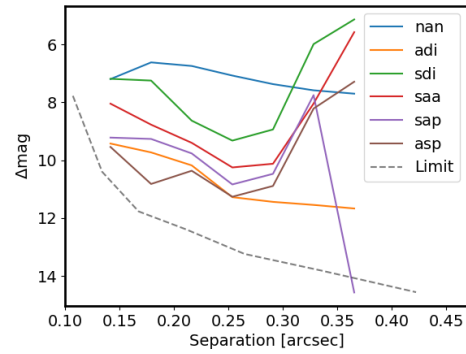


(e) 18 principal components

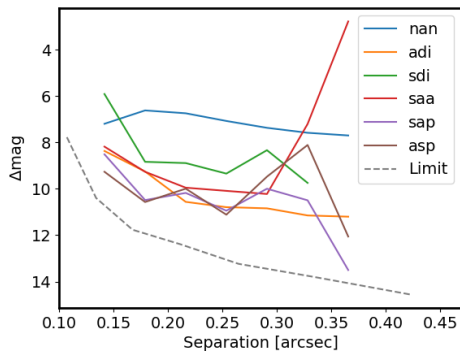
Figure 41: Additional contrast curves of Ob2 (Target: 2MASS J 13381128-5214251; PI: A.J. Bohn) including a companion candidate at $SEP = 0.151 \pm 0.007$ arcsec, $PA = 166 \pm 3^\circ$. The contrast curves show the 5σ detection limits for further companions. The 'Limit' curve was calculated using the SPHERE/IFS exposure time calculator available at <https://www.eso.org/observing/etc/bin/gen/form?INS.NAME=SPHERE+INS.MODE=IFS>. The differential imaging techniques are explained in chapter 2.4



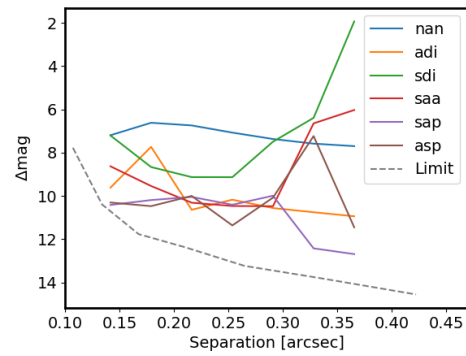
(a) 2 principal components



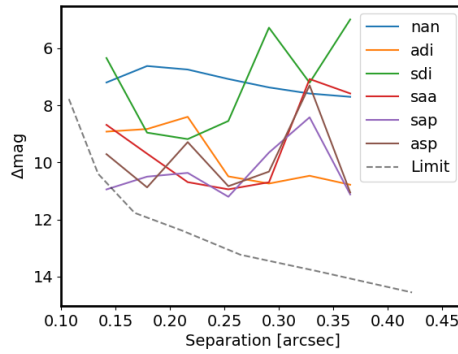
(b) 6 principal components



(c) 10 principal components

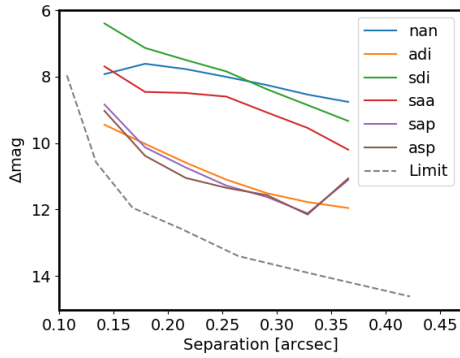


(d) 14 principal components

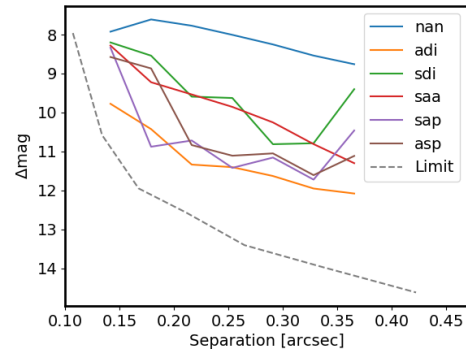


(e) 18 principal components

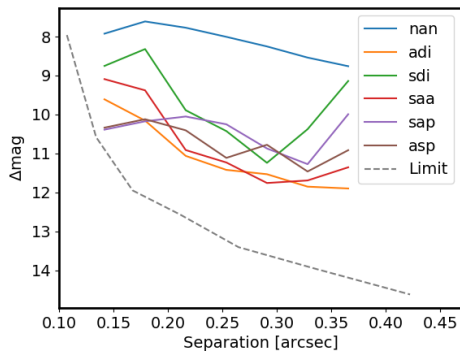
Figure 42: Additional contrast curves of Ob3 (Target: 2MASS J 12123577-5520273; PI: A.J. Bohn). The contrast curves show the 5σ detection limits for further companions. The 'Limit' curve was calculated using the SPHERE/IFS exposure time calculator available at <https://www.eso.org/observing/etc/bin/gen/form?INS.NAME=SPHERE+INS.MODE=IFS>. The differential imaging techniques are explained in chapter 2.4



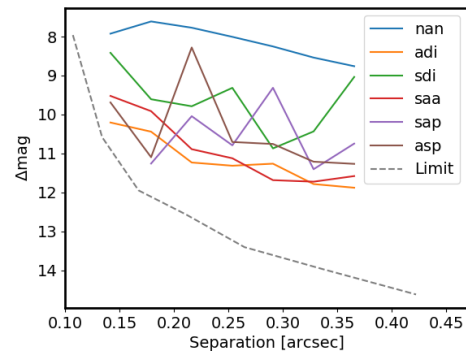
(a) 2 principal components



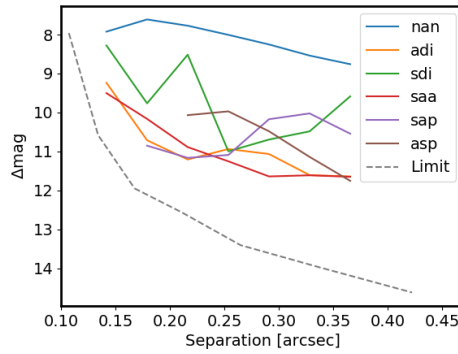
(b) 6 principal components



(c) 10 principal components



(d) 14 principal components



(e) 18 principal components

Figure 43: Additional contrast curves of Ob5 (Target: 2MASS J 13233587-4718467; PI: A.J. Bohn). The contrast curves show the 5σ detection limits for further companions. The 'Limit' curve was calculated using the SPHERE/IFS exposure time calculator available at <https://www.eso.org/observing/etc/bin/gen/form?INS.NAME=SPHERE+INS.MODE=IFS>. The differential imaging techniques are explained in chapter 2.4

Python Code

Pypelines

```
1 import os
2 import numpy as np
3 import pynpoint as pp
4
5 # ===== Input Variables
6 # Directories for the input images
7 path_working = "./working"
8 path_in = "./in"
9 path_out = "./out"
10
11 path_lam = "./in/lam"
12 path_science = './in/reduced'
13 path_center = './in/center'
14 path_dark = './in/dark'
15 path_flat = './in/flat'
16 path_flux = './in/flux'
17 path_star_spectra = './working/stellar_model.txt'
18
19 # crop size of the flux images [px]
20 fl_size = 80
21
22 # neutral density filter of the flux images
23 flux_filter = 'ND_1.0'
24
25 # crop size of the science images [px]
26 im_size = 280
27
28 # rough position of the star in the flux images [px, px]
29 star_pos = [187, 203]
30
31 # rough position of the companion [px, px]
32 plan_pos = [80, 34]
33
34 # max separation of the contrast curve [px]
35 r_max = 50
36
```

```

37 # radial resolution of the contrast curve [px]
38 r_res = 5
39
40 # angular resolution of the contrast curve [degree]
41 a_res = 120
42
43 # processing type
44 p_type = 'Tasp'
45 pca_nr = np.arange(1,15)
46
47
48 # ===== Pipeline Setup
49 # --- SPHERE/IFS parameters
50 # inner working angle [arcsec]
51 iwa = 0.1
52
53 # conversion factor: pixel to arcsecond [arcsec/px]
54 pixscale = 0.00746
55
56 # smallest separation of waffle spots [px]
57 ce_r_min = 47
58
59 # smallest wavelength [micron]
60 ce_l_min = 0.953
61
62 # angular offset of the waffle spots [degree]
63 ce_angle = 55
64
65 # extra rotation of the observation [degree]
66 im_extra_rot = 0.
67
68 # dictionaries for the moduels executed within the IFSsupport Function
69 mods = []
70
71 # Create Working directory for this target
72 if not os.path.isdir(path_working):
73     print("Creating directory: %s" % (path_working))
74     os.makedirs(path_working)
75
76 # Create directory for results
77 if not os.path.isdir(path_out):
78     print("Creating directory: %s" % (path_out))
79     os.makedirs(path_out)
80
81 # Set up Pipeline
82 pipeline = pp.Pypeline(working_place_in = path_working,
83                        input_place_in = path_in,
84                        output_place_in = path_out)
85
86
87 # ===== Pipeline 1
88 # --- read in of science, flux and centring images
89 im_reading_mod = pp.FitsReadingModule(name_in = "im_reading_mod",
90                                       input_dir = path_science,
91                                       image_tag = "im")
92

```

```

93 ce_reading_mod = pp.FitsReadingModule(name_in = "ce_reading_mod",
94                                     input_dir = path_center,
95                                     image_tag = "ce")
96
97 fl_reading_mod = pp.FitsReadingModule(name_in = "fl_reading_mod",
98                                     input_dir = path_flux,
99                                     image_tag = "fl")
100
101 # --- bad pixel cleaning of science, flux and centring images
102 im_badpixel_dict = {'module': 'BadPixelSigmaFilterModule',
103                   'name_in': "im_badpixel_dict",
104                   'image_in_tag': 'im',
105                   'image_out_tag': 'im_bp',
106                   'box': 11,
107                   'sigma': 5.,
108                   'iterate': 5}
109
110 ce_badpixel_dict = {'module': 'BadPixelSigmaFilterModule',
111                   'name_in': "ce_badpixel_dict",
112                   'image_in_tag': 'ce',
113                   'image_out_tag': 'ce_bp',
114                   'box': 11,
115                   'sigma': 5.,
116                   'iterate': 5}
117
118 fl_badpixel_dict = {'module': 'BadPixelSigmaFilterModule',
119                   'name_in': "fl_badpixel_dict",
120                   'image_in_tag': 'fl',
121                   'image_out_tag': 'fl_bp',
122                   'box': 11,
123                   'sigma': 5.,
124                   'iterate': 5}
125
126 # --- Scaling correction of science, flux and centring images
127 im_ifss_dict = {'module': 'IfsScalingModule',
128               'name_in': 'im_ifss_dict',
129               'image_in_tag': 'im_bp',
130               'image_out_tag': 'im_sc',
131               'scaling': (1.0, 1.0011, 1.0),
132               'angle': 50.,
133               'pixscale': True}
134
135 ce_ifss_dict = {'module': 'IfsScalingModule',
136               'name_in': 'ce_ifss_dict',
137               'image_in_tag': 'ce_bp',
138               'image_out_tag': 'ce_sc',
139               'scaling': (1.0, 1.0011, 1.0),
140               'angle': 50.,
141               'pixscale': True}
142
143 fl_ifss_dict = {'module': 'IfsScalingModule',
144               'name_in': 'fl_ifss_dict',
145               'image_in_tag': 'fl_bp',
146               'image_out_tag': 'fl_sc',
147               'scaling': (1.0, 1.0011, 1.0),
148               'angle': 50.,

```



```

149         'pixscale': True}
150
151 # --- Angular calculation of science, flux and centring images
152 im_ac_dict = {'module': 'AngleCalculationModule',
153              'name_in': 'im_ac_dict',
154              'data_tag': 'im_sc',
155              'instrument': 'SPHERE/IFS'}
156
157 ce_ac_dict = {'module': 'AngleCalculationModule',
158              'name_in': 'ce_sc_dict',
159              'data_tag': 'ce_sc',
160              'instrument': 'SPHERE/IFS'}
161
162 fl_ac_dict = {'module': 'AngleCalculationModule',
163              'name_in': 'fl_sc_dict',
164              'data_tag': 'fl_sc',
165              'instrument': 'SPHERE/IFS'}
166
167 # --- Waffel centring of science images
168 im_bwc_dict = {'module': 'WaffleCenteringModule',
169               'name_in': 'im_bwc_dict',
170               'image_in_tag': 'im_sc',
171               'center_in_tag': 'ce_sc',
172               'image_out_tag': 'im_bw',
173               'radius': ce_r_min,
174               'l_min': ce_l_min,
175               'size': None,
176               'center': None,
177               'angle': ce_angle,
178               'sigma': 10.*pixscale,
179               'dither': False}
180
181 # --- Sort for paralactic angle
182 im_sort_dict = {'module': 'SortParangModule',
183                'name_in': 'im_sort_dict',
184                'image_in_tag': 'im_bw',
185                'image_out_tag': 'im_fc'}
186
187 # --- Print final cut, derotated
188 im_derotstack_dict = {'module': 'DerotateAndStackModule',
189                       'name_in': 'im_derotstack_dict',
190                       'image_in_tag': 'im_bw',
191                       'image_out_tag': 'fc_check',
192                       'derotate': True,
193                       'stack': None,
194                       'extra_rot': 0}
195
196 # --- Crop images
197 im_crop_dict = {'module': 'CropImagesModule',
198                'name_in': "im_crop_dict",
199                'image_in_tag': 'im_fc',
200                'image_out_tag': 'im_crop',
201                'size': im_size*pixscale,
202                'center': None}
203
204

```

```

205 # ===== Pipeline 2
206 # --- extract the star
207 fl_starextract_dict = {'module': 'StarExtractionModule',
208                       'name_in': "fl_starextract_mod",
209                       'image_in_tag': "fl_sc",
210                       'image_out_tag': "fl_extract",
211                       'image_size': fl_size*pixscale,
212                       'fwhm_star': 0.1,
213                       'position': (star_pos[0], star_pos[1], 0.15)}
214
215 # --- aligne all flux frames
216 fl_align_dict = {'module': 'StarAlignmentModule',
217                'name_in': "fl_align_dict",
218                'image_in_tag': "fl_extract",
219                'image_out_tag': "fl_aligned",
220                'ref_image_in_tag': None,
221                'interpolation': "spline",
222                'accuracy': 10,
223                'resize': None,
224                'num_references': 1,
225                'subframe': 41*pixscale}
226
227 # --- calculate offset of the star within the flux images
228 fl_centercalc_dict = {'module': 'FitCenterModule',
229                      'name_in': "fl_centercalc_dict",
230                      'image_in_tag': "fl_aligned",
231                      'fit_out_tag': "center_fit",
232                      'method': "full",
233                      'radius': 20*pixscale,
234                      'sign': "positive",
235                      'model': "gaussian",
236                      'filter_size': None}
237
238 # --- center the star within the flux images
239 fl_centershift_dict = {'module': 'ShiftImagesModule',
240                       'name_in': "fl_centershift_dict",
241                       'image_in_tag': "fl_aligned",
242                       'image_out_tag': "fl_centerfit",
243                       'shift_xy': "center_fit",
244                       'interpolation': "spline"}
245
246 # --- Sort flux images for paralactic angle
247 fl_sort_dict = {'module': 'SortParangModule',
248               'name_in': 'fl_sort_dict',
249               'image_in_tag': 'fl_centerfit',
250               'image_out_tag': 'fl_fc'}
251
252 # --- Flux images for quality control
253 fl_derotmedian_dict = {'module': 'DerotateAndStackModule',
254                       'name_in': "fl_derotmedian_dict",
255                       'image_in_tag': "fl_fc",
256                       'image_out_tag': "fl_check",
257                       'derotate': True,
258                       'stack': "median",
259                       'extra_rot': 0.}
260

```

```

261 # --- calculate the average of the flux images per wavelength
262 fl_median_dict = {'module': 'DerotateAndStackModule',
263                  'name_in': "fl_median_dict",
264                  'image_in_tag': "fl_crop",
265                  'image_out_tag': "fl_median",
266                  'derotate': False,
267                  'stack': "median",
268                  'extra_rot': im_extra_rot}
269
270 # --- crop images to output size
271 fl_cropres_dict = {'module': 'CropImagesModule',
272                   'name_in': "fl_cropres_dict",
273                   'image_in_tag': "fl_median",
274                   'image_out_tag': "fl_cp",
275                   'size': fl_size*pixscale,
276                   'center': None}
277
278
279 # ===== Pipeline 3
280 # --- Perform pca reduction
281 pca_mod = pp.PcaPsfSubtractionModule(name_in = 'pca_psf_subtraction',
282                                     images_in_tag = 'WEOUT_im_crop',
283                                     reference_in_tag = 'WEOUT_fl_cp',
284                                     res_mean_tag = 'res_mean',
285                                     res_median_tag = 'res_median',
286                                     res_weighted_tag = None,
287                                     dmp_stim_tag = 'dmp_stim',
288                                     res_rot_mean_clip_tag = None,
289                                     res_arr_out_tag = None,
290                                     basis_out_tag = None,
291                                     pca_numbers = pca_nr,
292                                     extra_rot = im_extra_rot,
293                                     subtract_mean = True,
294                                     processing_type = p_type)
295
296 # --- write PCA results
297 median_mod = pp.FitsWritingModule(name_in = "median_write_mod",
298                                  file_name= "median_residuals.fits",
299                                  data_tag = "res_median")
300
301 mean_mod = pp.FitsWritingModule(name_in = "mean_write_mod",
302                                 file_name = "mean_residuals.fits",
303                                 data_tag = "res_mean")
304
305 stim_mod = pp.FitsWritingModule(name_in = "stim_write_mod",
306                                 file_name = "stim_detectionmap.fits",
307                                 data_tag = "dmp_stim")
308
309
310 # ===== Pipeline 4
311 # --- Derotate and stack science images for each wavelength
312 im_photo_derotstack_dict = {'module': 'DerotateAndStackModule',
313                              'name_in': 'im_photo_derotstack_dict',
314                              'image_in_tag': 'im_crop',
315                              'image_out_tag': 'im_prep',
316                              'derotate': True,

```

```

317         'stack': 'median',
318         'extra_rot': 0}
319
320 # --- calculate the contrast of companion to host star
321 im_aperture_photo_dict = {'module': 'SdiAperturePhotometryModule',
322                            'name_in': 'im_aperture_photo_dict',
323                            'image_in_tag': 'im_prep',
324                            'psf_in_tag': 'fl_cp',
325                            'flux_position_tag': 'ap_flux',
326                            'rough_position': plan_pos,
327                            'psf_scaling': None,
328                            'flux_filter': flux_filter,
329                            'cutout_size': 21,
330                            'fit_each_image': False,
331                            'aperture_size': 21*pixscale}
332
333 # --- calculate the companions spectra and use model based rejection
334 spec_ap_mod = pp.SpectralCharModule(name_in = 'spec_aperture_mod',
335                                    image_in_tag = 'WEOUT_ap_flux',
336                                    method = 'aperture',
337                                    stellar_model = path_star_spectra,
338                                    prop_factor = 7.496 * 10**(-20),
339                                    mol_fit = 'full',
340                                    output_dir = path_out)
341
342
343 # ===== Pyepline 5
344 # --- calculate the contrast of the companion
345 simp_sm_mod = pp.SdiSimplexMinimizationModule(name_in = 'spec_sm_mod',
346                                                image_in_tag = 'im_prep',
347                                                psf_in_tag = 'WEOUT_fl_cp',
348                                                res_out_tag = 'res_simplex',
349                                                flux_position_tag = 'sm_flux',
350                                                position = plan_pos,
351                                                magnitude = 10,
352                                                psf_scaling = None,
353                                                flux_filter = flux_filter,
354                                                merit = 'hessian',
355                                                aperture = 5*pixscale,
356                                                sigma = pixscale,
357                                                tolerance = 0.1,
358                                                pca_number = pca_nr[-1],
359                                                cent_size = iwa*pixscale,
360                                                edge_size = None,
361                                                extra_rot = 0.,
362                                                residuals = 'median',
363                                                processing_type = p_type)
364
365 # --- calculate the companions spectra and use model based rejection
366 spec_sm_mod = pp.SpectralCharModule(name_in = 'spec_aperture_mod',
367                                    image_in_tag = 'sm_flux',
368                                    method = 'simplex',
369                                    stellar_model = path_star_spectra,
370                                    prop_factor = 1.072e-18,
371                                    error_simplex = 0.1,
372                                    mol_fit = 'full',

```

```

373         output_dir = path_out)
374
375
376 # ===== Pipeline 6
377 # --- contrast calculation
378 ccurve_mod = pp.ContrastCurveModule(name_in = 'ccurve_mod',
379                                     image_in_tag = 'WEOUT_im_crop',
380                                     psf_in_tag = 'WEOUT_fl_cp',
381                                     contrast_out_tag = 'ccurve_out',
382                                     separation = (iwa*pixscale,
383                                                 r_max*pixscale,
384                                                 r_res*pixscale),
385                                     angle = (0.0, 360.0, a_res),
386                                     threshold = ('sigma', 5.0),
387                                     psf_scaling = None,
388                                     flux_filter = flux_filter,
389                                     aperture = 2*pixscale,
390                                     pca_number = pca_nr[-1],
391                                     cent_size = iwa*pixscale,
392                                     edge_size = None,
393                                     extra_rot = im_extra_rot,
394                                     residuals = 'median',
395                                     snr_inject = 100.0,
396                                     processing_type = p_type)
397
398 # --- plot contrast curve
399 plot_cc_mod = pp.PlotContrastCurveModule(name_in = 'plot_cc_mod',
400                                           image_in_tag = 'ccurve_out',
401                                           data_index = 4,
402                                           file_name = 'ccurve.png',
403                                           output_dir = path_out)
404
405
406 # ===== Append all modules to the Pipeline
407 # --- Pyepline 1
408 pipeline.add_module(im_reading_mod)
409 pipeline.add_module(ce_reading_mod)
410 pipeline.add_module(fl_reading_mod)
411 mods.append(im_badpixel_dict)
412 mods.append(ce_badpixel_dict)
413 mods.append(fl_badpixel_dict)
414 mods.append(im_ifss_dict)
415 mods.append(ce_ifss_dict)
416 mods.append(fl_ifss_dict)
417 mods.append(im_ac_dict)
418 mods.append(ce_ac_dict)
419 mods.append(fl_ac_dict)
420 mods.append(im_bwc_dict)
421 mods.append(im_sort_dict)
422 mods.append(im_derotstack_dict)
423 mods.append(im_crop_dict)
424
425 # --- Pypeline 2
426 mods.append(fl_starextract_dict)
427 mods.append(fl_align_dict)
428 mods.append(fl_centercalc_dict)

```

```

429 mods.append(fl_centershift_dict)
430 mods.append(fl_sort_dict)
431 mods.append(fl_derotmedian_dict)
432 mods.append(fl_median_dict)
433 mods.append(fl_cropres_dict)
434
435 # --- Pypeline 4 (part 1)
436 mods.append(im_photo_derotstack_dict)
437 mods.append(im_aperture_photo_dict)
438
439 # Execute IFS support function to add all modules to the pipeline
440 pp.IFSsupportModule(image_in_tag = ['im', 'ce', 'fl'],
441                    image_out_tag = ['im_crop', 'fl_cp'],
442                    pipe=pipeline,
443                    mod_args = mods,
444                    path_lam = path_lam,
445                    skip_split = False,
446                    print_out = True,
447                    split_argument = 'LAMBDA')
448
449 # --- Pypeline 3
450 pipeline.add_module(pca_mod)
451 pipeline.add_module(median_mod)
452 pipeline.add_module(mean_mod)
453 pipeline.add_module(stim_mod)
454
455 # --- Pypeline 4 (part 2)
456 pipeline.add_module(spec_ap_mod)
457
458 # --- Pypeline 5
459 pipeline.add_module(simp_sm_mod)
460 pipeline.add_module(spec_sm_mod)
461
462 # --- Pypeline 6
463 pipeline.add_module(ccurve_mod)
464 pipeline.add_module(plot_cc_mod)
465
466 # --- Run the Pyepline
467 pipeline.run()

```

Listing 1: Pipelines 1 to 6 as described in chapter 3.7.

SNR and Astrometry Calculation

```

1 # -*- coding: utf-8 -*-
2 __author__ = "Alexander Bohn, Sven Kiefer"
3
4 import numpy as np
5 import matplotlib.pyplot as plt

```

```

6 import photutils as pu
7
8 from astropy.table import Table
9 from photutils.aperture import CircularAperture
10 from scipy.special import erf
11 from astropy.modeling import fitting, models
12 from astropy.nddata import Cutout2D
13 from astropy.stats import sigma_clip
14
15
16 def get_false_alarm_probability(image_in: str,
17                               rough_pos: tuple,
18                               aperture_radius: float,
19                               method: str = 'exact',
20                               skip_closest_apertures: bool = False,
21                               plot: bool = False) -> Table:
22
23     """
24     Function to create a 2D elliptical Gaussian model.
25
26     Parameters
27     -----
28     image_in : str
29         Tag of the database entry with images that are read as input.
30     rough_pos : tuple
31         Approximate position of the companion (pix, pix).
32     aperture_radius : float
33         Radius of the aperture to calculate the SNR
34     method : str
35         Method to extract the centre of the companion
36     skip_closest_apertures : bool
37         Skipes reference apertures next to the signal aperture as
38         they could be influenced by the companions signal
39     plot : bool
40         If true, quality control plots are printed.
41
42     Returns
43     -----
44     Table
45         Table with the calculated statistics.
46
47     """
48
49
50     # Get image shape
51     im_shape = image_in.shape
52
53     # Perform Gaussian fit, if required
54     if method=="fit":
55
56         # Cut image at pos to resolution of 5 fwhm for Gaussian fit
57         im_cut = Cutout2D(data=image_in,
58                           position=rough_pos,
59                           size=(4 * aperture_radius,
60                                4 * aperture_radius),
61                           mode="partial",

```

```

62         fill_value=0.).data
63
64     # Fit the source in the science image using a 2D Gaussian
65     g_i = models.Gaussian2D(amplitude=im_cut[im_cut.shape[0] / 2,
66                               im_cut.shape[1] / 2],
67                              x_mean=im_cut.shape[0] / 2.,
68                              y_mean=im_cut.shape[1] / 2.,
69                              x_stddev=aperture_radius,
70                              y_stddev=aperture_radius,
71                              theta=0.)
72
73     fit_gauss = fitting.LevMarLSQFitter()
74
75     y, x = np.mgrid[:im_cut.shape[1], :im_cut.shape[0]]
76     gauss_science = fit_gauss(g_i, x, y, im_cut)
77
78     tmp_p = (gauss_science.x_mean.value,
79             gauss_science.y_mean.value)
80
81     # Transform tmp_cc_pos to cc_pos
82     pos = (rough_pos[0] + (tmp_p[0] - im_cut.shape[0] / 2.) + .5,
83           rough_pos[1] + (tmp_p[1] - im_cut.shape[1] / 2.) + .5)
84
85
86     else:
87         pos = rough_pos
88
89     # Vector from image center to point source
90     offset_vector = np.asarray(pos)-np.asarray(im_shape)/2.
91
92     # Radial separation of point source
93     separation = np.linalg.norm(offset_vector)
94
95     # Check separation and aperture_radius
96     if plot:
97         print(separation, aperture_radius)
98
99     # Calculate number of apertures
100    ap_nr = int(np.floor(np.pi/np.arcsin(aperture_radius/separation)))
101
102    # Azimuthal angles of the apertures
103    azimuthal_angles = np.linspace(0,2.*np.pi,ap_nr+1)[: -1]
104
105    # Rotation Matrix
106    rot_matrx = lambda phi: np.array([[np.cos(phi),np.sin(phi)],
107                                       [-np.sin(phi),np.cos(phi)]])
108
109    # Get cartesian positions of the apertures
110    temp = [np.asarray(im_shape)/2.+np.dot(rot_matrx(i),offset_vector)
111            for i in azimuthal_angles]
112    ap_pos = np.array(temp).T
113
114    # Define science and background apertures
115    science_aperture = CircularAperture(positions=ap_pos[:,0],
116                                       r=aperture_radius)
117

```



```

118     if skip_closest_apertures:
119         bg_apertures = CircularAperture(positions=ap_pos[:,2:-1],
120                                         r=aperture_radius)
121     else:
122         bg_apertures = CircularAperture(positions=ap_pos[:,1:],
123                                         r=aperture_radius)
124
125     # Determine science flux
126     sc_phot = pu.aperture_photometry(data=image_in,
127                                     apertures=science_aperture,
128                                     method="exact")
129     sc_flux = sc_phot["aperture_sum"].data[0]
130
131     # Determine background fluxes
132     bg_phot = pu.aperture_photometry(data=image_in,
133                                     apertures=bg_apertures,
134                                     method="exact")
135     bg_fluxes = bg_phot["aperture_sum"].data
136
137     # Perform sigma clipping of background fluxes
138     bg_fluxes_clipped = sigma_clip(bg_fluxes, sigma=3, maxiters=5)
139
140     # Perform statistics
141     bg_rms = np.sqrt(np.mean(bg_fluxes_clipped**2))
142     bg_mean = np.average(bg_fluxes_clipped)
143     bg_std = np.std(bg_fluxes_clipped)
144
145     snr = sc_flux/bg_rms
146
147     # Gaussain error propagation
148     snr_sigma = snr * np.sqrt((bg_std/sc_flux)**2 + (bg_std/bg_rms)**2)
149     sigma = np.abs((bg_mean-sc_flux)/bg_std)
150     signal = sc_flux-bg_mean
151     fap = 1. - erf(sigma/np.sqrt(2))
152
153     # plot for quality check
154     if plot:
155         f, ax = plt.subplots()
156         plt.imshow(image_in, origin="lower left")
157         science_aperture.plot(color="r", ax=ax)
158         bg_apertures.plot(color="w", ax=ax)
159         plt.show()
160
161     # return table with results
162     return Table(data=[(pos[0],), (pos[1],), (snr,), (sigma,),
163                       (fap,), (signal,), (snr_sigma,)],
164                 names=("pos_x", "pos_y", "signal_to_noise", "sigma",
165                       "fap", "signal", "snr_sigma"))

```

Listing 2: PynPoint function `get_false_alarm_probability`. The astrometry of the analysed object is determined via fitting of a two-dimensional Gaussian distribution. The signal is calculated via aperture photometry. The noise is determined within reference apertures at the same separation as the object.

Chapter C

Declaration of Originality



Eidgenössische Technische Hochschule Zürich
Swiss Federal Institute of Technology Zurich

Declaration of originality

The signed declaration of originality is a component of every semester paper, Bachelor's thesis, Master's thesis and any other degree paper undertaken during the course of studies, including the respective electronic versions.

Lecturers may also require a declaration of originality for other written papers compiled for their courses.

I hereby confirm that I am the sole author of the written work here enclosed and that I have compiled it in my own words. Parts excepted are corrections of form and content by the supervisor.

Title of work (in block letters):

Improving Direct Imaging of Exoplanets using Spectral Observations from SPHERE/IFS

Authored by (in block letters):

For papers written by groups the names of all authors are required.

Name(s):

Kiefer

First name(s):

Sven

With my signature I confirm that

- I have committed none of the forms of plagiarism described in the '[Citation etiquette](#)' information sheet.
- I have documented all methods, data and processes truthfully.
- I have not manipulated any data.
- I have mentioned all persons who were significant facilitators of the work.

I am aware that the work may be screened electronically for plagiarism.

Place, date

Niederstetten, 09.04.2020

Signature(s)

For papers written by groups the names of all authors are required. Their signatures collectively guarantee the entire content of the written paper.